universität wien

DISSERTATION / DOCTORAL THESIS

Titel der Dissertation /Title of the Doctoral Thesis

„Excited-state mechanisms and dynamics of the ruthenium nitrosyl complex trans-$[RuCl(NO)(Py)_4]^{2+}$“

verfasst von / submitted by

Dott. Mag. Dott. Francesco Talotta

angestrebter akademischer Grad / in partial fulfilment of the requirements for the degree of

Doktor der Naturwissenshaften (Dr. Rer. Nat.)

Wien, 2018 / Vienna 2018

Studienkennzahl lt. Studienblatt / degree programme code as it appears on the student record sheet:	A 796 605 419
Dissertationsgebiet lt. Studienblatt / field of study as it appears on the student record sheet:	Chemie
Betreut von / Supervisors:	Dr. Martial Boggio-Pasqua Univ.-Prof. Dr. Leticia Gonzàlez

Université de Toulouse

THÈSE

En vue de l'obtention du

DOCTORAT DE L'UNIVERSITÉ DE TOULOUSE

Délivré par : *l'Université Toulouse 3 Paul Sabatier (UT3 Paul Sabatier)*
Cotutelle internationale *Institut für Theoretiche Chemie, Fakultät für Chemie, Universität Wien*

Présentée et soutenue le *Date de défense (21/12/2018)* **par :**

FRANCESCO TALOTTA

Excited-state mechanisms and dynamics of the ruthenium nitrosyl complex trans-$[RuCl(NO)(Py)_4]^{2+}$

JURY

HARVEY JEREMY	Professeur (Rapporteur)	Leuven University
PATERSON MARTIN	Professeur (Rapporteur)	Heriot Watt University
POTEAU ROMUALD	Professeur (Examinateur)	UT3 Paul Sabatier
PENFOLD THOMAS	Professeur (Examinateur)	Newcastle University
GONZÁLEZ LETICIA	Professeur (Examinateur)	Vienna University
BOGGIO-PASQUA MARTIAL	Chargé de Recherche	UT3 Paul Sabatier

École doctorale et spécialité :
SDM : Physicochimie théorique - COP 01

Unité de Recherche :
Laboratoire de Chimie et Pysique Quantiques, UMR 5626, IRSAMC, CNRS et Université Toulouse 3, 118 route de Narbonne, 31062 Toulouse, France

Directeur(s) de Thèse :
Martial Boggio-Pasqua et *Leticia González*[a]

Rapporteurs :
Jeremy Harvey et *Martin Paterson*

Abbreviations

CASPT2 second-order Complete Active Space Perturbation Theory

CASSCF Complete Active Space Self Consistent Field

CI Configuration Interaction

CISD Single and Double Configuration Interaction

CPKS Coupled Perturbed Kohn-Sham

CSF Configuration State Function

DFT Density Functional Theory

diag Diagonal Representation

DTE bis(carboxylato)dithienylethene

FCI Full CI

fs Femtosecond

GGA Generalized Gradient Approximation

HF Hartree-Fock

KS-DFT Kohn & Sham DFT

LDA Local Density Approximation

LSDA Local Spin-Density Approximation

MC-SCF Multi-Configurational SCF

MLCT Metal to Ligand Charge Transfer

MO Molecular Orbital

MS-CASPT2 Multi-state CASPT2

NAC Non Adiabatic Coupling

NEVPT2 Second-order n-electron valence state perturbation theory

PT2 Second order perturbation theory

Py Pyridine ligands

SA-CASSCF State-averaged CASSCF

SCF Self Consistent Field

SCM Software for Chemistry & Materials

SH Surface Hopping

SHARC Surface Hopping with ARbitrary Couplings

SOC Spin-Orbit Coupling

TD-DFT Time Dependent DFT

TPA Two-photon absorption

UV Ultraviolet irradiation

WFT Wave Function Theory

Nomenclature

$|\Phi^{el}\rangle$ Polyelectronic wavefunction

Z_A Charge of nucleus A

r_i Coordinate of the electron i

$\hat{H}^{el}$ Total Electronic Hamiltonian

$\hat{H}^{\text{add}}$ Generic coupling hamiltonian

$\hat{H}^{\text{SOC}}$ Spin-Orbit coupling hamiltonian

$|\Phi_{\text{HF}}\rangle$ Hartree-Fock wavefunction

m Total number of nuclei

$|\varphi_i\rangle$ Single electron wavefunction (or molecular orbital)

$|\chi_i\rangle$ Atomic orbital

E_{exact} Exact non-relativistic energy

$\varepsilon_{\text{corr}}$ Correlation energy

M Number of orbitals in the active space

N Number of electrons in the active space

$|\Phi_i\rangle$ Configuration state function

$\hat{J}$ Coulomb operator

$\hat{K}$ Exchange Operator

$\hat{H}^{tot}$ Total hamiltonian

C_i CI coefficient

c_{iq} Basis function coefficient

$\hat{H}_0$ Unperturbed hamiltonian

$\hat{H}'$ Perturbed hamiltonian

$\hat{\mathcal{F}}$ Fock operator

$\hat{\mathcal{P}}$ Projection Operator

$\rho(\mathbf{r})$ Electronic density

n Total number of electrons

v_{ext} External potential

v_{ee} Electron-electron potential

$T_e[\rho]$ Electronic kinetic energy

$V_{ext}[\rho]$ Electron-nuclear attraction energy

$V_{ee}[\rho]$ Electron-electron repulsive energy

$J_{ee}[\rho]$ Coulomb energy

ω Vertical excited energy

n_s Total number of electronic states

$|\Psi_a\rangle$ Electronic basis state

$\mathbf{v}$ Nuclear velocity vector

$\mathbf{K}$ Non adiabatic coupling vector

$\mathbf{H}^{\text{diag}}$ Diagonal hamiltonian

$\mathbf{U}$ Unitary transformation matrix

$\mathbf{P}$ Three step propagator

$\mathbf{S}$ Overlap matrix

$\nabla_{\mathbf{R}} H_\alpha$ Gradient of the electronic state α

$\mathbf{R}_A$ Coordinates of the nucleus A

M_A Mass of the nucleus A

r Generic bond distance

Contents

Abstract

In the past fifteen years, ruthenium nitrosyl complexes received a growing interest due to some unique photochemical properties, such as their photochromism or the possibility to photorelease nitric oxide (NO) thought photoinduced isomerization. The direction of such photoisomerization can be controlled by external light, which can induce forward or backward conversion between the N-bonded nitrosyl (Ru-NO) and the isonitrosyl (Ru-ON) isomers, according to the selected irradiation wavelength. Hence, such complexes can potentially find applications in the development of photonic devices, such as optical switches or high density data storage. The capability of ruthenium nitrosyl complexes to also photorelease nitric oxide makes them also very appealing for biological and medical applications, including blood pressure regulation, neurotransmission, and anti-cancer activity. Despite their potential applications, the low photoconversion yield prevents an effective and reliable implementation of such systems in practical applications. For this reason, many efforts of the scientific community focused on the design and characterization of molecules that possess large photoconversion yields. The trans-$[RuCl(NO)(Py)_4]^{2+}$ complex shows a remarkable photochromic response to ultraviolet and infrared light irradiation, showing a Ru-NORu-ON photoconversion yield of 100% for a single crystal in one hour. In the past four years, DFT studies of both NO linkage photoisomerization and NO photorelease processes revealed a complex mechanism involving a two-photon sequential absorption mechanism. This mechanistic picture has been later experimentally confirmed. However, the identity of the excited states involved in the various photochemical processes that take place after light absorption were only postulated according to DFT results, which focused only on the lowest-energy singlet and triplet states. Hence, the main goal of this PhD thesis is to unravel the detailed sequence of photochemical events that lead to photoisomerization and photodissociation of the nitrosyl group. A full characterization of singlet and triplet ground and excited states potential energy surfaces was performed with accurate ab-initio CASSCF/CASPT2 calculations, whereas simulation of the most important photochemical relaxation processes that can take place after light absorption was carried out through non-adiabatic molecular dynamics simulations. The adopted multiconfigurational methods are adequate enough to deliver accurate and detailed information about the possible photoisomerization and photorelease mechanisms, including precise evaluation of spin-orbit couplings along the computed singlet and triplet potential energy surfaces. On the other hand, the dynamical simulations provide new insight on the ultrafast nature of internal conversion and intersystem crossings phenomena, allowing a direct observation of the most probable pathways and quenching funnels crossed by the trans-$[RuCl(NO)(Py)_4]^{2+}$ complex after light absorption. The stationary calculations showed agreement with the previous theoretical and experimental results, providing the presence of new radiationless pathways that involve multiple internal conversions on singlet excited states only, in addition to the singlet-triplet relaxation pathways previously assumed. Further work of this thesis includes comprehensive benchmark calculations of various DFT functionals assessed against the energies and state

characters retrieved from the CASPT2 calculations. This systematic evaluation helps to select the most suitable DFT functional used to perform the non-adiabatic molecular dynamics simulations.

Résumé de Thèse

Au cours des quinze dernières années, les complexes de ruthénium à ligand nitrosyle ont suscité un intérêt croissant en raison de certaines propriétés photochimiques uniques, telles que le photochromisme lié à la photo-isomérisation d'enchainement du ligand ou la possibilité de photo-libérer l'oxyde nitrique. La direction de cette photo-isomérisation peut être contrôlée par la lumière externe, qui peut induire une conversion vers l'avant ou vers l'arrière entre les isomères nitrosyle (Ru-NO) liés par l'azote et isonitrosyle (Ru-ON) liés par l'oxygène, en fonction de la longueur d'onde d'irradiation sélectionnée. Par conséquent, de tels complexes peuvent potentiellement trouver des applications dans le développement de dispositifs photoniques, tels que des commutateurs optiques ou le stockage de données à haute densité. La capacité des complexes de ruthénium nitrosyle à photo-libérer également l'oxyde nitrique les rend également très attrayants pour des applications biologiques et médicales, telles que, la neurotransmission et l'activité anticancéreuse. Malgré ses applications potentielles, le faible rendement de photoconversion empêche une implémentation efficace et fiable de tels systèmes dans des applications pratiques. Le complexe trans-$[RuCl(NO)(Py)_4]^{2+}$ montre une réponse photochromique remarquable à l'irradiation sous lumière ultraviolette et infrarouge, possédant un rendement de photoconversion Ru-NORu-ON avoisinant 100% pour un monocristal en une heure. Au cours des quatre dernières années, des études DFT de photo-isomérisation d'enchainement NO et de processus de photo-libération de NO ont révélé un mécanisme complexe impliquant un mécanisme d'absorption séquentielle à deux photons. Ce scénario mécanistique a été confirmé plus tard expérimentalement. Cependant, l'identité des états excités impliqués dans les divers processus photochimiques qui ont lieu après l'absorption de la lumière n'a été postulée que selon les résultats de la DFT, qui se concentraient uniquement sur les états singulet et triplet de plus basses énergies. L'objectif principal de cette thèse est donc de découvrir la séquence détaillée des événements photochimiques conduisant à la photo-isomérisation et à la photodissociation du ligand nitrosyle. Une caractérisation complète des surfaces d'énergie potentielle de l'état fondamental et des états excités singulets et triplets a été effectuée avec des calculs ab-initio précis de type CASSCF/CASPT2, tandis que la simulation des processus de relaxation photochimique les plus importants après l'absorption de la lumière a été réalisée par une étude en dynamique moléculaire non-adiabatique. Les méthodes multiconfigurationnelles adoptées sont suffisantes pour fournir des informations précises et détaillées sur les mécanismes possibles de photo-isomérisation et de photo-libération, y compris une évaluation précise des couplages spin-orbite le long des surfaces d'énergie potentielle singulet et triplet calculées. En revanche, les simulations dynamiques apportent un nouvel éclairage sur le caractère ultra-rapide des phénomènes de conversion interne et de croisement intersystèmes, permettant une observation directe des voies les plus probables et des points de croisement traversés par le complexe trans-$[RuCl(NO)(Py)_4]^{2+}$ après absorption de la lumière. Les calculs stationnaires ont montré un accord avec les résultats théoriques et expérimentaux précédents, fournissant la présence de nouvelles

voies non-radiatives impliquant de multiples conversions internes sur des états excités singulets, en plus des voies de relaxation singulet-triplet précédemment supposées. Cette thèse rapporte également des calculs de référence complets de diverses fonctionnelles en DFT évaluées par rapport aux énergies et aux caractères des états électroniques extraits des calculs CASPT2. Cette évaluation systématique permet de sélectionner les fonctionnelles les plus appropriées en DFT pour effectuer les simulations de dynamique moléculaire non-adiabatique.

Zusammenfassung

Seit fünfzehn Jahren finden Rutheniumnitrosylkomplexe immer mehr Beachtung, da sie einzigartige photochemische Eigenschaften zeigen, wie zum Beispiel Photochromie oder die Möglichkeit, Stickoxide (NO) mittels photoinduzierter Isomerisierung abzuspalten. Die Richtung, in die diese Photoisomerisierungen ablaufen, kann durch externe Lichtquellen kontrolliert werden. Letztere können sowohl die Vor- als auch die Rückkonversion zwischen N-gebundenen Nitrosyl (Ru-NO) und Isonitrosyl (Ru-ON), je nach verwendeter Wellenlänge, auslösen. Aufgrund dieser Eigenschaften finden diese Komplexe potentielle Anwendung bei der Entwicklung photonischer Bauelemente wie optische Schalter oder hochkapazitive Speicher. Die zusätzliche Eigenschaft, photochemisch Stickoxid abzuspalten, macht diese Verbindungen weiterhin interessant für biologische und medizinische Anwendungsszenarien wie zum Beispiel zur Blutdruckregulierung, bei der Neurotransmission und als potentielle Anti-Tumor-Medikamente. Trotz der vielversprechenden Anwendungsmöglichkeiten ist der Einsatz aufgrund der niedrigen Photokonversionsausbeute bisher nicht praktikabel. Daher wurden große Anstrengungen unternommen, Moleküle mit größerer Photokonversionsausbeute zu finden. trans-$[RuCl(NO)(Py)_4]^{2+}$-Komplexe zeigen dabei bemerkenswerte photochromatische Eigenschaften bezüglich UV und IR Strahlung, mit einer Ru-NORu-ON Konversionsausbeute von fast 100% innerhalb einer Stunde im Fall von Einkristallen. DFT-Studien der letzten 4 Jahre haben einen komplexen Mechanismus aufgezeigt, bei dem eine sequentielle Absorption von zwei Photonen eine Rolle spielt. Dieses mechanistische Modell wurde später experimentell bestätigt. Allerdings beschränkte sich die Identifizierung der angeregten Zustände, welche bei den photochemischen Prozessen eine entscheidende Rolle spielen, auf Vorhersagen mittels DFT-Rechnungen, welche nur die energetisch niedrigsten Singulett- und Triplett-Zustände beschreiben. Das Hauptziel dieser Arbeit ist die Aufklärung des genauen Ablaufs der photochemischen Ereignisse, welche zur Photoisomerisierung und letztendlich Photodissoziation der Nitrosylgruppe führen. Dazu wurde eine vollständige Charakterisierung der involvierten Singulett- und Triplettpotentialenergieflächen mittels hochgenauer ab initio CASSCF/CASPT2-Rechnungen durchgeführt, und anschließend die wichtigsten photochemischen Relaxationsprozesse, welche nach der Lichtanregung stattfinden, durch nicht-adiabatische Moleküldynamikrechnungen simuliert. Die verwendeten Multikonfigurationsmethoden sind geeignet, genaue und detaillierte Informationen über die möglichen Photoisomierisierungs- und Photoabspaltungsmechanismen zu erhalten, inklusive der präzisen Evaluierung der Spin-Bahn-Kopplungen, welche entlang der berechneten Singulett- und Triplettpotentialflächen auftreten. Weiterhin liefern die Dynamiksimulationen neue Erkenntnisse bezüglich der ultraschnellen Natur der Internen Konversion und der Interkombinationsvergänge, und ermöglichen eine direkte Beobachtung der wahrscheinlichsten Reaktionswege und der Trichter welche der trans-$[RuCl(NO)(Py)_4]^{2+}$-Komplex nach der Lichtanregung durchläuft. Die stationären Berechnungen stimmen dabei mit den bisherigen theoretischen und

experimentellen Ergebnissen überein und zeigen, zusätzlich zu den schon bekannten Singulett-Triplett-Reaktionspfaden, die Existenz strahlungsloser Reaktionspfade, welche verschiedene interne Konversionen entlang der Singulett-Zustände beinhalten.

Weiterhin beschäftigt sich diese Arbeit mit umfassenden Benchmarkrechnungen verschiedener DFT- Funktionale, verglichen mit den Energien und Zustandscharakterisierungen mittels CASPT2- Rechnungen. Diese systematische Evaluierung erlaubt die Auswahl des am besten geeigneten DFT- Funktionals, welches bei den nicht-adiabatischen Moleküldynamiksimulationen zum Einsatz kommt.

Chapter 1

Introduction

1.1 Background on Photochemistry

Photochemistry studies chemical reactions and other physico-chemical phenomena induced by light absorption. The role of light in affecting chemical changes has been recognized for many years. For instance, the connection between solar light and the biosynthesis of plant carbohydrates from carbon dioxide and water was known since the early 1800's. However, the systematic and accurate investigation of the connections between absorbed light and the induced chemical or physical processes, took place only starting from the beginning of the last century. Indeed, the development of more accurate experimental techniques, allowed for the discovery of a rich range of interesting chemical reactions that can be triggered by light.

In the early 1910's Stark and Einstein suggested, in analogy with the photoelectric effect, that an isolated molecule in gas phase can absorb one photon and then undergo an elementary photoreaction act. Actually, after the absorption a molecule can undergo different kind of chemical reactions or experience processes that do not involve chemical transformations (photophysical processes).

In the first half of the 20-th century, some fundamental photochemical reactions that are of practical use today were discovered, such as the dimerization of cinnamic acids,[1] photoreduction of carbonyl compounds,[2] and photoisomerization of olefins.[3] However, the fundamental rules behind these reactions were still unknown. During the 1930s and 1940s, thanks to the strengthening of quantum theory and advance of spectroscopic techniques, it was possible to formulate the physical principles required to understand photochemistry. The theoretical concepts of molecular orbital (MO) and singlet or triplet state level were introduced and then confirmed by a series of experiments on organic molecules. By the end of the 1950's, most of the rules of photochemistry were established and correlations were made between spectroscopic properties of the molecules and the orbital configuration of the excited states, providing a firm scientific platform for the birth of the modern

molecular photochemistry during the 1960's and 1970's. In this period, the theory of photoreactions made a significant step forward when the concept of potential energy surface (PES) started to be used for the comprehension of reaction mechanisms. The ability to discuss the reactive processes in terms of PESs instead of state levels, added new richness to the intellectual aspects photochemical reactions, but also served to propose new experiments previously unimaginable. Theoretical concepts of upper excited state reactivity, adiabatic and chemioluminescent reactions can be easily explained in terms the ground and excited states PESs topology. In this context, the power of mechanics investigations of these phenomena based on theoretical calculations has been demonstrated during the last thirty years, and nowadays computational chemistry methods are considered an essential investigation tool to be coupled with experiments to properly tackle the study of photoreaction mechanism or the design of new light-sensitive materials.
In general a photochemical reaction can be seen as a three step process:

1. Absorption of the electromagnetic radiation to produce excited states
2. Primary photochemical reactions involving the excited states
3. Secondary (or dark) reactions, that may occur eventually after the end of the primary photochemical reactions

The first two steps can be described using the concept of PESs, as shown in Figure 1.1 for a simple diatomic molecule. The diagram shows the singlet ground state S_0, the two singlet excited states S_1 and S_2, and the triplet excited state T_1 together with the most important absorption and primary photoreactions that can happen among the electronic states.
In the first step, the energy of incident light photons ($h\nu_1$) is used to excite an electron to a high-energy orbital, (usually an anti-bonding orbital) producing an electronically excited species A^*:

$$A + h\nu_1 \rightarrow A^* \tag{1.1}$$

The vertical excitation $S_0 \rightarrow S_2$ occurs with no change in the bond length r (^0r_e equilibrium bond length). The molecule retains the same geometry it had in the ground state. This observation, stated by the Franck-Condon principle[4;5] is justified by the short transition time scale of the electrons from the ground to the excited state compared to the bond vibrations time scale. Therefore, the geometry of the electronically excited molecule is in the first instant that it is produced just like the ground-state one.
From here, the system undergoes various primary photochemical reactions that can be grouped into *luminescence* transitions with emission of a photon:

$$A^* \rightarrow A + h\nu_2 \qquad (\nu_2 < \nu_1) \tag{1.2}$$

or *radiationless* transitions with no photon emission:

$$A^* \rightarrow A \tag{1.3}$$

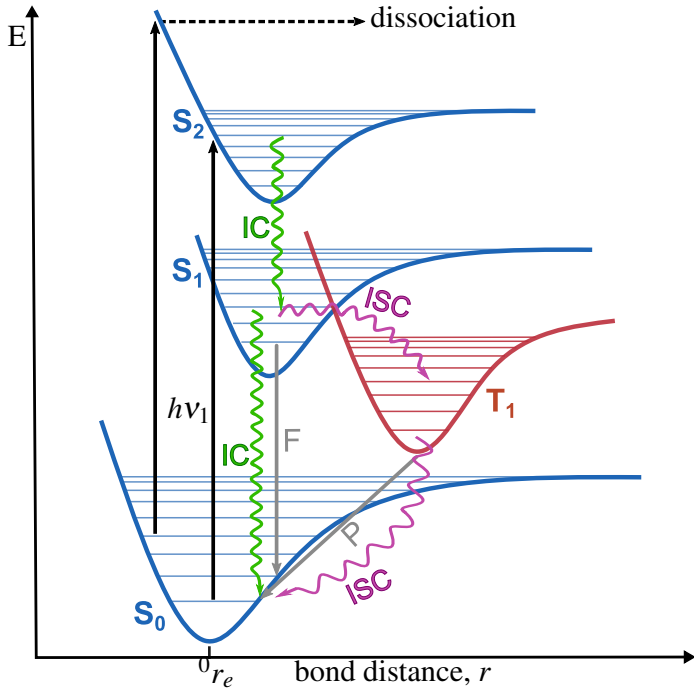

Figure 1.1 Schematic potential energy diagram for a diatomic molecule A as a function of the bond length (r), showing the most important photophysical processes. Straight arrows depict the radiative processes: absorption ($h\nu$), fluorescence (F), and phosphorescence (P). Wavy arrows show the radiationless processes: internal conversion (IC), and intersystem crossing (ISC). Dashed arrow pointing towards large values of the bond distance indicates a dissociation process.

It may also happen that a substantial part of the photon energy is used to break a chemical bond producing two radicals. In this case a *photodissociation* process takes place:

$$A^* \rightarrow B + C \tag{1.4}$$

The remaining energy is spread over the vibrational, rotational and translational motion of both fragments.

If the molecule does not dissociate, it relaxes nonraditive from the S_2 excited state, by loosing vibrational energy through *internal conversion* (IC) towards S_1. In this case energy is dissipated into heat through the vibrational motion of the system. Since the IC transition is spin-allowed (no change in the spin multiplicity between S_2 and S_1), it is very efficient and usually requires about 10^{-12} sec. From S_1 the system may eventually return to the ground state S_0 via another radiationless IC or with emission of a photon through a *fluorescence* (F) transition. Usually fluorescence occurs in 10^{-9} to 10^{-7} sec after the absorption of the original radiation. However, from the S_1 state the system can undergo another non-radiative transition called *intersystem crossing* (ISC) which involves a spin-flipping from the singlet S_1 towards the lower triplet T_1. Singlet to triplet conversion

usually occurs slower than IC, as this transition is forbidden by the general spectroscopic selection rules. Nevertheless, for some molecules such as transition metal complexes with heavy atoms that display large values of spin-orbit coupling (SOC), the ISC rates can be brought to the IC ones. Further details about this particular case will be given in Chapter 3 and Chapter 6 where we will investigate the photochemistry of a transition metal complex with very similar ISC and IC rates. From the triplet state T_1 the system may eventually cross over S_0 via another radiationless ISC, but in many cases a radiative transition occurs, even though it has low probability. This type of radiative transition is called *phosphorescence* (P). Because phosphorescence is a process with a low probability, the T_1 state may persist from a fraction of second to many seconds.
The following sections will give a short overview on the concepts of photochromic systems and molecular switches, as in this PhD we tackle the study of a particular type of ruthenium nitrosyl complex that acts as a photochromic system.

1.2 Photochromic Systems

Photochromism may be defined as the reversible phototransformation of a chemical species between two forms A and B having different absorption spectra, as shown in Figure 1.2. The first direct observation of photochromism has been reported by Fritsche[6] in 1867, who observed the bleaching of a orange-colored tetracene solution exposed to air and sunlight, and regeneration of the color in the dark. Since then, photochromism has received considerable attention and it is still an active field of basic and applied research. Nowadays a well known example of photochromic system are the ophthalmic lens that darken on exposure to specific wavelengths of sufficient intensity.[7]
Photochromic transformations are generally based on unimolecular processes involving the

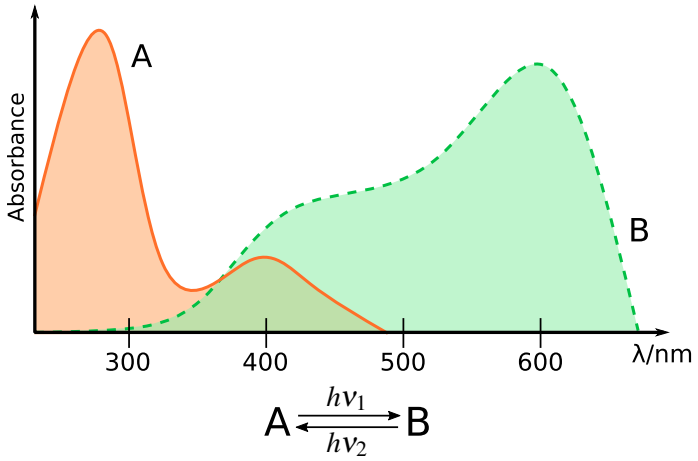

Figure 1.2 Illustration of absorption spectra of the two photochromic isomers A and B.

interconversion of two isomers, such as cis/trans, ring opening/closing, or intramolecular

proton transfer. More generally, the process behind this conversion is known as *photoisomerization*, formally written as:

$$\begin{aligned} A + h\nu_1 &\rightarrow A^* && (1.5)\\ A^* &\rightarrow B && (1.6) \end{aligned}$$

The excited molecule A^* isomerizes to B, reverting to the ground state by ISC or IC radiationless decay. The reversible process B→A can occur either thermally (*Photochromism of type T*) or photochemically (*Photochromism of type P*). In the second case, the B isomer is re-excited upon irradiation at a different frequency ν_2, and then it relaxes via ISC or IC towards A:

$$\begin{aligned} B + h\nu_2 &\rightarrow B^* && (1.7)\\ B^* &\rightarrow A && (1.8) \end{aligned}$$

The reactive mechanism triggered by the irradiation wavelength which reversibly generates the isomers A and B is also known as *photoswitching*. In both directions the photon energy is used to overcome the activation barriers that can not be normally surmounted by thermal energy, by performing part of the structural changes in the excited states.
Photoswitching is normally triggered by a single-photon absorption. However, the A and B photoproducts can also be formed through a two-photon absorption (TPA) mechanism. In this case, the photon absorption can be classified into three groups:

- vertical simultaneous absorption of two photons via a virtual level
- vertical sequential absorption of two photons, where the second photon absorption takes place form a real excited state
- sequential absorption through metastable intermediate species X

The three processes are schematized in Figure 1.3.

During a photoisomerization many physicochemical properties change, such as the dielectric constant, oxidation/reduction potential, refractive index and obviously the color. This ability to give a light-controlled reversible change of molecular properties, makes these systems very interesting for the development of *photonic* devices, such as erasable optical memories or photooptical switch components. In the ongoing quest for nano-devices and molecular machines, the design of molecular switching elements integrated with a variety of functions represents an essential part of materials science and a formidable challenge at the same time. For these reasons, many efforts of the scientific community focus on design, investigation and production of devices capable of acting as switches[8–14] at molecular level. The application of such technology covers a wide range of scientific fields, such as molecular computing,[15–17] molecular logic gates,[18] optoelectronic devices,[19–23] and high-density memory elements[8–10;24]. Usually, systems

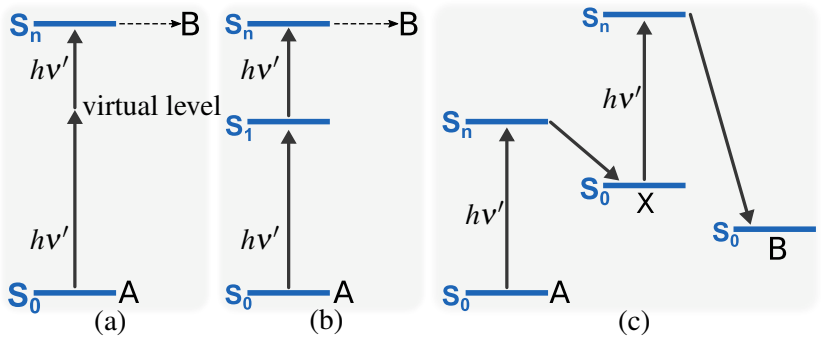

Figure 1.3 Schematic of energy levels for a two-photon absorption mechanisms, (a) vertical simultaneous two-photon absorption, (b) vertical sequential two-photon absorption, (c) sequential absorption through a metastable state X.

that exhibit P-type photochromism are more adequate for the development of such practical applications with respect to systems which exhibit T-type photochromism, because of the thermal stability of both isomers A and B under ambient conditions.
One of the earliest photochromic system that has been intensively studied was the bis(carboxylato)dithienylethene (DTE) molecule,[25–28] synthesized in the late 1980's. Experimental evidences[29–31] pointed out how an aqueous solution of DTE changes its color

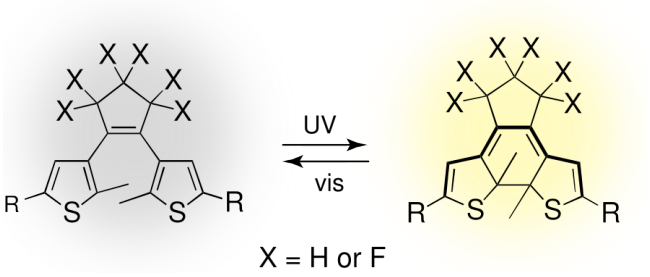

Figure 1.4 Example of photochromic system: the DTE molecule undergoes reversible photoisomerization upon UV and visible light irradiation.

from transparent to yellow upon ultraviolet irradiation (UV) as shown in Figure 1.4. The reaction mechanism involves interconversion between open and closed forms of the central ring, i.e. unconjugated and π-conjugated forms. Upon UV light the closed-ring isomer is generated, which later can switch back to the original open-ring form upon visible light irradiation.
Through this simple example, it is easy to figure out the usefulness of such systems, for instance storing digital information by establishing a one-to-one correspondence between the open-ring (closed-ring) geometry and the ON (OFF) state of a device, creating a chemical switch triggered by light.
So far, various types of organic photochromic compounds such as azobenzene, diarylethenes, fulgides, spirobenzopyrans, have been developed. However, in the last 15

years, transition metal complexes featuring photoresponsive ligands appeared to be an interesting alternative to pure organic molecules.[32–35] Indeed, combining photochromic ligands with transition metal and coordination complexes, would not only render the triplet state of the organic photochromic system more readily accessible due to the large spin-orbit coupling of the heavy metal center, but would also provide new properties deriving from redox, optical, and magnetic properties of the metal complexes. Moreover the photochromism could be extended from the high energy UV region to the less destructive visible-light sources, through the readily accessible triplet excited states. Early studies on these molecules were mostly focused on the first row transition metals, but the last 30 years brought more interest in metals of 2nd and 3rd row,[36] since the application of ruthenium polypyridyl in dye sensitized solar cells was reported.[37;38] As a result, the number of studies on the photochemical properties of these 2nd and 3rd rows has expanded significantly. The research on photochromic metal complexes has already led to potential applications such as oxygen sensors,[39;40] OLEDS[41;42] holographic recording.[43]
In the next paragraph we will introduce a particular ruthenium complex showing remarkable photochemical properties that will investigated in details throughout the next chapters.

1.3 A Prototype of Photochromic System

A critical issue of many organic and inorganic photochromic systems is the photoconversion yield which usually results to be very slow, representing a problem for practical applications. Therefore, a lot of efforts are devoted to the design of new systems with higher photoconversion rates. Among the class of ruthenium nitrosyl complexes, the trans-$[RuCl(NO)(Py)_4]^{2+}(PF_6)_2 \cdot \frac{1}{2}H_2O$[†] (where Py denotes pyridine ligands) has raised the attention of the scientific community in the recent years.[44–48] This photochromic system undergoes P-type linkage photoisomerization between the Ru metal center and the NO ligand, showing a remarkable 100% Ru-NO $\rightarrow$ Ru-ON photoconversion yield upon irradiation of a single crystal for 1 hour.[44] So far, this is the only metal complex of the nitrosyl class ML_5NO showing such a large quantum yield, although the slow photoconversion rate constitutes a drawback for real efficient applications. The three isomers involved in the photoisomerization are shown in Figure 1.5. Photoisomerization starts from the N-bonded ground-state isomer (denoted **GS**) corresponding to an orange-colored crystal. Upon blue light absorption, this species undergoes a 180° rotation of the nitrosyl ligand to form the isonitrosyl Ru-ON isomer (denoted **MS1**), corresponding to a green-colored crystal. Subsequent irradiation of the new crystal **MS1** with infrared light (around 980nm) generates a mixture of two isomers: the initial orange crystal **GS** and a metastable black-colored isomer called **MS2** (central molecule on Figure 1.5), with the nitrosyl ligand on "side-on" configuration $Ru<^{N}_{O}$ rotated

[†]also known as trans-$[RuCl(NO)(Py)_4]^{2+}$

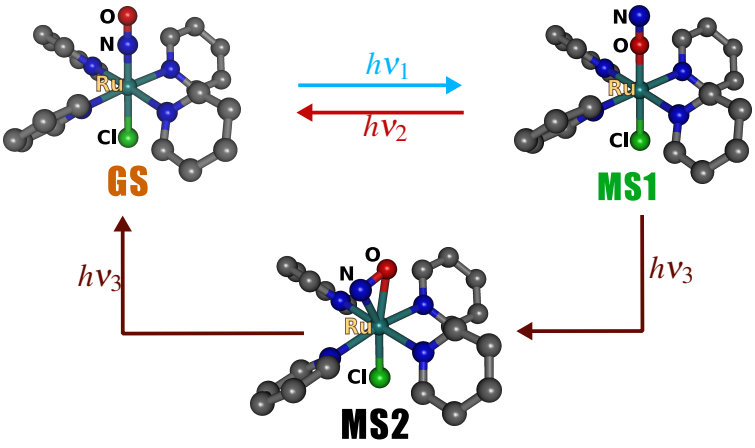

Figure 1.5 Schematic representation of the linkage isomers of the trans-$[RuCl(NO)(Py)_4]^{2+}$complex involved in the P-type photoisomerization (hydrogen atoms are omitted): ground state **GS**, metastable states **MS1** and **MS2**. The experimental irradiation conditions are: blue, 473 nm; red, 782 nm; dark red 980 nm.

by 90°. The **MS2** isomer eventually turns to the orange crystal **GS** if continuously exposed to infrared light. Alternatively, **MS1** returns directly to **GS** upon red light irradiation of 782 nm.

Beside photoisomerization, ruthenium nitrosyl complexes can also release nitric oxide upon external light irradiation. In particular, experimental[49] evidences pointed out how an aqueous solution of trans-$[RuCl(NO)(Py)_4]^{2+}$can photorelease $NO^{\bullet}$ upon blue light irradiation at 473 nm (see Figure 1.6), although this molecule shows a lower quantum yield with respect to other ruthenium nitrosyl complexes.[50;51] Nevertheless, the possibility to photorelease NO makes this system even more interesting because of the well known relevance of the nitric oxide in biological processes such as blood pressure regulation,[52] neurotransmission[53] and anti-cancer activity.[54] Indeed, a lot of studies in this field have already produced numerous NO-releasing drugs not only for cancer treatment, but also for cardiovascular therapy,[55] as multifunctional agents for photodynamic therapy[56] and AIDS treatment.[57] On the other hand, it should be noted that uncontrolled NO delivery causes

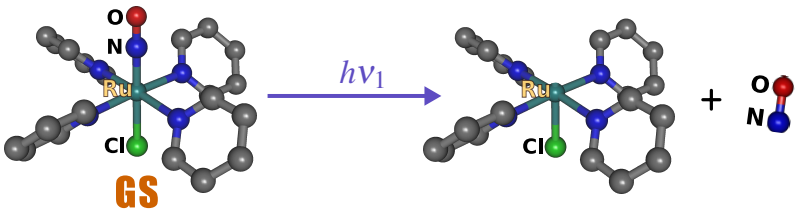

Figure 1.6 Schematic representation of nitrosyl photodissociation of the trans-$[RuCl(NO)(Py)_4]^{2+}$complex (hydrogen atoms are omitted) at the irradiation frequency of 473 nm.

also apoptosis (cell death) of healthy cells. Accordingly, considerable efforts have been devoted to the design of NO donor molecules which can be activated "on-demand" and can locally deliver NO upon light exposure. Precision delivery of cancer drugs to tumor site is crucial for improving therapeutic efficacy and minimizing adverse effects. In this context, the class of ruthenium nitrosyl complexes was found to be very stable over a long time in physiological conditions which makes the trans-$[RuCl(NO)(Py)_4]^{2+}$molecule a great candidate for harmless and precise NO delivery for anticancer drugs controlled by external light.[58]

1.4 The Aim of This PhD Thesis

Despite the extensive experimental investigations carried out on the trans-$[RuCl(NO)(Py)_4]^{2+}$molecule, the mechanism behind photoisomerization and photodissociation processes is still unclear. A first study[45] based on density functional theory (DFT) calculations on the lowest potential energy surfaces S_0 and T_1 suggested a complex sequential mechanism (Fig 1.3(c)) involving IC and ISC to explain the Ru-NO $\rightleftarrows$ Ru-ON photoisomerization process. This TPA mechanism has been later confirmed by experiments.[47] In a second publication,[59] the photodissociation has been investigated using a similar DFT-based strategy, uncovering the competing mechanism between nitrosyl isomerization and dissociation.
Whilst these two DFT-based works represent a major breakthrough in the understanding of the mechanisms behind the photoreactivity of such ruthenium nitrosyl complexes, relaxation pathways from the initial excited singlet states and their possible deactivation to higher triplet states by ISC have not been considered thoroughly. Surely, to make potential applications work efficiently it is necessary to understand all the underlying photochemical processes that are involved in both nitrosyl isomerization and dissociation. Thus, in this PhD thesis we will carry out an accurate and detailed investigation of the photoisomerization and photodissociation pathways of the trans-$[RuCl(NO)(Py)_4]^{2+}$complex, using several different computational chemistry methods. The work has been divided into two parts which follow the chronological development of this thesis project. In the first part, an extensive analysis of the excited states will be performed with robust and accurate ab-initio multiconfigurational quantum chemistry methods capable to properly describe bond breaking and bond formation. This first set of calculations focused on the static excited-states properties such as excited state energies, transition probability, and spin-orbit couplings, at particular nuclear conformations which are assumed to be critical in the description of the photochromic properties of the system. However, retrieving the exact reaction mechanism solely from the interpretation of the static ab-initio calculations is not a trivial task, notably when dealing with relatively large non-small systems owing many degrees of freedom. A detailed assessment of the photochemical relaxation processes can only be obtained by explicit simulations of the excited states dynamics with the proper description of IC and ISC

transitions. To this end, the second part of this thesis will be devoted to the investigation and discussion of the photoisomerization mechanism of the trans-$[RuCl(NO)(Py)_4]^{2+}$complex through semiclassical excited state dynamics simulations. The outcome of these simulations will support and complete the ab-initio results obtained in the first part of this work, by allowing for the observation of the most probable photoisomerization pathways including the quenching funnels that can potentially slow down the entire photoswitching process. Both static ab-initio and semiclassical dynamics simulations allowed us to confirm some of the previous assumptions made by the scientific community on the photochemistry of this compound but also allowed us to propose new mechanisms that could explain in great detail the isomerization and dissociation of this photochromic system. This thesis is structured as follow:

- Chapter 2 will give an overview on the methods and analysis tools used for the calculations carried out in this Thesis
- Chapter 3 will present in more details the TPA process derived from a previous study of the N$\rightarrow$O photoisomerization, and then this photoisomerization mechanism will be studied using very accurate quantum mechanical methods
- In Chapter 4 the NO photodissociation will be studied with the same theoretical tools used in Chapter 3
- Chapter 5 is dedicated to assess many DFT functionals against the CASPT2 results. This analysis is motivated by the fact that our subsequent semiclassical excited state dynamics study requires the use of adequate DFT/TD-DFT potential energy surfaces
- Chapter 6 discuss the photoisomerization mechanism that is obtained by means of the semiclassical excited state dynamics methods

Bibliography

[1] H. I. Bernstein and W. C. Quimby. The photochemical dimerization of *trans*-cinnamic acid. *J. Am. Chem. Soc.*, 65:1845–1846, 1943.

[2] R. S. Davidson and P. F. Lambeth. The photoreduction of carbonyl compounds by amines. *Chem. Commun. (London)*, pages 1265–1266, 1967.

[3] H. Morrison. cis-trans isomerization of olefins by intramolecular energy transfer. *J. Am. Chem. Soc.*, 87(4):932–932, 1965.

[4] J. Franck. *Trans. Faraday Soc.*, 21:536, 1926.

[5] E. U. Condon. *Phys. Rev.*, 28:858, 1926.

[6] M. Fritsche. *Comp. Rend.*, 69:1035, 1867.

[7] T. Eppig, A. Speck, M. Gillner, D. Nagengast, and A. Langenbucher. Photocromic dynamics of ophthalmic lenses. *Appl. Opt.*, 51:133–8, 2012.

[8] Z. F. Liu, K Hashimoto, and A. Fujishima. Photoelectrochemical information storage using an azobenzene derivative. *Nature*, 347:658–660, 1990.

[9] S. Hunter, F. Kiamilev, S. Esener, D. A. Parthenopoulos, and P. M. Rentzepis. Potentials of two-photon based 3-d optical memories for high performance computing. *Appl. Opt.*, 29(14):2058–2066, 1990.

[10] B. L. Feringa, W. F. Jager, and B. de Lange. Organic materials for reversible optical data storage. *Tetrahedron*, 49(37):8267 – 8310, 1993.

[11] G. M. Tsivgoulis and J.-M. Lehn. Multiplexing optical systems: Multicolor-bifluorescent-biredox photochromic mixtures. *Adv. Mater.*, 9(8):627–630.

[12] M. Seibold, M. Handschuh, H. Port, and H.C. Wolf. Photochromic fulgides: towards their application in molecular electronics. *J. Lumin.*, 72-74:454 – 456, 1997. Luminescence and Optical Spectroscopy of Condensed Matter.

[13] R. H. Mitchell, T. R. Ward, Y. Wang, and P. W. Dibble. Pi-switches: synthesis of three-way molecular switches based on the dimethyldihydropyrenemetacyclophanediene valence isomerization. *J. Am. Chem. Soc.*, 121(11):2601–2602, 1999.

[14] G. Wirnsberger, B. J. Scott, B. F. Chmelka, and G. D. Stucky. Fast response photochromic mesostructures. *Adv. Mater.*, 12(19):1450–1454.

[15] J. S. Miller. Molecular electronics? *Adv. Mater.*, 2(8):378.

[16] J. S. Miller. Molecular electronics? *Adv. Mater.*, 2(10):495.

[17] J. S. Miller. Molecular electronics? *Adv. Mater.*, 2(12):601.

[18] D. Liu, W Chen, K. Sun, K. Deng, W. Zhang, Z. Wang, and X. Jiang. Resettable, multi-readout logic gates based on controllably reversible aggregation of gold nanoparticles. *Angew. Chem. Int. Ed.*, 50(18):4103–4107.

[19] H. Dong, H. Zhu, Q. Meng, X. Gong, and W. Hu. Organic photoresponse materials and devices. *Chem. Soc. Rev.*, 41:1754–1808, 2012.

[20] T. Tsujioka and M. Irie. Electrical functions of photochromic molecules. *J. Photochem. Photobiol.*, 11(1):1 – 14, 2010.

[21]

[22] D. Roldan, V. Kaliginedi, S. Cobo, V. Kolivoska, C. Bucher, W. Hong, G. Royal, and T. Wandlowski. Charge transport in photoswitchable dimethyldihydropyrene-type single-molecule junctions. *J. Am. Chem. Soc.*, 135(16):5974–5977, 2013. PMID: 23574365.

[23] F. Wang, X. Liu, and I. Willner. Integration of photoswitchable proteins, photosynthetic reaction centers and semiconductor/biomolecule hybrids with electrode supports for optobioelectronic applications. *Advanced Materials*, 25(3):349–377.

[24] A.S. Dvornikov, C.M. Taylor, Y.C. Liang, and P.M. Rentzepis. Photorearrangement mechanism of 1-nitro-naphthaldehyde and application to three-dimensional optical storage devices. *J. Photochem. Photobiol. A*, 112(1):39 – 46, 1998.

[25] T. Kodani, K. Matsuda, T. Yamada, S. Kobatake, and M. Irie. Reversible diastereoselective photocyclization of a diarylethene in a single-crystalline phase. *J. Am. Chem. Soc.*, 122(40):9631–9637, 2000.

[26] S. Kobatake, K. Uchida, E. Tsuchida, and M. Irie. Single-crystalline photochromism of diarylethenes: reactivity–structure relationship. *Chem. Commun.*, pages 2804–2805, 2002.

[27] M. Morimoto and M. Irie. Photochromism of diarylethene single crystals: crystal structures and photochromic performance. *Chem. Commun.*, pages 3895–3905, 2005.

[28] S. Kobatake, S. Takami, H. Muto, T. Ishikawa, and Irie. M. Rapid and reversible shape changes of molecular crystals on photoirradiation. *Nature*, 446:778, 2007.

[29] B. L. Feringa. *Molecular Switches*. W. R. Browne, 2011.

[30] M. Irie. Diarylethenes for memories and switches. *Chem. Rev.*, 100(5):1685–1716, 2000. PMID: 11777416.

[31] J. Kärnbratt, M. Hamm, S. Li, H.L. Anderson, B. Albinsson, and J. Andréasson. Photochromic supramolecular memory with nondestructive readout. *Angew. Chem. Int. Ed.*, 49(10):1854–1857.

[32] C.-C. Ko and W.-W. V. Yam. Transition metal complexes with photochromic ligands-photosensitization and photoswitchable properties. *J. Mater. Chem.*, 20, 2010.

[33] S. Kume and H. Nishihara. Photochrome-coupled metal complexes: molecular processing of photon stimuli. *Dalton Trans.*, pages 3260–3271, 2008.

[34] Y. Hasegawa, T. Nakagawa, and T. Kawai. Recent progress of luminescent metal complexes with photochromic units. *Coord. Chem. Rev.*, 254(21-22):2643–2651, 2010.

[35] M. Akita. Photochromic organometallics, a stimuli-responsive system: An approach to smart chemical systems. *Organometallics*, 30(1):43–51, 2011.

[36] J. G. Vos and M. T. Pryce. Photoinduced rearrangements in transition metal compounds. *Coord. Chem. Rev.*, 254(21):2519 – 2532, 2010. 18th International Symposium on the Photochemistry and Photophysics of Coordination Compounds Sapporo, 2009.

[37] B. O'Regan and M. Gräztel. A low-cost, high-efficiency solar cell based on dye-sensitized colloidal tio2 films. *Nature*, 353(737), 1991.

[38] A. Hagfeldt and M. Grätzel. Molecular photovoltaics. *Acc. Chem. Res.*, 33(5):269–277, 2000. PMID: 10813871.

[39] C. Malins, G. H. Glever, D. B. MacCraith, S. Fanni, and J. G. Vos. The preparation of a sol–gel glass oxygen sensor incorporating a covalently bound fluorescent dye. *Anal. Commun.*, 36:3–4, 1999.

[40] A. Lobnik, I. Oehme, I. Murkovic, and O. S. Wolfbeis. ph optical sensors based on sol–gels: Chemical doping versus covalent immobilization. *Anal. Chim. Acta*, 367(1):159 – 165, 1998.

[41] P.-T. Chou and Y. Chi. Phosphorescent dyes for organic light-emitting diodes. *Chem. Eur. J.*, 13(2):380–395.

[42] H. Inomata, K. Goushi, T. Masuko, T. Konno, T. Imai, H. Sasabe, J. J. Brown, and C. Adachi. High-efficiency organic electrophosphorescent diodes using 1,3,5-triazine electron transport materials. *Chem. Mater.*, 16(7):1285–1291, 2004.

[43] M. Imlau, Haussühl, Woike S., and T. Holographic recording by excitation of metastable electronic states in $na_2[fe(cn)_5no]\cdot 2h_2o$: a new photorefractive effect. *Appl. Phys. B*, 68:877, 1999.

[44] B. Cormary, I. Malfant, M. Buron-Le Cointe, L. Toupet, B. Delley, D. Schaniel, N. Mockus, T. Woike, K. Fejfarová, V. Petříček, and M. Dušek. $[ru(py)_4cl(no)](pf_6)_2\cdot 5h2o$: A model system for structural determination and ab initio calculations of photo-induced linkage no isomers. *Acta Crystallogr., Sect. B: Struct. Sci.*, 65:612, 2009.

[45] J. Sanz García, F. Alary, M. Boggio-Pasqua, I. M. Dixon, I. Malfant, and J.-L. Heully. Establishing the two-photon linkage isomerization mechanism in the nitrosyl complex trans-$[rucl(no)(py)_4]^{2+}$ by dft and tddft. *Inorg. Chem.*, 54:8310, 2015.

[46] J. Sanz García, F. Alary, M. Boggio-Pasqua, I. M. Dixon, and J.-L. Heully. Is photoisomerization required for no photorelease in ruthenium nitrosyl complexes? *J. Mol. Model.*, 22:284, 2016.

[47] L. Khadeeva, W. Kaszub, M. Lorenc, I. Malfant, and M. Buron-Le Cointe. Buron-le cointe, m. two-step photon absorption driving the chemical reaction in the model ruthenium nitrosyl system $[ru(py)_4cl(no)](pf_6)_2\cdot 1/2h_2o$. *Inorg. Chem.*, 55:4117, 2016.

[48] M. Tassé, H. S. Mohammed, C. Sabourdy, S. Mallet-Ladeira, P. G. Lacroix, and I. Malfant. Synthesis, crystal structure, spectroscopic, and photoreactive properties of a ruthenium(ii)-mononitrosyl complex. *Polyhedron*, 119:350, 2016.

[49] A. G. De Candia, J. P. Marcolongo, R. Etchenique, and L. D. Slep. Widely differing photochemical behavior in related octahedral Ru-NO^6 compounds: Intramolecular redox isomerism of the excited state controlling the photodelivery of no. *Inorg. Chem.*, 49(15):6925–6930, 2010. PMID: 20578716.

[50] K. Karidi, A. Garoufis, A. Tsipis, N. Hadjiliadis, H. den Dulk, and J. Reedijk. Synthesis, characterization, in vitro antitumor activity, dna-binding properties and electronic structure (dft) of the new complex cis-(cl,cl)[ruiicl2(no+)(terpy)]cl. *Dalton Trans.*, pages 1176–1187, 2005.

[51] J. Akl, I. Sasaki, P. G. Lacroix, I. Malfant, S. Mallet-Ladeira, P. Vicendo, N. Farfán, and R. Santillan. Comparative photo-release of nitric oxide from isomers of substituted terpyridinenitrosylruthenium(ii) complexes: experimental and computational investigations. *Dalton Trans.*, 43:12721–12733, 2014.

[52] D. D. Rees, R. M. Palmer, and S. Moncada. Role of endothelium-derived nitric oxide in the regulation of blood pressure. *Proceedings of the National Academy of Sciences*, 86(9):3375–3378, 1989.

[53] L. J. Ignarro. Nitric oxide. a novel signal transduction mechanism for transcellular communication. *Hypertension*, 16(5):477, 1990.

[54] A. Levina, A. Mitra, and P. A. Lay. Recent developments in ruthenium anticancer drugs. *Metallomics*, 1:458–470, 2009.

[55] J.-L. Burgaud, E. Ongini, and P. Soldato. Nitric oxide-releasing drugs. *Ann. N. Y. Acad. Sci.*, 962(1):360–371.

[56] S. L. H. Higgins and K. J. Brewer. Designing red-light-activated multifunctional agents for the photodynamic therapy. *Angew. Chem. Int Ed.*, 51(46):11420–11422.

[57] D. Torre, A. Pugliese, and F. Speranza. Role of nitric oxide in hiv-1 infection: friend or foe? *Lancet Infec. Dis.*, 2(5):273 – 280, 2002.

[58] M. J. Rose and P. K. Mascharak. Photoactive ruthenium nitrosyls: Effects of light and potential application as no donors. *Coord. Chem. Rev.*, 252(18):2093 – 2114, 2008.

[59] J.S. García, F. Alary, M. Boggio-Pasqua, I. M. Dixon, and J.-L. Heully. Is photoisomerization required for no photorelease in ruthenium nitrosyl complexes? *J. Mol. Model*, 22:284, 2016.

Chapter 2

Methodology and Implementation

The aim of this chapter is to present the theoretical methods used in this PhD thesis and to outline the work carried out during the two months secondment at the Software for Chemistry and Material (SCM) software company in Amsterdam. To this end, throughout the first part of the chapter we will briefly detail the Complete Active Space Self-Consistent Field (CASSCF), the second-order Complete Active Space Perturbation Theory (CASPT2), the Density Functional Theory (DFT) and its Time Dependent formulation (TD-DFT). In the second part, we will firstly give an overview of the theoretical method used for the analysis of the trans-$[RuClPy_4(NO)]^{2+}$ photochemistry, and finally we will focus on the two months assignment in SCM.

2.1 Treatment of the electronic structure

The solution of the Schrödinger equation[1] represents a big challenge for the theoretical chemistry community, as this eigenvalue equation remains nowadays unsolvable exactly for a many-electron system. When studying the electronic problem the equation is written in its time-independent form, making use of the Born-Oppenheimer approximation:[2]

$$\hat{H}^{el}|\Phi^{el}\rangle = E|\Phi^{el}\rangle \tag{2.1}$$

where $\hat{H}^{el}$ is the electronic hamiltonian of the system, written as:

$$\hat{H}^{el} = -\sum_{i}^{n}\frac{1}{2}\nabla_i^2 + \sum_{A<B}^{m}\frac{Z_A Z_B}{|\mathbf{R}_A - \mathbf{R}_B|} - \sum_{A}^{m}\sum_{i}^{n}\frac{Z_A}{|\mathbf{R}_B - \mathbf{r}_i|} + \sum_{i<j}^{n}\frac{1}{|\mathbf{r}_i - \mathbf{r}_j|} \tag{2.2}$$

where n is the total number of electrons, m is the total number of nuclei, Z_A is the charge of nucleus A, $\mathbf{R}_A$ is the coordinate of nucleus A, whereas r_i is the coordinate of electron i.

Because electronic structure is the key to understand many chemical problems, a variety of approximation techniques have been proposed in the past years. The most popular approximated methods can be divided into the wave function theory (WFT) based methods also known as *ab-initio* methods, and the density functional theory based methods (DFT).
One of the earliest WFT approximation has been Hartree-Fock[3;4] (HF). In this theory, the electronic wavefunction is represented by a single Slater determinant,[4] and every electron is considered to be moving in an average field of all the other electrons and nuclei. The Hartree-Fock wavefunction ($|\Phi_{\mathrm{HF}}\rangle$) is a product of n single-electron wavefunctions $|\varphi_i\rangle$ also called molecular orbitals (MOs). To apply the HF approximation in practice, one needs to choose an explicit form for the orbitals $|\varphi_i\rangle$. In general, the linear combination of atomic basis functions ($|\chi_i\rangle$) expansion[5] is made:

$$|\varphi_i\rangle = \sum c_{iq}|\chi_q\rangle \tag{2.3}$$

The solution of the Schrödinger equation is found by iterating a trial wave function with a Self-Consistent Field (SCF) method. At each iteration a more accurate mean field is obtained until the HF energy (E_{HF}) converges.
A key issue of the HF method, and more generally of all the approximate solutions of the Schrödinger equation, is the electron correlation energy $\varepsilon_{\mathrm{corr}}$. This energy is usually defined as the difference between the exact non-relativistic energy (E_{exact}) and the HF energy[6] at the limit of a complete basis set:

$$\varepsilon_{\mathrm{corr}} = E_{exact} - E_{\mathrm{HF}} \tag{2.4}$$

and has a huge effect on the final results and represents a bottleneck to high accuracy. Usually, correlation energy is divided into two types of interactions:[7] *static correlation*, and *dynamic correlation*. Static correlation arises from near degeneracy of several configurations, and become important whenever a single Slater determinant is inadequate to represent the ground state of the system. Dynamic correlation is due to the tendency of electrons to avoid one another at short distances to minimize the repulsion, or due to their correlated motion at longer distances leading to dispersion forces. Normally, the WFT approaches describe very well the static correlation energy, and depending on the method, they can properly describe the dynamic correlation as well. On the other hand WFT methods become very computational demanding when the size of the system increases.
DFT based methods have a more favorable scaling of computationally resources with respect to the system size, and usually describe very well the dynamic correlation. On the other hand, they fail when the system undergoes bond breaking or bond formations, when static correlation effects become important. In these circumstances, the use of multiconfigurational methods is advisable for the accurate description of the system.

2.1.1 The CI and MC-SCF methods

The main limitation of the HF theory consists of neglecting the correlation among electronic motion even if the SCF method accounts for interelectronic repulsion through the Coulomb $\hat{J}$ and exchange $\hat{K}$ operators.[3;4] Obviously, a single determinantal function, or more generally a configuration state function[8] (CSF), cannot represent the true eigenfunction of the system, even for closed shell molecules, specially in chemical reactivity (when bonds are broken and formed) but also in highly excited electronic states in which a single configuration is inadequate. Two methods have been proposed in order to cope with that problem: Configuration Interaction (CI), and Multi-Configurational Self Consistent Field (MC-SCF).
In the CI method[9–13] the electronic wavefunction $|\Phi^{el}\rangle$ is a multiconfigurational function expanded in a sum of CSFs $|\Phi_i\rangle$:

$$|\Phi^{el}\rangle = \sum_i C_i |\Phi_i\rangle \tag{2.5}$$

in which the coefficients C_i are determined using a variational procedure, i.e. by minimizing the total energy given by

$$E = \frac{\sum_{i,j} C_i^* C_j \int \langle \Phi_i^* | \hat{H}^{\mathrm{el}} | \Phi_j \rangle}{\sum_{i,j} \langle \Phi_i^* | \Phi_j \rangle} \tag{2.6}$$

In a full CI (FCI) approach the sum (2.5) is extended to all the possible CSFs that can be built by taking into account all the possible electronic excitations to the different molecular orbitals of the system. Therefore, a FCI wavefunction will consist of a large number of $|\Phi_i\rangle$ terms. For example, for the H_2O molecule, using a DZ basis[4] the CI eigenfunction will consist of about 250,000 configurations. Thus, a full CI calculation is possible only for fairly small systems and by truncating the list of considered configurations to the only configurations contributing significantly to the wavefunction. In this way, a simpler CI scheme is the Single and Double Configuration Interaction (CISD), in which only the singly and doubly excited configurations are included. However, a truncated CI is not "*size consistent*".[†] In the alternative MC-SCF method, a simultaneous optimization of both C_i coefficients of (2.5) among the various configurations, and c_{iq} coefficients of the basis function.The simultaneous optimization of both sets of coefficients makes the MC-SCF procedure extremely heavy. For this reason quite often in the (2.5) expansion one considers only the configurations obtainable from a limited number of molecular orbitals (active or valence orbitals). For instance, in the CASSCF method[14] the number of CSFs is reduced by dividing the molecular orbitals in three sets: the inactive sets (orbitals doubly occupied

[†]A method is said "*size consistent*" when the energy computed for a molecular system by bringing two of its subsystems (say A and B) at infinite distance is equal to the sum of that of the two subsystems A and B computed as separate systems

in all the CSFs), the virtual set (the non occupied orbitals in all CSFs), and the active set. Usually, the number of electrons inside the active set is specified as well, forming the so called *active space* (N,M), where N is the number of electrons and M is the number of orbitals in the active space. Inside this space a FCI is performed using the given number of electrons and the given number of orbitals. A critical issue of this method is the choice of the active space, in other words, which orbitals and how many electrons have to be included. For small molecules a usual choice is to take all the valence orbitals (full valence CAS), however in other types of molecules the selection of the active space is not straightforwards and requires a certain amount of chemical intuition.
Often the MC-SCF calculation is the first step of a two-stage calculation. This second stage is very important because usually the MC-SCF methods cannot provide accurate results unless the dynamic correlation is explicitly included. To this end, a common approach is to perform an additional calculation with the second-order perturbation theory (PT2), starting from the unperturbed CASSCF optimized wavefunction, leading to the CASPT2 method.[15;16] In perturbation theory the hamiltonian is $\hat{H}^{el}$ is partitioned into a part $\hat{H}_0$ with a known solution $|\Phi^{(0)}\rangle$ and a part $\hat{H}'$ that acts as a perturbation on $|\Phi^{(0)}\rangle$. In this framework, the electronic time-independent Schrödinger equation (2.1) can be rewritten for a particular CSF:

$$\left(\hat{H}_0 + \lambda\hat{H}'\right)|\Phi_i\rangle = E_i|\Phi_i\rangle \tag{2.7}$$

$$\hat{H}_0|\Phi_i^{(0)}\rangle = E_i^{(0)}|\Phi_i^{(0)}\rangle \tag{2.8}$$

where λ is a dimensionless small parameter. By expanding both the electronic wavefunction $|\Phi_i\rangle$ and the energy E_i in powers of λ

$$|\Phi_i\rangle = |\Phi_i^{(0)}\rangle + \lambda|\Phi_i^{(1)}\rangle + \lambda^2|\Phi_i^{(2)}\rangle + ... \tag{2.9}$$

$$E_i = E_i^{(0)} + \lambda E_i^{(1)} + \lambda^2 E_i^{(2)} + ... \tag{2.10}$$

and inserting in equation (2.8), one arrives at the system of equations that allow the determination of the terms $|\Phi_i^{(n)}\rangle$ and $E_i^{(n)}$ order by order:

$$\lambda^0: \quad \hat{H}_0|\Phi_i^{(0)}\rangle = E^{(0)}|\Phi_i^{(0)}\rangle \tag{2.11}$$

$$\lambda^1: \quad \hat{H}_0|\Phi_i^{(1)}\rangle + \hat{H}'|\Phi_i^{(0)}\rangle = E^{(0)}|\Phi_i^{(1)}\rangle + E^{(1)}|\Phi_i^{(0)}\rangle \tag{2.12}$$

...

$$\lambda^n: \quad \hat{H}_0|\Phi_i^{(n)}\rangle + \hat{H}'|\Phi_i^{(n-1)}\rangle = \sum_{m=0}^{n} E_i^{(n)}|\Phi_i^{(n-m)}\rangle \tag{2.13}$$

The energy contribution up to the second-order can be computed if the zero-order eigenfunction $|\Phi_i^{(0)}\rangle$ is known:

$$E_i^{(0)} = \langle\Phi_i^{(0)}|\hat{H}_0|\Phi_i^{(0)}\rangle \tag{2.14}$$

$$E_i^{(1)} = \langle\Phi_i^{(0)}|\hat{H}'|\Phi_i^{(0)}\rangle \tag{2.15}$$

$$E_i^{(2)} = -\sum_{j\neq i}\frac{\left|\langle\Phi_i^{(0)}|\hat{H}'|\Phi_j^{(0)}\rangle\right|^2}{E_j^{(0)}-E_i^{(0)}} \tag{2.16}$$

There exist different approaches on how to define the zeroth-order hamiltonian $\hat{H}_0$ when using a CASSCF wave function as the reference function $|\Phi_i^{(0)}\rangle$. In CASPT2 this is defined as:

$$\hat{H}_0 = \hat{\mathcal{P}}_0\hat{\mathcal{F}}\hat{\mathcal{P}}_0 + \hat{\mathcal{P}}_K\hat{\mathcal{F}}\hat{\mathcal{P}}_K + \hat{\mathcal{P}}_{SD}\hat{\mathcal{F}}\hat{\mathcal{P}}_{SD} \tag{2.17}$$

where $\hat{\mathcal{P}}$ is the projection operator[15;16] and $\hat{\mathcal{F}}$ is the Fock operator.[4] The aim of the projector operators is to project on the CASSCF wavefunction ($\hat{\mathcal{P}}_0$) and all the single and double excitations inside ($\hat{\mathcal{P}}_K$) and outside ($\hat{\mathcal{P}}_{SD}$) the active space. As an extension to CASPT2, there exist also a CASSCF-based perturbation theory method such as the second-order n-electron valence state perturbation theory (NEVPT2), where two electron terms are included in the reference hamiltonian.[17–19]
Both CASSCF and CASPT2 are suitable methods for ground and excited state calculations. To get a more balanced treatment of several states, is possible to perform a State-average CASSCF (SA-CASSCF)[20] and Multi-State CASPT2 (MS-CASPT2).[21]

2.1.2 The DFT method

For large systems and a very large number of molecular geometries, DFT[22;23] provides a versatile and practical means to calculate electronic energies because of the more favorable scaling compared to CI and MC-SCF methods. The key quantity of DFT is the electronic density $\rho(\mathbf{r})$ (the number of electrons per unit volume in a given space point) which replaces the electronic wavefunction $|\Phi^{el}\rangle$. The problem of determining the wavefunction as in the WFT methods is now redressed with that of the electronic density, leveraging on the simple idea that the electronic system of a molecule behaves as a gas of particles subject to coulombian interactions (v_{ext} for the nuclei of the molecule and v_{ee} for the electrons themselves). This concept has been formalized by the Hohenberg-Kohn theorems, stating that:[24]

1. *the external potential v_{ext} depends on the electronic density $\rho(\boldsymbol{r})$ of the ground state.*

2. *the electronic density of the ground state (ρ_0) can be computed using variational methods.*

Accordingly, $\rho(\mathbf{r})$ can be easily related to the total number of electrons n

$$\int \rho(\mathbf{r})\mathrm{d}\mathbf{r} = n \tag{2.18}$$

and determines the wavefunction of the ground state as well as the related electronic energy that is formulated as

$$E[\rho] = T_e[\rho] + V_{ext}[\rho] + V_{ee}[\rho] \tag{2.19}$$

where $T_e[\rho]$ is the kinetic energy, $V_{ext}[\rho]$ the electron nucleus attractive energy and $V_{ee}[\rho]$ the electron electron repulsive energy. The computational scheme of DFT is embodied into the Kohn-Sham equations (KS-DFT).[22] The effect of the interaction among n interacting electron is rendered as that of the same number of non interacting electron subject to an external potential. In KS-DFT the total energy can be written as:

$$E[\rho] = T_s[\rho] + V_{ext}[\rho] + J_{ee}[\rho] + E_{ex}[\rho] \tag{2.20}$$

where $T_s[\rho]$ is the energy associated to a gas of non interacting electrons ($T_s[\rho] = \sum_i^N \langle\psi_i| - \frac{1}{2}\nabla^2|\psi_i\rangle$), $J_{ee}[\rho]$ is the Coulomb energy, $V_{ext}[\rho]$ is the interaction energy with the external potential v_{ext} with density ρ

$$V_{ext}[\rho] = \int \rho(\mathbf{r}) v_{ext}(\mathbf{r}) d\mathbf{r} \tag{2.21}$$

The last term $E_{ex}[\rho]$ called exchange-correlation energy[25] is unknown and contains the differences between the independent electron gas model and the real system including the non classical part of V_{ee}.
By applying the variational principle to the energy formulation (2.20) one gets n separated Kohn-Sham monoelectronic equations to be solved using an iterative SCF-like procedure:

$$\left[-\frac{\hbar^2}{2m}\nabla^2 + v_{\mathrm{eff}}(\mathbf{r})\right]\phi_i(\mathbf{r}) = \varepsilon_i\phi_i(\mathbf{r}) \tag{2.22}$$

where $v_{\mathrm{eff}}(\mathbf{r}) = v_{ext}(\mathbf{r}) + j_{\mathrm{ee}}(\mathbf{r}) + v_{\mathrm{ex}}(\mathbf{r})$. The first two terms v_{ext} and j_{ee} are known, whereas the third term v_{ex} called exchange-correlation potential, is unknown. Like in the Hartree-Fock theory the polyelectronic problem leads to the resolution of n monoelectronic equations. However, while in the HF theory the electronic correlation effects are introduced either through MC-SCF methods or by expanding the polyelectronic wavefunction in Slater determinants, DFT directly embeds the dynamical effects of the electronic correlation, although it ignores almost all static correlation effects.
Several approximated exchange-correlation functionals[25] have been proposed in the past years to compute the unknown energy E_{ex}. The most basic approach is the Local-Density

Approximation (LDA), where the energy depends on the electron density of a uniform gas. The Local Spin-Density Approximation (LSDA) is a generalization of the LDA in order to include electron spin. A better estimation of E_{ex} is usually achieved by including not only information on the local density ρ but also the gradient of the density ($\nabla\rho$) as well, in order to account for the non-homogeneity of the density in real systems: this is called Generalized Gradient Approximation (GGA). As a logical extension of GGA, the exchange-correlation energy can be allowed to depend on higher order derivatives of the electron density. In particular, the meta-GGA functionals use the Laplacian of the density ($\nabla^2\rho$) to evaluate E_{ex}. The last way to approximate E_{ex} adopts an hybrid approach where the exchange-correlation energy depends on ρ, $\nabla\rho$, $\nabla^2\rho$ plus one part of the HF exchange-correlation energy. In this case, the functionals are divided into two classes: hybrid-GGA and meta-hybrid-GGA according to origin of the non HF part.

2.1.3 Description of the Excited States: TD-DFT

Time-dependent density functional theory (TD-DFT)[26–29] extends the basic ideas of the ground-state DFT to the treatment of excited states and time-dependent phenomena in general. In this case the the basic variable is the the time-dependent one-body electron density $\rho(\mathbf{r},t)$. The standard way to obtain such time dependent density is through a modified version of the Kohn-Sham equation (2.22) rewritten in terms of the time-dependent Schrödinger equation:

$$i\frac{\partial}{\partial t}\phi_i(\mathbf{r},t) = \left[-\frac{\nabla^2}{2} + v_{\text{eff}}(\mathbf{r},t)\right]\phi_i(\mathbf{r},t) \tag{2.23}$$

The full solution of equation (2.23) is quite difficult numerically. However, there are approximate frameworks that circumvent the direct solution of this equation. Indeed, within the framework of the adiabatic approximation and the linear response theory, the equation can be recast as a pseudo-eigenvalue form:[30]

$$\begin{bmatrix} \mathbf{A} & \mathbf{B} \\ \mathbf{B}^* & \mathbf{A}^* \end{bmatrix}\begin{bmatrix} \mathbf{X} \\ \mathbf{Y} \end{bmatrix} = \omega \begin{bmatrix} \mathbf{1} & \mathbf{0} \\ \mathbf{0} & \mathbf{-1} \end{bmatrix}\begin{bmatrix} \mathbf{X} \\ \mathbf{Y} \end{bmatrix} \tag{2.24}$$

where ω are the vertical excitation energies, whereas the form of the matrices $\mathbf{A}$ and $\mathbf{B}$ depends on the nature of the functional used for the TD-DFT calculation. It is also possible to derive an operator whose eigenvalues are the square of the excitation energies, thereby reducing the dimension of the matrix equation 2.24:

$$(\mathbf{A}-\mathbf{B})^{1/2}(\mathbf{A}+\mathbf{B})(\mathbf{A}-\mathbf{B})^{1/2}\mathbf{Z} = \omega^2\mathbf{Z} \tag{2.25}$$

with $\mathbf{Z} = (\mathbf{A} - \mathbf{B})^{1/2}(\mathbf{X} + \mathbf{Y})$. Linear response is a good approximation when the electronic structure in the excited states does not change drastically with respect to the electronic structure of the ground state. The method is thus suitable for the computation of UV-visible absorption spectra, where the bands experimentally observed are the result of electronic excitations from valence occupied to valence virtual orbitals. In this case the core electronic structure is practically unmodified in these valence electronic transitions, i.e. the inner electronic structure of the ground and excited states is very similar.

2.2 A Surface Hopping method: the SHARC Procedure

The treatment of full-dimensional nuclear motion of large molecules with accurate quantum mechanical methods can be very expensive, and in many case unfeasible. To a large extent, this is due to the exponential increase of computational cost as soon as more degrees of freedom are included in the molecular model. For these reasons, during the past years many efforts have been devoted to the development of mixed quantum-classical methods, capable of describing the molecular dynamics of large systems at a reasonable computational cost. In this way, one of the most developed approach has been surface hopping (SH),[31] where electrons are treated quantum mechanically, whereas nuclear motion is treated classically. However, the SH method in its original formulation[31] ignores non-adiabatic effects necessary to simulate ISC. Therefore, a generalization of the standard SH model called Surface Hopping with ARbitrary Couplings (SHARC),[32–35] has been developed and successfully used to investigate the photochemical properties of various systems.[36–42] Indeed, through this new method and the related software `SHARC 2.0`,[35] is possible to perform full dimension surface hopping dynamics simulations including any arbitrary coupling between electronic states. For instance, with the introduction of spin-orbit coupling (SOC), the program can accurately describe ISC between states of different multiplicity. Several file-based interfaces allow SHARC to work with several quantum chemistry packages such as the Amsterdam Density Functional (ADF) used to perform all the DFT/TD-DFT dynamics simulations carried out during this PhD thesis.
In SHARC, and more generally in all SH methods, the electrons are represented by a time-dependent wavefunction $|\Phi^{el}(t)\rangle$ written as a linear combination of electronic basis states, $\{|\Psi_a\rangle\}$:

$$|\Phi^{el}(t)\rangle = \sum_{\alpha}^{n} c_\alpha(t)|\Psi_\alpha\rangle \tag{2.26}$$

The time evolution of the total wavefunction is ruled by the time-dependent Schrödinger equation:

$$i\frac{d}{dt}|\Phi^{el}(t)\rangle = \hat{H}^{tot}|\Phi^{el}(t)\rangle \tag{2.27}$$

where $\hat{H}^{el}$ is the total hamiltonian of the system, usually written as the sum of two separated contributions:

$$\hat{H}^{tot} = \hat{H}^{\mathrm{MCH}} + \hat{H}^{\mathrm{add}} \tag{2.28}$$

where $\hat{H}^{tot}$ is the standard coulomb molecular hamiltonian defined in Equation 2.2 and and $\hat{H}^{\mathrm{add}}$ is a generic coupling hamiltonian. In this thesis, $\hat{H}^{\mathrm{add}}$ is the spin-orbit hamiltonian $\hat{H}^{\mathrm{SOC}}$ as we want to include the description of ISC in the dynamics simulations (see Chapter 6).
By inserting Equation 2.26 in Equation 2.27 and multiplying by $\langle\Psi_a|$, one obtains the equation of motion of the wave function coefficients:

$$\frac{\partial}{\partial t}c_\alpha = \sum_\gamma \left[iH_{\alpha\gamma} + \mathbf{v}\cdot\mathbf{K}_{\alpha\gamma}\right] c_\gamma \tag{2.29}$$

where $H_{\alpha\gamma} = \langle\Psi_\alpha|\hat{H}^{\mathrm{total}}|\Psi_\gamma\rangle$ is the total hamiltonian matrix, $\mathbf{v}$ is nuclear velocity vector, and $\mathbf{K}_{\alpha\gamma} = \langle\Psi_\alpha|\frac{\partial}{\partial\mathbf{R}}|\Psi_\gamma\rangle$ is the non adiabatic coupling vector (NAC). These matrix elements can be computed using the eigenfunctions of the hamiltonian (2.2) $\{|\Psi_a^{\mathrm{MCH}}\rangle\}$, normally chosen as few lowest singlet and triplet excited states obtained from a quantum chemistry software. However, in this basis the hamiltonian matrix $H_{\gamma\alpha}^{\mathrm{MCH}} = \langle\Psi_\gamma|\hat{H}^{\mathrm{total}}|\Psi_\alpha\rangle$ is not diagonal due to the $\hat{H}^{\mathrm{add}}$ term and furthermore the SOC are usually delocalized over the entire potential energy surface. This fact can lead to non-zero transition probability also in the regions far away from the PES crossing regions. Hopefully, it is possible to diagonalize the hamiltonian with an appropriate unitary transformation $\mathbf{U}$:

$$\mathbf{H}^{\mathrm{diag}} = \mathbf{U}^\dagger\mathbf{H}^{\mathrm{MCH}}\mathbf{U} \tag{2.30}$$

obtaining eigenenergies (diagonal elements in $\mathbf{H}^{\mathrm{diag}}$) and eingenstates:

$$|\Psi_\gamma^{\mathrm{diag}}\rangle = \sum_\alpha |\Psi_\alpha^{\mathrm{MCH}}\rangle U_{\alpha\gamma} \tag{2.31}$$

in a new basis called diagonal representation (diag). Accordingly, in this basis the equation of motion 2.29 becomes:

$$\frac{\partial}{\partial t}\mathbf{c}^{\mathrm{diag}} = -\left[i\mathbf{U}^\dagger\mathbf{H}^{\mathrm{MCH}}\mathbf{U} + \mathbf{v}\cdot\mathbf{U}^\dagger\mathbf{K}^{\mathrm{MCH}}\mathbf{U} + \mathbf{U}^\dagger\frac{\partial\mathbf{U}}{\partial t}\right]\mathbf{c}^{\mathrm{diag}} \tag{2.32}$$

The main advantage of the diag representation is that all the couplings are now localized, as they become large only in regions where two potential energy surfaces become near-degenerate.[33] However, the derivative $\mathbf{U}^\dagger\frac{\partial\mathbf{U}}{\partial t}$ is notably very difficult to compute because $\mathbf{U}$ is not uniquely defined, and furthermore it might change very rapidly near the points of near-degeneracy. In order to avoid the computation of this term, in SHARC the

wavefunction is propagated using the three-step propagator:[33]

$$\mathbf{c}^{\mathrm{diag}}(t+\Delta t) = \left[\mathbf{U}^{\dagger}(t+\Delta t)\mathbf{P}^{\mathrm{MCH}}(t+\Delta t,t)\mathbf{U}(t)\right]\mathbf{c}^{\mathrm{diag}}(t) \tag{2.33}$$

where $\mathbf{P}^{\mathrm{MCH}}(t+\Delta t,t) = \exp\left[-i\mathbf{H}^{\mathrm{MCH}} + \mathbf{vK}^{\mathrm{MCH}}\right]$ is the propagator. This quantity can be obtained by integration of $\mathbf{H}^{\mathrm{MCH}}$ and $\mathbf{vK}^{\mathrm{MCH}}$ with the local diabatization procedure[43] which does not require NACs, but uses the overlap matrix $\mathbf{S}^{\mathrm{MCH}}$ between states of subsequent time steps:[44]

$$S^{\mathrm{MCH}}_{\alpha\gamma}(t,t+\Delta t) = \langle \Psi^{\mathrm{MCH}}_{\alpha}(t) | \Psi^{\mathrm{MCH}}_{\gamma}(t+\Delta t)\rangle \tag{2.34}$$

The use of local diabatization offers several advantages compared to the standard integration methods typically used to calculate the propagator $\mathbf{P}^{\mathrm{MCH}}$. Indeed, it has been demonstrated that this algorithm is very stable even where the NACs are extremely narrow and large,[44] and furthermore it allows the propagation of the wavefunction even when the quantum chemistry programs coupled with SHARC do not offer NACs.
Using the diag representation requires also the transformation of the MCH gradients $\nabla_{\mathbf{R}} H_{\alpha}{}^{\mathrm{MCH}}$ through the formula:

$$\nabla_{\mathbf{R}} H^{\mathrm{diag}}_{\alpha} = \sum_{i}^{n}\sum_{j}^{n} U^{*}_{i\alpha}U_{j\alpha}\left[\nabla_{\mathbf{R}} H^{\mathrm{MCH}}_{j}\delta_{ij} - (H^{\mathrm{MCH}}_{ii} - H^{\mathrm{MCH}}_{jj})\mathbf{K}^{\mathrm{MCH}}_{\alpha\alpha}\right] \tag{2.35}$$

The nuclear motion is ruled by the classical Newton equations of motion:

$$M_A \frac{\partial^2 \mathbf{R}_A}{\partial t^2} = -\nabla_{\mathbf{R}} H^{\mathrm{MCH}}_{\beta} \tag{2.36}$$

where M_A and $\mathbf{R}_A$ are the mass and the coordinate of the atom A. The nuclei move as a classical trajectory, with the motion constantly related to the quantum part through the gradient of the electronic energy $-\nabla_{\mathbf{R}} H^{\mathrm{MCH}}_{\beta}$. To determine this active state, SHARC uses by default a modified version[43**?**] of the "fewest switches" formula,[31] based on analysis of population coefficients $|c_a(t)|^2$:

$$h_{\beta\to\alpha} = \left(1 - \frac{|c_{\beta}(t+\Delta t)|^2}{|c_{\beta}(t)|^2}\right)\frac{\Re\left[c_{\alpha}(t+\Delta t)P^{*}_{\alpha\beta}c^{*}_{\beta}(t)\right]}{|c_{\beta}(t)|^2 - \Re\left[c_{\beta}(t+\Delta t)P^{*}_{\beta\beta}c^{*}_{\beta}(t)\right]} \tag{2.37}$$

Then, a stochastic algorithm is used to determine the active state.[33] If the active state has changed, a so-called *surface hop* is performed. As a consequence of the stochastic process involved and also to mimic the branching of a wave-packet, SHARC requires an ensemble

of trajectories, each one starting from a different initial condition.

2.3 Optimization of the ADF Program Package

2.3.1 Motivation

The assignment in SCM consisted in the optimization and implementation of new features in the quantum chemistry program package Amsterdam Density Functional (ADF),[45;46] directly developed and maintained by SCM. The aim of such modifications was to speed up the TD-DFT electronic structure calculations, performed on-the-fly during the propagation of the SHARC trajectories. Indeed, the original design of the ADF code was not intended for running such semiclassical dynamics simulations within the SHARC scheme. In particular, the calculation of the potential energy surface gradients at each time step turned out to be very inefficient. In paragraph 2.2 it has been shown how SHARC propagates the electronic wavefunction in the diag basis and how such representation requires appropriate transformations of several quantities from MCH to diag basis and vice versa. In particular, the transformation formula of the gradients shown in Equation 2.35 says that all the n_s MCH gradients are needed to get a single diagonal gradient at each time step t_i. This particular scheme represents a bottleneck for the quantum chemistry calculations, because the original ADF program was intended to compute one single MCH gradient for each DFT/TD-DFT calculation, because of the standard geometry optimization on a specific electronic state. Therefore, in the first implementation of the SHARC↔ADF interface, this problem has been overcome by repeating n_s times the DFT and TD-DFT single point calculations at the same geometry, each time asking for a different MCH gradient, and eventually collecting the n_s MCH gradients needed for the SHARC dynamics. This procedure is schematically shown in Figure 2.1. However, this brute force approach results

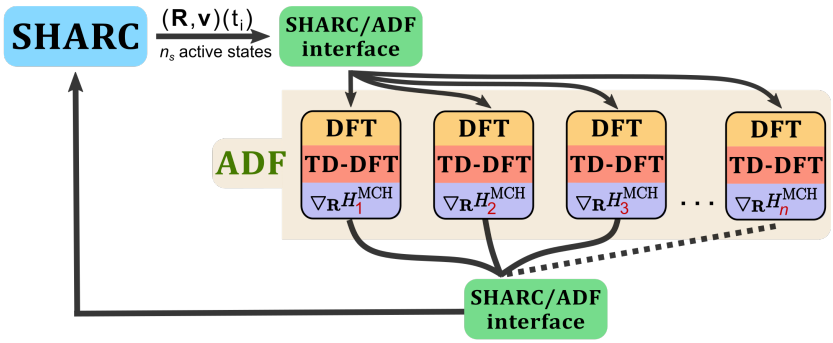

Figure 2.1 Typical workflow diagram used with the old version of ADF. At each propagation step t_i, the SHARC↔ADF interface calls ADF several times, each time asking for a different MCH gradients.

to be computationally very inefficient, since performing DFT and TD-DFT multiple times

on the same unchanged geometry, outputs the same the same identical information for the DFT and TD-DFT parts. For instance, a typical DFT/TD-DFT energy calculation for the trans-$[RuClPy_4(NO)]^{2+}$ system takes 15 minutes for 3 singlet and 3 triplet excited states, whereas it takes 7 minutes to get one MCH gradient. Thus, in order to collect all the gradients, ADF needs to be called six times, resulting in (15+7)×6=132 min for one single time step calculation. However without repeating the DFT/TD-DFT single point calculations, the total time required is 15+(7×6)=57 min, gaining approximately 75 minutes for each propagation step. Moreover, note that this value needs to be multiplied by the total number of propagation steps and the total number of trajectories. For a 1000 fs simulation, a propagation step of 0.5 fs, and 100 trajectories, the total amount of wasted time is $75\text{min} \times 2000 \times 100 = 250000\text{h}$.
Accordingly, the first task consisted in a proper restructuring of the ADF source code, in order to enable the calculation of all the gradients with a single DFT and TD-DFT call, as shown in Figure 2.2, and thus significantly improving the efficiency of the SHARC/ADF dynamics. This new feature will be hereafter called *multiple gradients*.

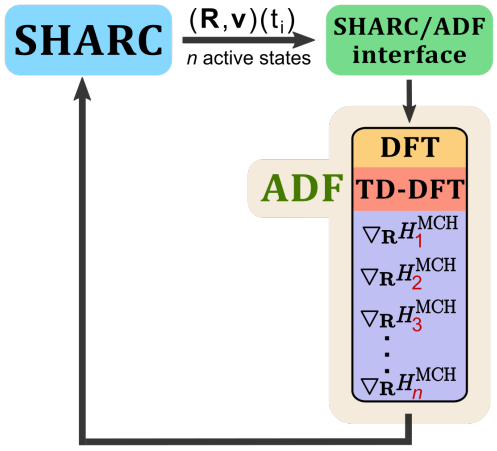

Figure 2.2 Workflow diagram used with the version of ADF. At propagation step t_i, the SHARC↔ADF interface calls ADF, which provides all the MCH gradients in one calculation.

The second important modification in the ADF source code, concerns the possibility to inquire an independent number of singlet and triplet excited states when performing a TD-DFT calculation. In the older versions of ADF, the user can specify how many singlet and triplet excitation energies should be calculated by TD-DFT. However, no other keywords exist to specify an independent number of singlet and triplet states, so the user gets inevitably the same number of singlet and triplet excited states. This limitation of the program represents again a disadvantage when facing the on-the-fly electronic calculations within the SHARC scheme, as in many occasions the photochemistry develops on a different number of singlet and triplet states. For instance, in case of the trans-$[RuClPy_4(NO)]^{2+}$ molecule, the photodynamics develops on the first two singlet

excited states S_1 and S_2 and the first three triplet states T_1, T_2, and T_3. Accordingly, the possibility to inquire only for the needed number of singlets and triplets enhances the efficiency of the whole dynamics calculation. This new feature will be hereafter called *independent number of singlets and triplets*.

2.3.2 Multiple Gradients

The development of the multiple gradients required the creation of two new Fortran subroutines `ReadRep2DoGrad` and `FindStates2DoGrad`, and the modification of two existing files:

- `Do_gradients` (the main routine)
- `ego_config` (reads keywords in the input file)

The implementation affected the `EXCITEDGO` section in the ADF input file. In the old versions, this keyword enables a geometry optimization in a particular excited state. However, if the `GRADIENT` keyword is specified before the `EXCITEDGO` section, the optimization is skipped and only the gradient is computed. In the new version of ADF, the `EXCITEDGO` block accepts three new subkeys, **`SING_GRAD`**, **`TRIP_GRAD`**, and **`ALL_GRADIENTS`**, which give much more flexibility for the gradient computation. The first two subkeys need a list of characters and numbers, which specify the symmetry and the excited states for which the gradients will be calculated. For instance, if the gradients of the states S_1(A1), S_2(A1), S_2(B2), T_1(A1), T_3(A1) are needed, the user will input:

```
GRADIENT
EXCITEDGO
  SING_GRADS
     A1 1 2
     B2 2
  SUBEND
  TRIP_GRADS
     A1 1 3
  SUBEND
END
```

The third keyword `ALL_GRADIENTS` has no arguments, as it reads the excitation data from the previous TD-DFT calculation and computes the gradients for all the available excited states. Note that these new features do not prevent the user to perform a regular excited state geometry optimization with the standard `EXCITEDGO` subkeys detailed in the

ADF manual.
The allocation of the new user data has been entrusted to the two new subroutines: `ReadRep2DoGrad` and `FindStates2DoGrad`, which read and allocate the necessary information form the input file. The first routine is called when either `SING_GRADS` or `TRIP_GRADS` subkeys are specified, whereas the second one is called when `ALL_GRADIENTS` is found. Both subroutines store the data into a Fortran array called `ego_input`, declared as `ego_input_type` derived datatype. This array normally holds all the information needed to determine which gradient has to be computed in case of a geometry optimization. To let the new implementation working, this derived datatype has been modified with the addition of two elements (`ngrad_tot` and `nrep_tot`), which contain the total number of irreducible representations and gradients that are going to be computed. In a nutshell, the most important elements of the datatype are:

```
type ego_input_type
 [...]
  integer(KINT) :: irrep = 1     ! Symmetry of the transition
  integer(KINT) :: istate(20)    ! Multi gradients states array
  integer(KINT) :: nstates = 1   ! Tot number of states per irrep
  character(2)  :: spin = 'SS'   ! SS or ST
  integer(KINT) :: ngrad_tot = 0 ! Total number of gradients
  integer(KINT) :: nrep_tot  = 0 ! Total number of irreps
 [...]
end type ego_input_type
```

Note that `istate` is now an array nested into the datatype that contains list of excited states for which the gradients will be calculated.
The next step of the implementation consisted in the modification of the `ego_config` subroutine. This routine searches for the all the keywords that can be specified within the `EXCITEDGO` block and calls the proper subroutine according to the keyword that has been found. Few lines were added in order to let the program to recognize the three new subkeys and to call the appropriate subroutine:

```
[...]
else if (contns(buf, 'SING_GRADS')) then
   call ReadRep2DoGrad(ego_input, 'SS')
else if (contns(buf, 'TRIP_GRADS')) then
   call ReadRep2DoGrad(ego_input, 'ST')
else if (contns(buf, 'ALL_GRADIENTS')) then
   call FindStates2DoGrad(ego_input)
[...]
```

The subroutine checks as well the consistency of the keyword inserted by the user, and stops the execution in case the user entered the wrong combination of keywords or simply misspell one of them.
Once the input data has been read and stored, the gradients can be computed. This task is assigned to the main routine `Do_gradients` which calls the `ego_config` subroutine before starting the gradient computation. The crucial part for the multiple gradient computation is the double do loop:

```
do irep = 1, ego_input(1)%nrep_tot + 1
 do igrad = 1, ego_input(irep)%nstates
  ego_input(irep)%nstate = ego_input(irep)%istate(igrad)
  egradc_tmp = egradc
  energy_tmp = energy

  if (DoExcitedGrads) then
     call ego_driver(curGeom, ego_input(irep), egradc_tmp, energy_tmp)
     gGeoupdata%genrgy(inow) = energy_tmp
  endif
[...]
 enddo
enddo
```

The do loops run over all irreducible representations (irep) and all the gradients (igrad) requested inside the *i*-th representation. Each gradient is printed into the ADF general result file TAPE21, which contains information about the calculation. The gradients can be found under the section `Excitation spin irrep`, where `spin` can be `SS` for a singlet gradient, or `ST` for a triplet gradient, whereas `irrep` is the irreducible representation to whom the electronic state belongs. Each gradient is preceded by an identifier `Gradients_CART n`, where `n` is the excited state number in the irreducible representation. For instance, the gradient of an excited state $T_2(^3B_{1u})$ can be found under the section:

```
Excitations ST B1.u
Gradients_CART 2
```

In case of a normal geometry optimization the two do loops cycle one time only, and compute the gradient needed by the geometry optimizer.
The multiple gradient algorithm is schematized in workflow diagram in Figure 2.3.

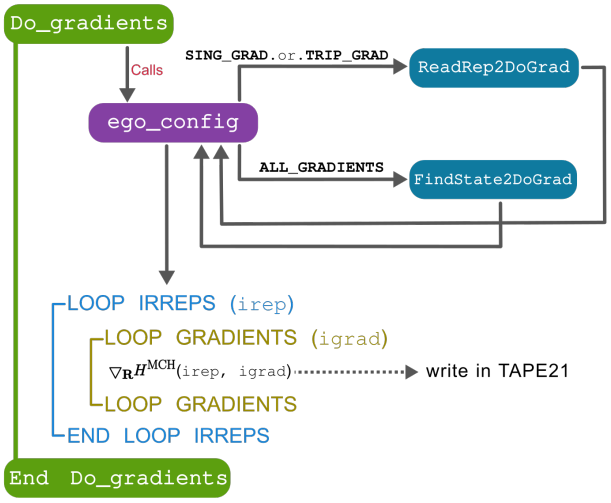

Figure 2.3 Workflow diagram of the multiple gradient algorithms.

2.3.3 Independent Number of Singlets and Triplets

Implementation of the independent number of singlets and triplets affected the `EXCITATION` block key in the ADF input file. This block performs singlet-singlet and singlet-triplet excited states calculations using TD-DFT. Several technical parameters, such as the diagonalization method (Exact, Davidson) or the number of excited state, can be handled by addressing additional subkeys in this data block. In particular, the `LOWEST nlowest` keyword performs a Davidson calculation, and through the integer `nlowest` it sets the number of singlet and triplet excited states that will be computed. This keyword is usually the most used one, as the Davidson diagonalization technique provides faster results than the Exact one, specially when working with large systems such as the trans-$[RuPy_4ClNO]^{2+}$ molecule. For this reason, the modifications that will be described in this paragraphs will concern the `LOWEST` subkey and the parts of source code directly related to the Davidson method.
The first step in the implementation has been the revision of the `LOWEST` keyword in the ADF input file. Indeed, in the new version this command can accept two integer numbers, one for each spin multiplicity. For instance, to request five singlet and six triplet excited states, the user can simply input:

```
EXCITATIONS
  Lowest 5 6
End
```

Nevertheless, the program still works in the standard way if the user specifies only one integer number. For instance, to request six singlets and six triplets, the user can input:

```
EXCITATIONS
  Lowest 6
End
```

In the ADF source code, several routines have been modified:

- `Excitation` (the main routine)
- `Set_Values` (reads and stores the user input data)
- `MakeLowest` (finds the lowest excitations)
- `allocDavidson` (performs the Davidson diagonalization)

In this case, the implementation required more conceptual efforts than practical modifications of the source code, since ADF already computes singlet and triplet excitations. After an accurate examination of the algorithms involved in the TD-DFT calculation, the bottleneck has been identified on the excited states data shared among the different subroutines. In particular, the data have been rearranged into two separate subsets, one related to the singlet and the other related to the triplet excited states. In the older version of the code, such information were stored into the integer `nlowest`, and into the 2-dimensional arrays `nsymdav(:,:)` and `lrep2dodavidson(:,:)`. Notably, `nsymdav` stores the number of energies for each irreducible representation and `lrep2dodavidson` stores the irreducible representations that will be calculated. However, the three variables own the same information for both singlet and triplet excited states. For this reason, an extra dimension has been added to take into account the different number of singlets and triplets. Therefore, the 2-dimensional arrays turn to 3-dimensional `nsymdav(:,:,2)` and `lrep2dodavidson(:,:,2)`, whereas the constant `nlowest` turns to a 1-dimension array `nlowest(2)`.
As a third step in the implementation, the subroutines have been adapted according to the new shape of the variables. New checks were added to the different subroutines, to manage possible errors in the input files. To handle the case where the `LOWEST` keyword is addressed with one integer, an if statement has been added in the `Excitation` routine, just before the

```
if(nspin==1) then
 lrep2dodavidson(:,:,2) = lrep2dodavidson(:,:,1)
         nsymdav(:,:,2) = nsymdav(:,:,1)
endif
```

Results are written in the output file and the in the general ADF result file TAPE21. The information can be found under the section `Excitations spin irrep` where `spin`

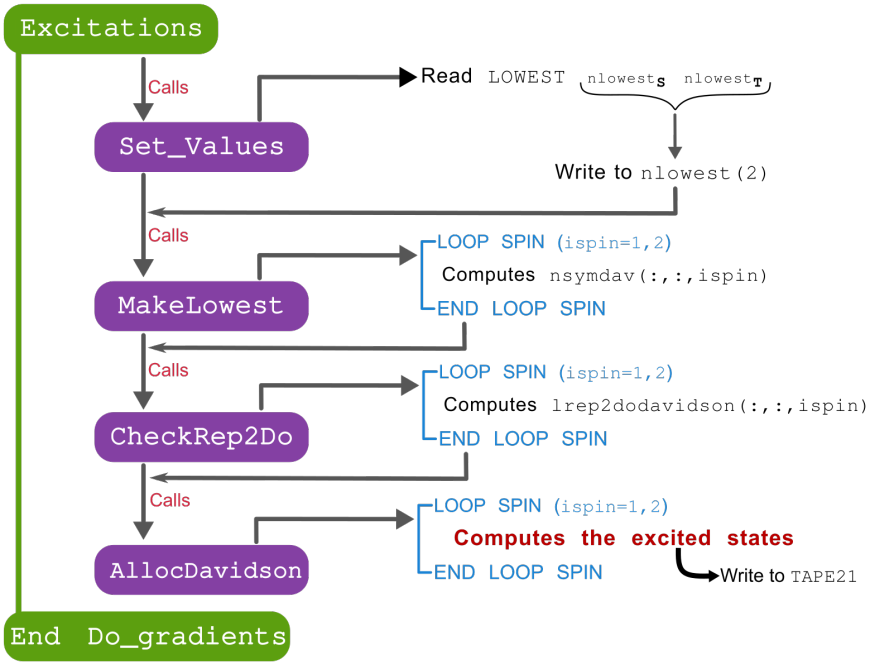

Figure 2.4 Workflow diagram used by the new version of ADF to compute the excited states.

can be `SS` or `ST` according to the transition type, either singlet-singlet or singlet-triplet, whereas irrep is the irreducible representation to whom the excitation belongs. The workflow for the computation of the excited states of the new version of ADF, is schematized in Figure 2.4.

2.3.4 Conclusions

Dynamics simulations are usually very expensive in terms of time and computational resources. For metal complexes systems such as the trans-$[RyPy_4ClNO]^{2+}$, an accurate investigation of the photodynamic properties requires an appropriate theoretical framework, able to accurately describe the photochemical transitions that can occur with metal complexes, such as non-radiative ISC and IC, at a reasonable computational cost. In this way, the combination of the SHARC molecular dynamics software package and the ADF quantum chemistry package provides a firm computational workflow for an accurate simulation of the photochemical properties of such ruthenium complexes. However, the original ADF code was not designed for running such non-adiabatic dynamics simulations withing the SHARC scheme. Indeed, with the old ADF version the on-the-fly computation of energies and gradients needed by the SHARC procedure is very inefficient. For this reason, the two months spent at SCM in Amsterdam focused to the optimization and improvement of the ADF source code. Implementation of the *multiple gradients* significantly improved the efficiency of the MCH gradients needed by SHARC, whereas

the implementation of the independent number of singlet and triplet states is not only useful for the SHARC simulations, but also for all ADF users that perform TD-DFT calculations. Indeed, this feature is particularly useful whenever the TD-DFT calculations are very computationally demanding, for instance when the size of the system is large.
In Chapter 6 we will detail the non-adiabatic dynamics with SHARC making use of the improved version of ADF. Thanks to the new features, the faster computational workflow made possible an extended propagation time of the trajectories up to 1 ps or more, that allowed for the observation of early photochemical processes.

Bibliography

[1] E. Schrödinger. An undulatory theory of the mechanics of atoms and molecules. *Phys. Rev.*, 28:1049–1070, 1926.

[2] M. Born and R. Oppenheimer. Zur quantentheorie der molekeln. *Annalen der Physik*, 389(20):457–484.

[3] J. C. Slater. *Quantum Theory of Matter, 2nd ed.* McGraw-Hill: New York, 1968.

[4] A. Szabo and N. S. Ostlund. *Modern Quantum Chemistry: Introduction to Advanced Electronic Structure Theory*. First edition, 1996.

[5] C. C. J. Roothaan. New developments in molecular orbital theory. *Rev. Mod. Phys.*, 23:69–89, 1951.

[6] P. O. Löwdin. The historical development of the electron correlation problem. *Int. J. Quantum Chem.*, 55(2):77–102.

[7] D. K. W. Mok, R. Neumann, and N. C. Handy. Dynamical and nondynamical correlation. *J. Phys. Chem.*, 100(15):6225–6230, 1996.

[8] J. E. Grabenstetter, T. J. Tseng, and F. Grein. Generation of genealogical spin eigenfunctions. *Int. J. Quantum Chem.*, 10(1):143–149.

[9] H. F. Scheafer. *Methods of Electronic Structure Theory*. Number pp 189-275. Plenum: New York, 1977.

[10] D. Wlodzislaw. Configuration interaction method: the past and future perspectives. *J. Mol. Struc.: THEOCHEM*, 234:27–49, 1991.

[11] I. Shavitt. The history and evolution of configuration interaction. *Mol. Phys.*, 94(1):3–17, 1998.

[12] C. D. Sherrill and H. F. Schaefer. The configuration interaction method: Advances in highly correlated approaches. volume 34 of *Advances in Quantum Chemistry*, pages 143–269. Academic Press, 1999.

[13] P. G. Szalay, T. Müller, G. Gidofalvi, H. Lischka, and R. Shepard. Multiconfiguration self-consistent field and multireference configuration interaction methods and applications. *Chem. Rev.*, 112(1):108–181, 2012. PMID: 22204633.

[14] B. O. Roos, P. R. Taylor, and P. E.M. Sigbahn. A complete active space SCF method (CASSCF) using a density matrix formulated super-ci approach. *Chem. Phys.*, 48(2):157–173, 1980.

[15] K. Andersson, P. A. Malmqvist, B. O. Roos, A. J. Sadlej, and K. Wolinski. Second-order perturbation theory with a CASSCF reference function. *J. Phys. Chem.*, 94(14):5483–5488, 1990.

[16] K. Andersson, P. A. Malmqvist, and B. O. Roos. Second-order perturbation theory with a complete active space self-consistent field reference function. *J. Chem. Phys.*, 96(2):1218–1226, 1992.

[17] K. G. Dyall. The choice of a zeroth-order hamiltonian for second-order perturbation theory with a complete active space self-consistent-field reference function. *J. Chem. Phys.*, 102(12):4909–4918, 1995.

[18] C. Angeli, R. Cimiraglia, and J.-P. Malrieu. On a mixed møller–plesset epstein–nesbet partition of the hamiltonian to be used in multireference perturbation configuration interaction. *Chem. Phys. Lett.*, 317(3):472 – 480, 2000.

[19] C. Angeli, R. Cimiraglia, S. Evangelisti, T. Leininger, and J.-P. Malrieu. Introduction of n-electron valence states for multireference perturbation theory. *J. Chem. Phys.*, 114(23):10252–10264, 2001.

[20] K. Ruedenberg, L. M. Cheung, and S. T. Elbert. MCSCF optimization through combined use of natural orbitals and the brillouin–levy–berthier theorem. *Int. J. Quantum Chem.*, 16(5):1069–1101.

[21] J. Finley, P. Malmqvist, B. O. Roos, and A. L. Serrano. The multi-state CASPT2 method. *Chem. Phys. Lett.*, 288:299–306, 1998.

[22] W. Kohn and L. J. Sham. Self-consistent equations including exchange and correlation effects. *Phys. Rev.*, 140:A1133–A1138, 1965.

[23] W. Kohn. Nobel lecture: Electronic structure of matter—wave functions and density functionals. *Rev. Mod. Phys.*, 71:1253–1266, 1999.

[24] P. Hohenberg and W. Kohn. Inhomogeneous electron gas. *Phys. Rev.*, 136:B864–B871, 1964.

[25] N. Schuch and F. Verstraete. Computational complexity of interacting electrons and fundamental limitations of density functional theory. 5:732–735, 2007.

[26] E.K.U. Gross and W. Kohn. *Time-Dependent Density-Functional Theory*, volume 21 of *Advances in Quantum Chemistry*. Academic Press, 1990.

[27] E .K. U. Gross, J. F. Dobson, and M. Petersilka. *Topics in Current Chemistry*, volume 181. Springer Verlag, 1996.

[28] G. Onida, L. Reining, and A. Rubio. Electronic excitations: density-functional versus many-body green's-function approaches. *Rev. Mod. Phys.*, 74:601–659, 2002.

[29] N. T. Maitra. *Reviews of Modern Quantum Chemistry*. WORLD SCIENTIFIC, 2002.

[30] M. Casida. *Recent Developments and Applications of Modern Density Functional Theory*, volume 41. Elsevier Science, 1996.

[31] J. C. Tully. Molecular dynamics with electronic transitions. *J. Chem. Phys.*, 93(2):1061–1071, 1990.

[32] M. Richter, P. Marquetand, J. González-Vázquez, I. Sola, and L. González. SHARC: ab initio molecular dynamics with surface hopping in the adiabatic representation including arbitrary couplings. *J. Chem. Theory Comput*, 7(5):1253–1258, 2011. PMID: 26610121.

[33] S. Mai, P. Marquetand, and L. González. A general method to describe intersystem crossing dynamics in trajectory surface hopping. *Int. J. Quantum Chem.*, 115, 2015.

[34] S. Mai, P. Marquetand, and L. González. Nonadiabatic dynamics: The SHARC approach. *Wiley Interdisciplinary Reviews: Computational Molecular Science*, 0(0):e1370.

[35] S. Mai, P. Marquetand, and L. González. Nonadiabatic dynamics: The SHARC approach. *WIRE Mol. Sci.*, 2018.

[36] L. Martínez-Fernández, J. González-Vázquez, L. González, and I. Corral. Time-resolved insight into the photosensitized generation of singlet oxygen in endoperoxides. *J. Chem. Theory Comput.*, 11(2):406–414, 2015. PMID: 25688180.

[37] A. J. Atkins and L. González. Trajectory surface-hopping dynamics including intersystem crossing in $[Ru(bpy)_3]^{2+}$. *J. Phys. Chem. Lett.*, 8(16):3840–3845, 2017. PMID: 28766339.

[38] C. Rauer, J. J. Nogueira, P. Marquetand, and L. González. Cyclobutane thymine photodimerization mechanism revealed by nonadiabatic molecular dynamics. *J. Phys. Chem. Lett.*, 138(49):15911–15916, 2016. PMID: 27682199.

[39] S. Mai, P. Marquetand, and L. González. Intersystem crossing pathways in the noncanonical nucleobase 2-thiouracil: A time-dependent picture. *J. Phys. Chem. Lett.*, 7(11):1978–1983, 2016. PMID: 27167106.

[40] B. Darren, A. D. Horke, A. D. Smith, H. M. Watts, E. Jager, E. Springate, O. Alexander, C. Cacho, R. T. Chapman, A. Kirrander, and R. S. Minns. Ab-initio surface hopping and multiphoton ionisation study of the photodissociation dynamics of cs2. *Chem. Phys. Lett.*, 683:383 – 388, 2017. Ahmed Zewail (1946-2016) Commemoration Issue of Chemical Physics Letters.

[41] F. M. Siouri, S. Boldissar, J. A. Berenbeim, and M. S. de Vries. Excited state dynamics of 6-thioguanine. *J. Physical Chem. A*, 121(28):5257–5266, 2017. PMID: 28651430.

[42] F. Peccati, S. Mai, and L. González. Insights into the deactivation of 5-bromouracil after ultraviolet excitation. *Philos. Trans. Royal Soc. A*, 375(2092), 2017.

[43] G. Granucci, M. Persico, and A. Toniolo. Direct semiclassical simulation of photochemical processes with semiempirical wave functions. *J. Chem. Phys.*, 114(24):10608–10615, 2001.

[44] F. Plasser, G. Granucci, J. Pittner, M. Barbatti, M. Persico, and H. Lischka. Surface hopping dynamics using a locally diabatic formalism: Charge transfer in the ethylene dimer cation and excited state dynamics in the 2-pyridone dimer. *J. Chem. Phys.*, 137(22):22A514, 2012.

[45] G. te Velde, F. M. Bickelhaupt, E. J. Baerends, C. Fonseca Guerra, S. J. A. van Gisbergen, J. G. Snijders, and T. Ziegler. Chemistry with adf. *J. Comput. Chem.*, 22(9):931–967, 2001.

[46] E. J. Baerends, T. Ziegler, A. J. Atkins, J. Autschbach, D. Bashford, O. Baseggio, A. Bérces, F. Matthias Bickelhaupt, C. Bo, P. M. Boerritger, Luigi Cavallo, C. Daul, D. P. Chong, D. V. Chulhai, L. Deng, R. M. Dickson, J. M. Dieterich, D. E. Ellis, M. van Faassen, A. Ghysels, A. Giammona, Stan J. A. van Gisbergen, A. Goez, A. W. Götz, S. Gusarov, F. E. Harris, P. van den Hoek, Z. Hu, Christoph R. Jacob, H. Jacobsen, L. Jensen, L. Joubert, J. W. Kaminski, G. van Kessel, C. König, F. Kootstra, A. Kovalenko, Mykhaylo Krykunov, Erik van Lenthe, D. A. McCormack, A. Michalak, M. Mitoraj, S. M. Morton, Johannes Neugebauer, V. P. Nicu, Louis Noodleman, V. P. Osinga, S. Patchkovskii, Michele Pavanello, C. A. Peeples, Pierre Herman Theodoor Philipsen, D. Post, Cory C. Pye, H. Ramanantoanina, P. Ramos, W. Ravenek, J. I. Rodríguez, P. Ros, R. Rüger, P. R. T. Schipper, D. Schlüns, H. van Schoot, G. Schreckenbach, J. S. Seldenthuis, Mike Seth, Jaap G. Snijders, Miquel Solà, Stener M., M. Swart, D. Swerhone, G. te Velde, V. Tognetti, P. Vernooijs, L. Versluis, Lucas Visscher, O. Visser, Fan Wang, T. A. Wesolowski, E. M. van Wezenbeek, G. Wiesenekker, S. K. Wolff, T. K. Woo, and A. L. Yakovlev. ADF2017, SCM, Theoretical Chemistry, Vrije Universiteit, Amsterdam, The Netherlands, https://www.scm.com.

Chapter 3

Linkage Isomerization of the trans-$[RuCl(NO)(Py)_4]^{2+}$ Complex

In this chapter the N→O linkage photoisomerization mechanism of the ruthenium nitrosyl complex $[RuCl(NO)(Py)_4]^{2+}$, for which a quasicomplete photoconversion between the stable nitrosyl (N-bonded) and metastable isonitrosyl (O-bonded) isomers has been observed under continuous irradiation of the crystal at 473 nm, is investigated using multiconfigurational second-order perturbation theory (CASPT2). The results support efficient intersystem crossing pathways from the initially excited singlet states to the lowest triplet excited state of metal-to-ligand charge transfer character (^{3}MLCT). The topology of the involved potential energy surfaces corroborates a complex sequential two-photon photoisomerization mechanism involving nonadiabatic processes in agreement with experimental observations and previous density functional theory calculations.

3.1 Previous Studies on the trans-$[RuCl(NO)(Py)_4]^{2+}$

The design of original photochromic compounds has been the center of intense research in photochemistry in order to build innovative functional materials for information processing and storage,[1–5] photocontrol in biological systems,[6;7] and photomechanical actuators.[8;9] The vast majority of reported photochromic compounds rely on organic molecules often undergoing photoinduced electrocyclic reactions.[1–3;10–12] However, transition metal complexes have also been designed to display photochromic properties. These systems are based on linkage isomerizations between the metal center and ambidentate ligands.[13–18] Among these systems, ruthenium nitrosyl complexes have attracted growing interest over the past two decades, not only owing to their photochromic properties but also because of their capability to photorelease nitric oxide.[19–42] Despite extensive experimental investigations, the mechanism for these two competing processes remained unclear

until recently.[43] Computational studies investigating the linkage photoisomerization

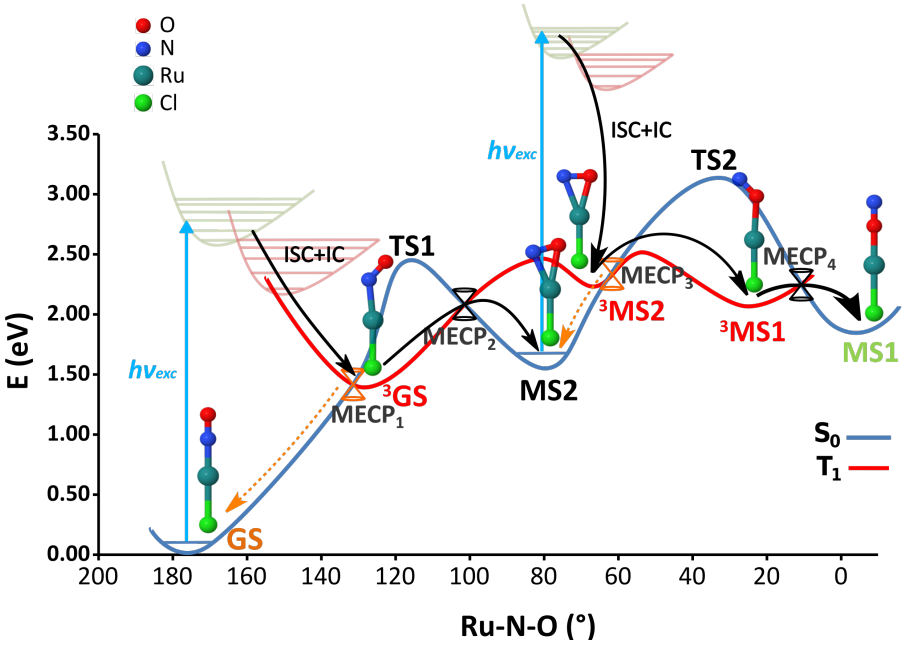

Figure 3.1 Potential energy profiles for the singlet ground state (blue curve) and the lowest triplet state (red curve) along the N→O linkage photoisomerization pathway derived from DFT calculations in Ref.[44]. The reaction coordinate is represented as the Ru-N-O angle. **GS**, **MS2** and **MS1** correspond to the N-bonded, NO-bonded and O-bonded isomers in the singlet state, respectively. ^{3}**GS**, ^{3}**MS2** and ^{3}**MS1** correspond to the N-bonded, NO-bonded and O-bonded isomers in the triplet state, respectively. Pyridine ligands have been omitted for clarity. Double-cone pictograms represent the minimum energy crossing points between the singlet and triplet states (in black the two ones relevant to N→O linkage photoisomerization). The black arrows indicate the sequential steps of the N→O linkage photoisomerization mechanism. The orange dashed arrows and orange double cones represent photostabilizing non-radiative decay paths to **GS** and **MS2**. Reprinted with permission from *J. Chem. Theory Comput.* 2017, 13, 12, 6120-6130. Copyright 2017, American Chemical Society.

mechanisms of metal complexes remain relatively scarce owing to the difficulty to compute the excited-state potential energy landscape in such systems.[45] The most significant contributions are based on DFT calculations of the S→O linkage photoisomerization pathways in ruthenium and osmium sulfoxide complexes[46–50] and of the P→O linkage photoisomerization pathway in a phosphinidene oxide ruthenium complex.[18] Very recently, the N→O linkage photoisomerization pathway in the trans-[RuCl(NO)(Py)$_4$]$^{2+}$ruthenium nitrosyl complex was investigated using a similar DFT-based strategy.[44] This study shed some light on the mechanistic picture of the N→O linkage photoisomerization. In contrast to ruthenium sulfoxide and phosphinidene oxide complexes for which energetically favorable linkage photoisomerization pathways on the lowest triplet excited state were characterized,[18;47;48] the triplet excited-state pathway for the N→O linkage

photoisomerization reveals an activated and energetically uphill process.[44] On account of these results, a complex sequential two-photon photoisomerization mechanism involving nonadiabatic processes was proposed[44] and later confirmed experimentally.[41] As illustrated in 3.1, the most stable N-bonded ground-state isomer (denoted **GS**) absorbs a blue light photon, which brings the system in excited singlet metal-to-ligand charge transfer (^{1}MLCT) states. These states are assumed to quickly relax by ISC due to significant SOC and by IC to the lowest triplet MLCT excited state (^{3}MLCT) leading to the N-bonded triplet state ^{3}**GS**. The system then encounters a large barrier (ca. 1 eV) on the adiabatic triplet PES to reach the NO-bonded ^{3}**MS2** intermediate. A more accessible route is provided by ISC at a triplet/singlet crossing point allowing the system to decay at the **MS2** singlet state. A key feature of this mechanism is that this metastable state can also absorb the same blue light photon as **GS**, as revealed by the computed electronic absorption spectra with TD-DFT.[44] The system can then be re-excited to ^{1}MLCT states from which nonradiative decays by ISC and IC lead to the population of ^{3}**MS2**. From this intermediate, a small adiabatic barrier needs to be overcome to reach the O-bonded ^{3}**MS1**. Another singlet/triplet crossing lying nearby allows for ISC to the O-bonded **MS1** product. This final photoproduct does not absorb in the blue light spectral range. Thus, this proposed mechanistic picture accounts for the change of color of a single crystal of trans-$[RuCl(NO)(Py)_4]^{2+}(PF_6)_2\cdot 1/2H_2O$ from orange (**GS**) to green (**MS1**) with a very high photoconversion yield observed upon irradiation in the 473-476 nm region.[35;36;38] This sequential two-photon absorption mechanism was recently confirmed by visible absorption spectroscopy.[41]

However, this DFT-based study relies on the assumption that the photochemical properties of the studied complex can be rationalized based on the population of the lowest triplet excited state. While it is reasonable to think that the lowest excited state will eventually be populated, relaxation pathways from the initially excited singlet states and their possible deactivation to higher triplet states by ISC have not been considered thoroughly. In other words, the initial part of the photochemical path has largely been overlooked and assumed to lead to the lowest excited state on an ultrafast timescale. The ground for such an assumption relies on previous reports of efficient ISC[51;52], short singlet excited-state lifetimes[53–56], and significant spin-orbit couplings[57–59] in polypyridine ruthenium complexes, and SOC dynamics simulations in a ruthenium nitrosyl complex showing highly efficient ultrafast decay to the lowest triplet state[60]. In addition, this study relied on single-reference DFT to compute complex excited-state energy landscape including regions of bond breaking and bond formation where multiconfigurational character in the electronic state wavefunction is expected[61]. Thus, it is important to benchmark DFT results against more reliable multiconfigurational wavefunction-based methods[62].

The purpose of the present chapter is to investigate with an accurate ab initio method the photoisomerization pathways for the trans-$[RuCl(NO)(Py)_4]^{2+}$complex based on a static picture provided by the computation of the potential energy landscapes of relevant electronic states along the reaction paths. To achieve this goal, multiconfigurational calculations based on CASSCF and MS-CASPT2 methods including SOC have been

performed to study the initial ISC pathways and to revisit the photo-isomerization mechanism, in comparison to the previous DFT and TD-DFT results.

3.2 Computational Details

Multiconfigurational ab initio calculations were performed using the CASSCF and MS-CASPT2 methods[63]. These calculations have three main objectives: (i) determine the electronic structures and vertical transition energies associated with the low-lying excited states of the three isomers **GS**, **MS2** and **MS1**, (ii) investigate the main ISC pathways after initial irradiation of **GS**, and (iii) determine the potential energy landscape along the photoisomerization reaction paths. All reference CASSCF calculations were performed distributing 16 electrons in 13 molecular orbitals. This active space, shown in Figure 3.2 for the **GS** isomer, was chosen in view of the photoisomerization process, which mainly involves the three atoms Ru, N, and O, with a Ru-N bond breaking and a Ru-O bond formation. Accordingly, the five Ru(4d) valence orbitals need to be included, together with the orbitals directly interacting with them, in particular along the Ru-N-O axis. he active orbitals thus include the five 4d valence orbitals, the two pairs of π and π^* and the pair of σ and σ^* orbitals on NO, and one combination of N(p) orbitals of the equatorial pyridine ligands (σ_{Py}). State-averaged calculations over seven states were performed separately for singlet and triplet states (denoted SA7-CASSCF(16,13)). This number of states is necessary to stabilize the active space. MS-CASPT2 calculations were then performed using a standard IPEA shift[64;65] of 0.25 a.u. and a level shift of 0.3 a.u. was carefully chosen in order to avoid intruder states. For the first objective, the mixing was allowed between all seven singlet states (denoted MS7-CASPT2). Regarding the second and third objectives, the four lowest states were allowed to mix (denoted MS4-CASPT2), as only four triplet states are energetically accessible at the irradiation wavelength. In all calculations the Douglas-Kroll-Hell Hamiltonian and the Cholesky decomposition with a threshold of 10^{-4} a.u. were used along with the ANO-RCC-VTZP all-electron basis for Ru and ANO-RCC-VDZP for the other atoms. Oscillator strengths were computed using perturbation modified CASSCF (PM-CASSCF)[63] transition dipole moments along with MS-CASPT2 transition energies. All the MS-CASPT2 calculations were performed with MOLCAS 8.0.[66]

Additional calculations using the strongly-contracted second-order n-electron valence state perturbation theory (SC-NEVPT2) method[67] were performed to give further support to the MS-CASPT2 results. This method has the nice feature that it does not suffer from intruder state problems and the second-order perturbation energy is completely defined once the zeroth-order reference wavefunction is chosen. We have performed SC-NEVPT2 calculations to calculate the $S_0 \rightarrow S_1$ vertical transition at **GS** and **MS1** using the same active space as for the MS-CASPT2 calculations but state-averaging over three states only (as S_1 and S_2 are degenerate at these geometries). The def2-TZVP basis[68] on all atoms was used along with the associated small core relativistic pseudopotential[69] for the Ru

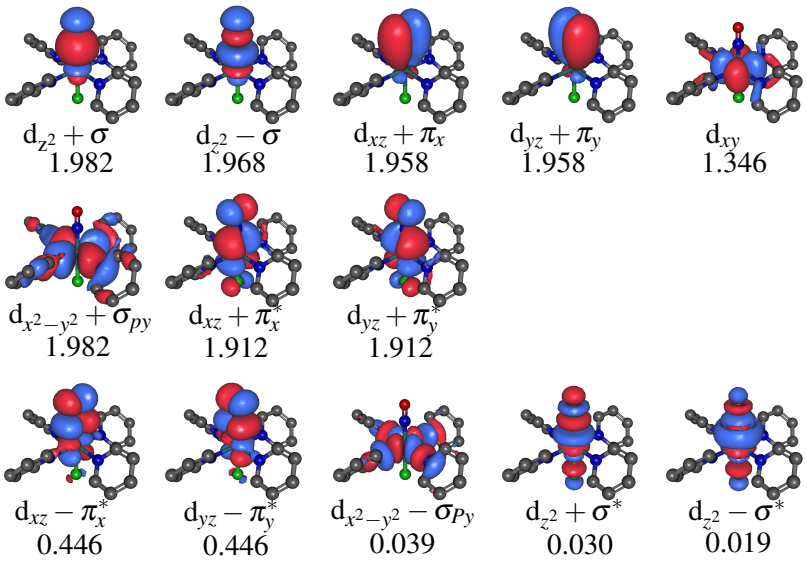

Figure 3.2 Active orbitals and average occupation numbers over the 7 states obtained from the SA7-CASSCF(16,13)/ANO-RCC-VTZP calculation at the **GS** isomer. Reprinted with permission from *J. Chem. Theory Comput.* 2017, 13, 12, 6120-6130. Copyright 2017, American Chemical Society.

atom. Because the singlet-triplet energy gap is an important feature of the PES due to the involved triplet/singlet crossings along the photoisomerization pathway, the adiabatic **GS**$\rightarrow^3$**GS** energy difference was also computed with SC-NEVPT2/def2-TZVP using SA7-CASSCF(16,13) wavefunctions. Domain based local pair natural orbital coupled cluster with single, double and perturbative triple excitations, DLPNO-CCSD(T),[70] using the def2-TZVP basis set were performed to investigate the thermal isomerization pathway and the adiabatic **GS**$\rightarrow^3$**GS** energy difference. SC-NEVPT2 and DLPNO-CCSD(T) calculations were performed with ORCA 4.0.0[71]

Regarding the computation of the ISC pathways, the relaxation path on S_1 was constructed as a linearly interpolated transit path (LITP) in internal coordinates between the **GS** isomer equilibrium structure and the optimized geometry of the S_1 excited state corresponding to the N-bonded isomer, denoted ^{1}**GS***. The **GS** structure was taken from a previous DFT study (using B3LYP with Grimme's dispersion correction; denoted B3LYP+D3 in the following),[44] while that of ^{1}**GS*** was obtained from a TD-B3LYP geometry optimization (see Table A.1 in Supporting Information). Along this path, MS4-CASPT2 single-point energy calculations were performed for the lowest four singlet and triplet states as shown in Table A.2 in Supporting Information). SOC calculations were performed at selected geometries along the S_1 relaxation path within the spin-orbit state interaction frame,[72] using singlet and triplet spin-free CASSCF wavefunctions as basis for the spin-orbit Hamiltonian. Dynamic electron correlation effects were included by using the MS-CASPT2 energies as the diagonal elements of the spin-orbit Hamiltonian.

The thermal isomerization pathway was constructed as a LITP between the various optimized stationary points on the lowest singlet PES (i.e., the **GS**, **MS2** and **MS1** minima and the transition states **TS1** and **TS2** connecting them). These optimized geometries were retrieved from a previous DFT study.[44] We have tested the effect of using CASSCF optimized structures. However, due to lack of dynamic correlation at the CASSCF level, the DFT structures proved to be more accurate (see Table 3.1 and Figure 3.3). Similarly,

Structure	B3LYP+D3	CASSCF	X-Ray data
Ru-N	1.745	1.763	1.755
Ru-O	2.886	2.905	
N-O	1.141	1.143	1.146
Ru-Cl	2.317	2.377	2.321
Ru-N_{Py1}	2.139	2.166	2.107[a]
Ru-N_{Py2}	2.139	2.166	2.107[a]
Ru-N_{Py3}	2.139	2.166	2.107[a]
Ru-N_{Py4}	2.139	2.166	2.107[a]
$\angle$ Ru-N-O	180.0	180.0	178.3

Table 3.1 Selected structural parameters for the optimized geometry of **GS** at B3LYP+D3 and CASSCF levels. Bond lengths in and angles in degrees. X-Ray data is taken from Cormary et al., Acta Cryst. B **2009**, 65, 612-623. [a]Mean value for the different Ru-N_{Py} bond lengths. Reprinted with permission from *J. Chem. Theory Comput*. 2017, 13, 12, 6120-6130. Copyright 2017, American Chemical Society.

the photoisomerization pathway was obtained from a LITP between the ^{3}**GS**, ^{3}**TS1**, ^{3}**MS2**, ^{3}**TS1** and ^{3}**MS1** optimized DFT structures. All the MS-CASPT2 energies along these interpolated paths are given in Tables 3.3 and Table A.3 in Supporting Information. Note that there is a minor change occurring in the active space along these LITP paths. The $d_{x^2-y^2} + \sigma_{Py}$ and $d_{x^2-y^2} - \sigma_{Py}$ are both replaced by orbitals with similar occupation numbers as shown in Figure 3.4. The main reason is that the original orbitals contribute to a singlet and a triplet excited state in the FC region (S_3 and T_4 in Table 3.2) but these states become too high in energy along the LITP and are then not included anymore in the state-average procedure, thus making these orbitals less relevant. However, this change of active space does not alter the CASSCF and MS-CASPT2 energies significantly (within 0.1 eV). At **MS1**, it is possible to find two stable solutions of the active space that differ mainly in the contribution of the Cl atom (see Figure 3.1). Both active spaces lead to very similar potential energy landscapes along the linkage isomerization pathway (Figure A2 in Supporting Information).

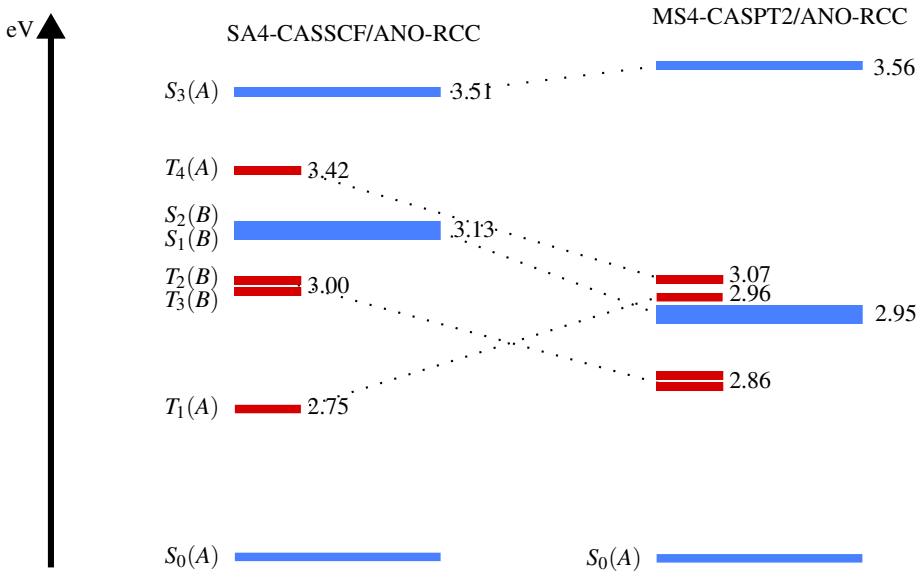

Figure 3.3 MS-CASPT2 singlet and triplet energies at DFT (B3LYP+D3) and CASSCF optimized geometries of **GS**. Reprinted with permission from *J. Chem. Theory Comput.* 2017, 13, 12, 6120-6130. Copyright 2017, American Chemical Society.

3.3 Electronic structures and absorption properties

3.3.1 Electronic Structure

The first seven singlet and triplet electronic states were computed at the **GS** DFT-optimized geometry using the MS7-CASPT2/ANO-RCC level of theory. Table 3.2 provides the vertical transition energies and details about the electronic structures of each electronic state, along with oscillator strengths. In all cases, the weights of the leading configuration of the CASSCF wavefunctions, C^2, are less than 0.9, indicating a significant multireference character[73] for some the states computed, including S_0 for which the weight of the leading closed-shell configuration is 0.71.

The first two singlet excited states S_1 and S_2 are degenerate by symmetry (^{1}E) and predicted at 3.03 eV (409 nm) and 2.93 eV (423 nm) at the MS-CASPT2 and SC-NEVPT2 levels, respectively. Based on the oscillator strengths computed at the MS-CASPT2 level, these two states are the only "bright" states at this geometry among the states computed, although the oscillator strength is very weak (0.0002). This pair of states are obtained by a MLCT transition involving the ruthenium d_{xy} orbital and a degenerate pair of orbitals mixing Ru(d_{xz}) and NO(π_x^*), and Ru(d_{yz}) and NO(π_y^*), respectively. This specific transition is notably well documented in the literature.[35;44;60] The character of the CASSCF transition is in agreement with that of earlier TD-DFT calculations at the same geometry[44] and confirms the assignment deduced from the experimental data[35]. However, a higher oscillator strength (0.003) and a lower transition energy (2.86 eV) are obtained at the TD-DFT level

state	CASSCF ΔE	MS-CASPT2 ΔE	main transition	nature	C^2	f
			Singlets			
S_0	0.000	0.000			0.71	
S_1	3.076	3.028	$d_{xy} \rightarrow d_{xz} - \pi_x^*$	MLCT	0.84	0.0002
S_2	3.076	3.028	$d_{xy} \rightarrow d_{yz} - \pi_y^*$	MLCT	0.84	0.0002
S_3	3.504	3.662	$d_{xy} \rightarrow d_{x^2-y^2} - \sigma_{Py}$	MC	0.61	0.0000
S_4	3.972	3.785	$d_{xz} + \pi_x^* \rightarrow d_{xz} - \pi_x^*$	MLCT	0.43	0.0000
			$d_{yz} + \pi_y^* \rightarrow d_{yz} - \pi_y^*$		0.43	
S_5	3.984	3.785	$d_{yz} + \pi_y^* \rightarrow d_{yz} - \pi_y^*$	MLCT	0.49	0.0000
			$d_{xz} + \pi_x^* \rightarrow d_{xz} - \pi_x^*$		0.38	
S_6	3.988	3.956	$d_{yz} + \pi_y^* \rightarrow d_{yz} - \pi_y^*$	MLCT	0.42	0.0000
			$d_{xz} + \pi_x^* \rightarrow d_{xz} - \pi_x^*$		0.32	
			Triplets			
T_1	2.973	2.924	$d_{xy} \rightarrow d_{xz} - \pi_x^*$	MLCT	0.87	0.0000
T_2	2.973	2.925	$d_{xy} \rightarrow d_{yz} - \pi_y^*$	MLCT	0.87	0.0000
T_3	3.301	3.086	$d_{xz} + \pi_x^* \rightarrow d_{xz} - \pi_x^*$	MLCT	0.44	0.0000
			$d_{yz} + \pi_y^* \rightarrow d_{yz} - \pi_y^*$		0.44	
T_4	2.721	3.106	$d_{xy} \rightarrow d_{x^2-y^2} - \sigma_{Py}$	MC	0.67	0.0000
T_5	3.647	3.548	$d_{xz} + \pi_x^* \rightarrow d_{xz} - \pi_x^*$	MLCT	0.44	0.0000
			$d_{yz} + \pi_y^* \rightarrow d_{yz} - \pi_y^*$		0.44	
T_6	3.649	3.555	$d_{xz} + \pi_x^* \rightarrow d_{xz} - \pi_x^*$	MLCT	0.44	0.0000
			$d_{yz} + \pi_y^* \rightarrow d_{yz} - \pi_y^*$		0.44	
T_7	3.918	3.854	$d_{xz} + \pi_x^* \rightarrow d_{xz} - \pi_x^*$	MLCT	0.44	0.0000
			$d_{yz} + \pi_y^* \rightarrow d_{yz} - \pi_y^*$		0.44	

Table 3.2 SA7-CASSCF and MS7-CASPT2 transition energies, ΔE (eV), nature of the main transitions with their respective weights, and oscillator strengths computed at the **GS** optimized geometry. C^2 is the weight of the leading configuration in the SA7-CASSCF wavefunctions. f is the oscillator strength computed using PM-CASSCF transition dipole moments and MS-CASPT2 energies of the spin-free states.

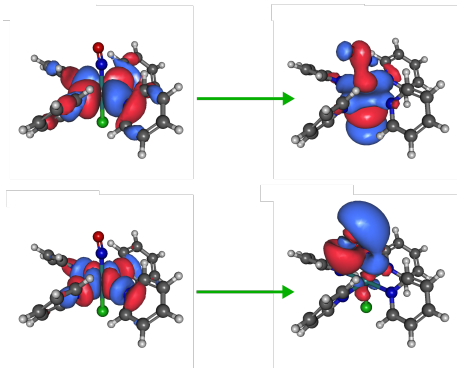

Figure 3.4 Change of active space along the linearly interpolated transit path (LITP) for the thermal isomerization. Reprinted with permission from *J. Chem. Theory Comput*. 2017, 13, 12, 6120-6130. Copyright 2017, American Chemical Society.

in acetonitrile.[44] Note that the irradiation wavelength used experimentally (473-476 nm) is tuned to optimize the photoconversion efficiency and thus does not correspond necessarily to the maximum of the $S_0 \rightarrow S_1/S_2$ absorption band of the crystal.[35;36;38] In addition, the experimental absorption spectrum recorded in acetonitrile gives this transition at 2.76 eV (450 nm),[74] in reasonable agreement with our MS-CASPT2 calculations in gas phase. The higher singlet states found are well separated from S_1/S_2, with S_3 up to S_6 lying between 0.6 to 0.9 eV above S_1/S_2. However, it is interesting that S_3, a metal-centered (MC) state found at 3.7 eV vertically above the ground state at the MS-CASPT2 level, was found at 4 eV at the TD-DFT level and corresponded to S_{20} due to many MLCT states being lower in energy.[44] This is due to the fact that some electronic excited states are missing here due to the limited size of the active space. For example, TD-DFT predicts vertical transition energies to S_6 and S_7 corresponding to excitation from a pyridine π orbital to $Ru(d_{xz})/NO(\pi_x^*)$ orbitals. As pyridine π orbitals have not been included in the active space, these states are not described. However, we describe all the lowest excited states relevant to the photoisomerization mechanism (vide infra).

Regarding the triplet states, T_1 and T_2 are degenerate by symmetry (^{3}E) and are located only 0.1 eV below S_1/S_2. These two states are described by transitions involving the same orbitals as in S_1/S_2 (^{1}E), thus displaying the same MLCT character. The next two triplets T_3 and T_4 are less than 0.2 eV above T_1/T_2 and less than 0.1 eV above S_1/S_2. Note that T_4 is a ^{3}MC state. The following triplet states are found substantially higher in energy. Thus, mainly the four lowest triplet states are possibly interacting with the initially excited S_1/S_2 states, as the proximity of these states could indeed create appropriate conditions for efficient singlet to triplet intersystem crossings just after light absorption by **GS**. This hypothesis, already suggested in the preceding DFT studies,[44;60] will be developed and discussed in the next subsection. Interestingly, the singlet transition energies at the CASSCF level are in good agreement (within 0.2 eV) with the MS-CASPT2 ones; however the order of the states is not correctly reproduced for triplet states.

structure	state	MS-CASPT2 ΔE	wavelength	main transition	f
GS	S_1	3.028 (3.101)	409 (400)	$d_{xy} \rightarrow d_{xz} - \pi_x^*$	0.0002 (0.0002)
	S_2	3.028 (3.101)	409 (400)	$d_{xy} \rightarrow d_{yz} - \pi_y^*$	0.0002 (0.0002)
MS2	S_1	2.054 (2.095)	604 (592)	$d_{yz} + \pi_y^* \rightarrow d_{xz} - \pi_x^*$	0.0015 (0.0008)
	S_2	2.363 (2.263)	525 (548)	$d_{yz} + \pi_y^* \rightarrow d_{yz} - \pi_y^*$	0.0001 (0.0002)
	S_3	2.634 (2.648)	471 (468)	$d_{xy} \rightarrow d_{yz} - \pi_y^*$	0.0077 (0.0075)
	S_4	3.035 (2.874)	409 (431)	$d_{xy} \rightarrow d_{xz} - \pi_x^*$	0.0004 (0.0005)
	S_5	3.171 (3.193)	391 (388)	$d_{xz} + \pi_x^* \rightarrow d_{yz} - \pi_x^*$	0.0005 (0.0003)
MS1	S_1	1.933 (1.944)	641 (638)	$d_{xy} \rightarrow d_{xz} - \pi_x^*$	0.0001 (0.0001)
	S_2	1.933 (1.944)	641 (638)	$d_{xy} \rightarrow d_{yz} - \pi_y^*$	0.0001 (0.0001)

Table 3.3 MS7-CASPT2 transition energies, ΔE (eV), corresponding wavelengths (nm), nature of the main transitions, and oscillator strengths computed for the three isomers **GS**, **MS2** and **MS1**. Results obtained in acetonitrile are given in parentheses. Oscillator strength computed using PM-CASSCF transition dipole moments and MS-CASPT2 energies of the spin-free states.

3.3.2 Absorption Properties

Vertical transition energies were also computed at the metastable **MS1** and **MS2** DFT-optimized geometries in order to describe the low-energy part of the absorption spectra of the three isomers. All the lowest singlet states carrying non-zero oscillator strengths are listed in Table 3.3 for all three isomers. The convoluted absorption spectra for the three isomers are shown in Figure 3.5.

As pointed out previously, the limited size of the reference active space prevents the description of all the optical transitions (e.g., those involving Cl(p) and Py(π) orbitals[44]). Nevertheless, all the relevant excited states for the photo-isomerization mechanism (which all involve Ru(d) or Ru(d) + NO(π^*) to Ru(d)-NO(π^*) transitions) are present. In addition, the MS-CASPT2 vertical transition energies agree qualitatively with those obtained by TD-DFT computed in acetonitrile:[44] i) the order of the states found at the MS-CASPT2 level is the same at the TD-DFT level; ii) the MS-CASPT2 transitions are systematically higher in energy than the TD-DFT ones (within 0.3 eV) for the bright states.

The **MS2** isomer displays three absorption bands: a weak band centered around 600 nm, a more intense one around 470 nm and a weak absorption feature at 400 nm. The electronic transition carrying the low energy band corresponds to the S_1 state and involves a $d_{yz} + \pi_y^* \rightarrow d_{xz} - \pi_x^*$ excitation, which was not found among the lowest excited states computed at the **GS** geometry. The more intense absorption around 470 nm is associated with S_3 and is associated with a $d_{xy} \rightarrow d_{yz} - \pi_y^*$ transition, which correlates with one component of the doubly degenerate S_1/S_2 states at the **GS** structure. The higher energy absorption feature around 400 nm is assigned to both S_4 and S_5, which exhibit transition

wavelength at 409 and 391 nm, respectively. As discussed later, this band plays a critical role in the N→O linkage photoisomerization mechanism, as it is superimposed with the absorption band of the **GS** isomer at 409 nm (Figure 3.5). This is in good agreement with the TD-DFT results[44] obtained in acetonitrile, which also predicted an overlap of the absorption bands between **GS** and **MS2** in this region.

The **MS1** isomer shows a weak band around 640 nm. The corresponding transition is

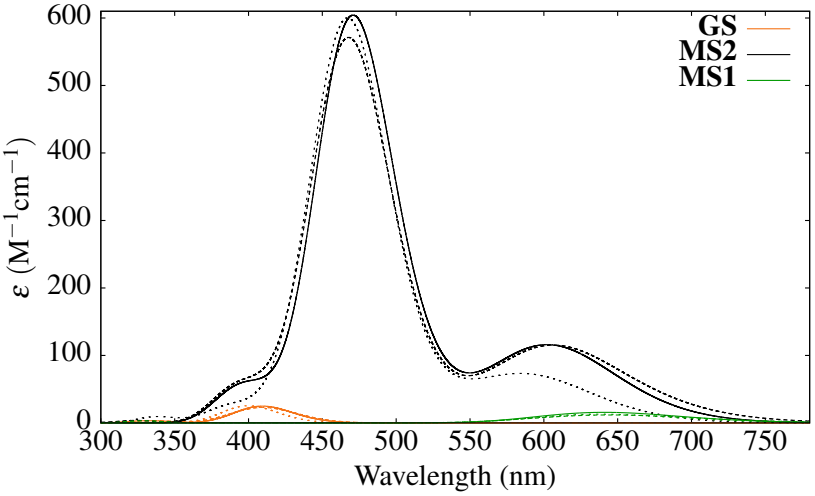

Figure 3.5 MS7-CASPT2 absorption spectra for the **GS**, **MS2**, and **MS1** isomers in the gas phase (convoluted arbitrarily with a Gaussian function characterized by a standard deviation of 6000 cm^{-1}). Full lines spin-free calculations; dashed lines including spin-orbit couplings; dotted lines spin-free calculations in acetonitrile. Reprinted with permission from *J. Chem. Theory Comput.* 2017, 13, 12, 6120-6130. Copyright 2017, American Chemical Society.

of MLCT character and is assigned to a pair of degenerate S_1/S_2 states involving similar electronic transitions as the S_1/S_2 states of the **GS** isomer. The MS-CASPT2 transition energy of 1.933 eV is about 0.2 eV higher than the SC-NEVPT2 value at 1.719 eV (721 nm). This is also in reasonable agreement with the TD-DFT results[44] in acetonitrile, which give the same transition at 703 nm, and the irradiation wavelength at 782 nm used experimentally.[41] This band overlaps with the low-energy absorption band of the **MS2** isomer, which is important for the reverse O→N linkage photoisomerization mechanism.[44] It is also important to note that **MS1** and **GS** absorb at very different wavelengths, which is an essential requirement for having an efficient photochromic switch.

Regarding the band intensities in Figure 3.5, it appears that they are underestimated by one order of magnitude for **GS** and **MS1** compared to TD-DFT and experimental observations in acetonitrile. This is due to the too weak transition dipole moments computed at the PM-CASSCF level. In addition, **MS2** displays more intense absorption bands relative to **GS** and **MS1** at the MS-CASPT2 level, a result that was neither observed at the TD-DFT level,[44] nor experimentally.[35] Including the SOC in the calculations did not alter significantly these absorption spectra, as shown in Figure 3. We tentatively attribute this

inconsistency either to inaccurate CASSCF transition dipole moments resulting from a lack of dynamic electron correlation in the CASSCF wavefunctions, or to the incomplete set of active orbitals used.

3.4 Intersystem Crossing Pathway

Investigation of singlet to triplet radiationless transitions is of utmost importance in the trans-[RuCl(NO)(Py)$_4$]$^{2+}$photochemistry, as a previous dynamical study on a related system highlighted the efficiency of these transitions[60] and the whole photoisomerization mechanism proposed in the previous DFT work[44] involves several singlet/triplet crossings (Figure 3.1) and assumed that ultrafast and efficient ISC was taking place from the initially excited ^{1}MLCT states to the lowest ^{3}MLCT state. A quantitative study of these nonradiative deactivation processes would require taking into account all the spin-vibronic couplings within a time-dependent approach.[45;75–77] Here, we simply investigate what are the lowest triplet states of interest susceptible to be populated by ISC using a static picture provided by MS4-CASPT2 and SOC calculations along the initial S_1 relaxation pathway.
The MS4-CASPT2 energies are plotted in Figure 3.6 along this S_1 relaxation pathway (data supplied in Table A.2 in Supporting Information) and SOC are provided between states lying close to each other. As expected, the lowest excited states S_1 and S_2 lose their degeneracy as the molecule leaves the Frank-Condon region. The S_1 state evolves toward its minimum (^{1}**GS***) along a barrierless potential energy profile, while S_2 eventually rises in energy. According to these MS-CASPT2 calculations, the four lowest triplet states are very close in energy to the lowest singlet excited states S_1 and S_2, especially in the vicinity of the Frank-Condon region where they cross each other several times. T_3 is almost degenerate (0.06 eV gap) with S_1/S_2 at the FC geometry. A S_1/T_2 crossing is encountered close to the FC geometry (between 0.2 and 0.3 along the LITP) and a S_2/T_3 crossing is present further along the S_1 relaxation coordinate (between 0.4 and 0.5 along the LITP). Furthermore, the lowest triplet state T_1 continuously lies below the S_1 state. Note that the T_1, T_2 and T_4 MS-CASPT2 energies are inaccurate at 0.1 along the LITP because of an artificially too strong mixing in the multistate calculation. This is a well-known MS-CASPT2 issue that can occur near avoided crossings and conical intersections.[78]
To get more insight into the possible ISC pathways, SOC calculations were performed at various geometries along the S_1 relaxation coordinate. The SOC values are shown in inset of Figure 3.6 between the S_1 state and the nearest triplet state from the initial **GS** structure to 0.3 along the LITP. Near the Frank-Condon geometry, the S_1 state strongly couples with T_3 (SOC 240 cm^{-1} at **GS** and at 0.1 along the LITP) resulting in a probable $S_1 \rightarrow T_3$ ISC. Between 0.2 and 0.3 along the LITP, S_1 crosses with T_2 with a substantial SOC between these states (150 cm^{-1}). The smaller SOC compared to that between S_1 and T_3 is compatible with the El-Sayed rule,[79] in the sense that the S_1 and T_2 state share the same character in their electronic transitions (both states are d$\rightarrow$d - π^*). An $S_1 \rightarrow T_2$ ISC pathway is also very likely. Thus, S_1 will most likely deactivate non-radiatively to T_2

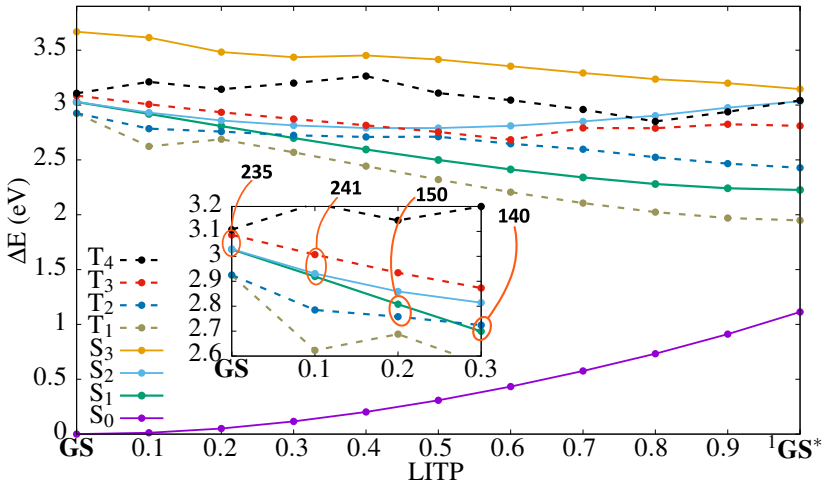

Figure 3.6 MS4-CASPT2 singlet an (full lines) and triplet (dashed lines) potential energy profiles along the S_1 relaxation pathway (linearly interpolated transit path: LITP) from the initial **GS** structure to the TD-DFT optimized S_1 minimum ^{1}**GS***. (inset) Spin-orbit couplings (cm^{-1}) between pairs of states. Reprinted with permission from *J. Chem. Theory Comput.* 2017, 13, 12, 6120-6130. Copyright 2017, American Chemical Society.

and T_3 in the initial relaxation dynamics after irradiation. Because T_3 also crosses with T_2 (Figure 3.6), it is likely that T_3 will undergo efficient internal conversion to T_2. Eventually, T_2 is expected to decay to T_1, the lowest-lying excited state, but depending on the rate and efficiency of this population transfer, the T_2 state (correlating with the T_3 FC state) may still be substantially populated. Thus, according to these calculations, the initial T_1, T_2 and T_3 MLCT states are all involved in the initial excited-state relaxation dynamics of trans-$[RuCl(NO)(Py)_4]^{2+}$.

It is also debatable whether part of the initial electronic population would remain on the initial S_1 and S_2 singlet excited states. Initially, these two states must be equally populated as they form a Jahn-Teller degeneracy. Because S_2 is quickly crossing T_3, its population is expected to decay rapidly toward this state (SOC of 186 cm^{-1} at 0.4 along LITP) and also to the lower S_1 state. Relaxation on S_1 leads the system to its lowest singlet excited-state N-bonded minimum, ^{1}**GS***. Again, depending on the rate and efficiency of the ISC channels described above (i.e., $S_1 \rightarrow T_3$ and $S_1 \rightarrow T_2$), part of the S_1 population may remain on this state and relax to ^{1}**GS***. The consequences of this scenario on the photoisomerization mechanism are described below. However, previous experimental[51–56;80–82] and theoretical[57–60;83] studies point out that ISC pathways are efficient in ruthenium polypyridine complexes. Thus, S_1 is expected to be depopulated rapidly. In particular, recent nonadiabatic molecular dynamics simulations carried out on a related ruthenium nitrosyl complex demonstrated how the large SOC (150 cm^{-1} or more) promotes very efficient ISC, with up to 85% of trajectories undergoing ultrafast ISC in the first 10 fs.[60] Our MS-CASPT2 calculations evidence large SOC and therefore efficient ISC

channels are expected.

3.5 Potential Energy Landscape

The previous DFT study focused on the lowest singlet and triplet PES for the whole photoreactive process.[44] Intervention of higher triplets T_2 and T_3 was mentioned then but remained hypothetic. The computational strategy involved characterization and optimization of the various minima, transition states and minimum energy crossing points along the photoisomerization pathway. The aim of the present MS-CASPT2 calculations is to reinvestigate the complete mechanism based on a multireference ab initio method capable of describing both static and dynamic electron correlation in a balanced way for all the electronic states involved.

3.5.1 Singlet States

Figure 3.8 presents the MS4-CASPT2 potential energy profiles for the four lowest singlet states along the ground-state (thermal) isomerization pathway (data provided in Table A.3 in Supporting Information). The ground state S_0 energy profile appears to be in very good agreement with the one obtained at the DFT level. Indeed, all the minima (**GS**, **MS2** and **MS1**) and transition states connecting them (**TS1** and **TS2**) are found at the MS4-CASPT2 level. Energy gaps are also well reproduced, with a maximum deviation of 0.3 eV at **TS2** and **MS1** geometries between DFT and MS4-CASPT2. Thus, the ab initio results are in line with the previous DFT calculations: the thermal N→O linkage isomerization cannot be achieved because of large thermodynamic barriers between **GS** and **MS1** on the ground-state PES.

The three lowest excited states S_1, S_2 and S_3 show a similar behavior in terms of potential energy profiles, which is in contrast to that of S_0: When S_0 is increasing in energy, S_1, S_2 and S_3 are decreasing, and vice versa. As a result, the energy gap between S_0 and these excited states is considerably reduced in the transition state regions at **TS1** and **TS2**, so much so that S_0 and S_1 become very close in energy. The shape of the potential energy curves suggests two avoided crossings near the two transition states. A detailed examination of the PM-CASSCF wavefunctions[63] (Figure A3 in Supporting Information) reveals that S_0 becomes heavily mixed around these transition states. Despite the high multiconfigurational character of the ground state in these regions, it is remarkable to note that a single determinant approach like DFT provides good transition state structures and accurate energy barriers. Another interesting feature of the PM-CASSCF wavefunctions is that, while S_0 is dominated by a single configuration at **GS** and **MS2**, it is strongly multiconfigurational at **MS1** with the largest weight in the configuration expansion being only 43% for the closed-shell ground-state determinant. In this case, the

multiconfigurational character is not due to electronic coupling with the lowest excited states found at the **MS1** geometry, as they are well separated in energy with S_0 (more than 2 eV higher), but results from mixing with excited states gained in the **TS2** region (Figure A3 in Supporting Information). Again, DFT describes the **MS1** structure and its relative energy accurately. Note that the reference SA7-CASSCF energy profiles are in good qualitative agreement with MS4-CASPT2 for these singlet states in Figure 3.7.

Coupled-cluster DLPNO-CCSD(T) calculations in Table A1 on the S_0 ground state

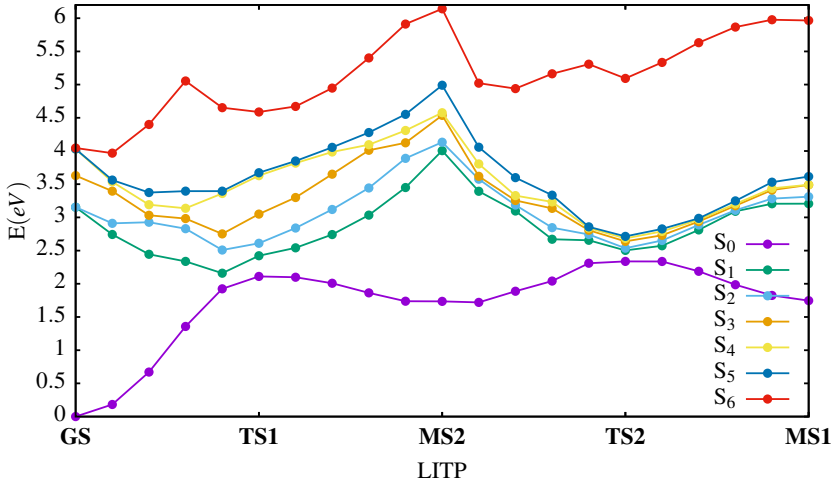

Figure 3.7 SA7-CASSCF(16,13) energy profiles of the seven lowest singlet states along the thermal isomerization pathway. Reprinted with permission from *J. Chem. Theory Comput.* 2017, 13, 12, 6120-6130. Copyright 2017, American Chemical Society.

confirmed the substantial multiconfigurational character encountered at **TS2** and **MS1**. Compared to the MS4-CASPT2 results, relative energy deviations of 0.1 eV up to 0.4 eV are obtained with DLPNO-CCSD(T). The T_1 diagnostic, which provides a useful indicator

Geometries	DPLNO-CCSD(T)	MS4-CASPT2	B3LYP+D3	T1 Diagnostic
GS	0.000	0.000	0.00	0.018
TS1	2.550	2.411	2.44	0.016
MS2	1.499	1.535	1.56	0.017
TS2	3.138	2.835	3.13	0.021
MS1	2.150	1.729	1.86	0.019

Table 3.4 DLPNO-CCSD(T) relative energies (eV) along the thermal isomerization pathway and comparison with MS-CASPT2 and DFT values.

for the importance of non-dynamical electron correlation effects,[84;85] shows the lowest values at **GS**, **TS1**, and **MS2** geometries, whereas a larger values of 0.021 and 0.019

are obtained at **TS2** and **MS1**, respectively. Thus, according to this diagnostic criterion, significant non-dynamical correlation effects are expected at these two geometries and single reference methods like CCSD(T) and DFT are potentially unreliable. This could explain why the discrepancies between these two levels of theory and MS4-CASPT2 are larger at **TS2** and **MS1**.

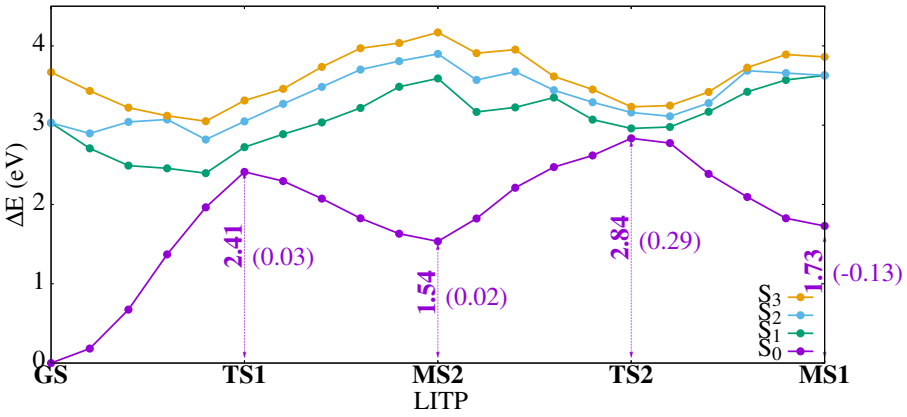

Figure 3.8 MS4-CASPT2 singlet potential energy profiles along the S_0 (thermal) linkage isomerization pathway (linearly interpolated transit path: LITP) between **GS**, **TS1**, **MS2**, **TS2**, and the **MS1** DFT-optimized structures. Relative energies are in electronvolts, and values in parentheses are the differences with the DFT values obtained in ref [44]. Reprinted with permission from *J. Chem. Theory Comput.* 2017, 13, 12, 6120-6130. Copyright 2017, American Chemical Society.

3.5.2 Triplet States

Figure 3.9 presents the MS4-CASPT2 potential energy profiles for the four lowest triplet states along the adiabatic T_1 photoisomerization pathway (data provided in Table A.4 in Supporting Information). The overall topology of the T_1 potential energy profile is again in good agreement with the DFT results. Three minima on the T_1 PES are located right at the ^{3}**GS**, ^{3}**MS2** and ^{3}**MS1** DFT structures and with the same energetic order: ^{3}**MS2** is the highest intermediate standing at ca. 0.9 eV above ^{3}**GS** and ca. 0.2 eV above ^{3}**MS1**. These relative energies are within 0.05 eV of the DFT values. Two maxima corresponding to the two transition states ^{3}**TS1** and ^{3}**TS2** are also present at the MS4-CASPT2 level, only slightly shifted with respect to the original position of the optimized transition states with DFT. The associated adiabatic T_1 potential energy barriers between ^{3}**GS** and ^{3}**MS2**, and between ^{3}**MS2** and ^{3}**MS1** are also in excellent agreement with the DFT values: the first barrier is very high at 1.12 eV (1.06 eV with DFT), while the second is much lower at 0.27 eV (0.26 eV with DFT). The next triplet states T_2, T_3, and T_4, have similar energy profiles to that of T_1 except in the region of ^{3}**MS2**, where their energy raises toward a maximum. Analysis of the PM-CASSCF wavefunctions (Figure A4 in Supporting Information) shows the multiconfigurational character of the triplet states in different

regions of the PES. In particular, T_1 becomes strongly multiconfigurational with the leading electronic configuration weighting less than 80% of the total wavefunction around ^{3}**GS**, ^{3}**TS1** and ^{3}**TS2**. Remarkably, the T_1 electronic structure changes from ^{3}**GS** to ^{3}**TS1** to ^{3}**MS2** due to various couplings with the higher triplet states. In particular, ^{3}**TS1** and ^{3}**TS2** correspond to regions of weakly avoided crossings between T_1 and higher triplet states. This is reminiscent to what was found between S_0 and higher singlet states at **TS1** and **TS2**. Note, however, that unlike singlet states, triplet states are in many occasions well represented by only one configuration with a weight greater than 80%. In addition, while the reference SA7-CASSCF energy profiles were in good qualitative agreement with MS4-CASPT2 for the lowest four singlet states, SA7-CASSCF gives a qualitatively wrong picture for the lowest triplet PES for which ^{3}**MS2** appears as a transition state rather than a minimum along the photoisomerization pathway (Figure A1 in Supporting Information).

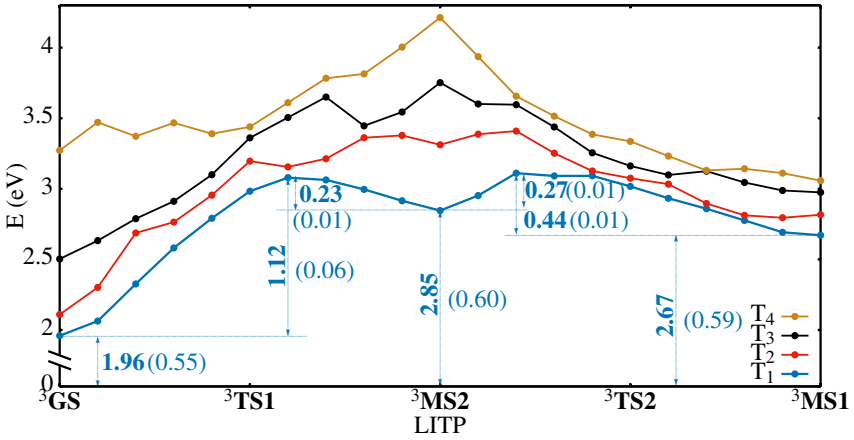

Figure 3.9 MS4-CASPT2 triplet potential energy profiles along the adiabatic T_1 linkage photoisomerization pathway (linearly interpolated transit path: LITP) between ^{3}**GS**, ^{3}**TS1**, ^{3}**MS2**, ^{3}**TS2**, and the ^{3}**MS1** DFT-optimized structures. Relative energies are in electronvolts, and values in parentheses are the differences with the DFT values obtained in ref [44]. Reprinted with permission from *J. Chem. Theory Comput.* 2017, 13, 12, 6120-6130. Copyright 2017, American Chemical Society.

3.5.3 Triplet/singlet crossings

Despite the excellent agreement between MS-CASPT2 and DFT regarding the adiabatic singlet and triplet potential energy profiles, there is one major discrepancy concerning the S_0-T_1 energy gap. At the MS-CASPT2 level, the T_1 PES is shifted up in energy by about 0.6 eV relative to the S_0 PES compared to DFT. As a result, the ^{3}**GS** minimum lies 1.96 eV above the **GS** minimum, instead of 1.42 eV with DFT. The better accuracy of the MS-CASPT2 singlet-triplet energy gap over B3LYP is confirmed by DLPNO-CCSD(T) and SC-NEVPT2 results, which predict a **GS** to ^{3}**GS** adiabatic transition at 1.85 and 2.18

eV, respectively. This large change in the S_0-T_1 relative energies between B3LYP and MS-CASPT2 has important consequences on the position of the triplet/singlet crossing points. As described in the introduction, these funnels play an important role in the sequential two-photon photoisomerization mechanism derived from the DFT results.[44] To locate these crossing points at the MS-CASPT2 level, we show in Figure 3.10 the potential energy profiles of the singlet states along the adiabatic T_1 linkage photoisomerization pathway. While four T_1/S_0 minimum energy crossing points were optimized along this pathway at the DFT level (see Figure 3.1 and Ref. [44]), only two T_1/S_0 crossing points are found with MS-CASPT2. The first one is encountered between ^{3}**GS** and ^{3}**TS1** and lies about 0.25 eV above ^{3}**GS**. The second one is located very close to ^{3}**MS1** only 0.02 eV above this minimum. The first MS-CASPT2 crossing point corresponds to the second minimum energy crossing point located with DFT at 0.67 eV above ^{3}**GS**. The second MS-CASPT2 crossing point corresponds to the fourth minimum energy crossing point located with DFT at 0.17 eV above ^{3}**MS1**. The consequences of these differences in the position of the T_1/S_0 funnels on the photoisomerization mechanism are discussed in the following subsection.

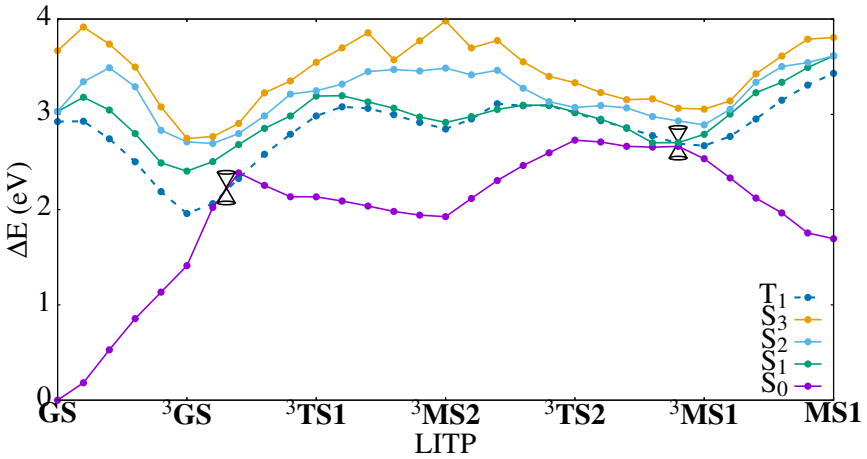

Figure 3.10 MS4-CASPT2 S_0-S_3 (full lines) and T_1 (dashed line) potential energy profiles along the adiabatic T_1 linkage photo-isomerization pathway (linearly interpolated transit path: LITP) between **GS**, ^{3}**GS**, ^{3}**TS1**, ^{3}**MS2**, ^{3}**TS2**, ^{3}**MS1** and the **MS1** DFT-optimized structures. Double-cone pictograms represent T_1/S_0 crossing points. Reprinted with permission from *J. Chem. Theory Comput*. 2017, 13, 12, 6120-6130. Copyright 2017, American Chemical Society.

3.6 N→O linkage photoisomerization mechanism revisited

After irradiation of the **GS** isomer with a blue light photon, the degenerate pair of singlet excited states S_1/S_2 of d→dπ^* nature are populated. As discussed in subsection 3.4,

efficient ISC pathways were identified driving the system to lower ^{3}MLCT states, T_1 and possibly T_2. The adiabatic T_1 PES displays an unfavorable energetic landscape along the N→O linkage photoisomerization with a high activation energy (> 1 eV) and an energetically uphill process (ΔE ^{3}**GS**→^{3}**MS1** = 0.7 eV). However, two funnels for efficient ISC between T_1 and S_0 were located, providing much more favorable nonadiabatic photoisomerization pathways. Upon relaxation to ^{3}**GS**, the system can reach a first T_1/S_0 crossing only 0.25 eV above ^{3}**GS**. Nonradiative $T_1 \rightarrow S_0$ decay can then bring the system to the **MS2** isomer. As this intermediate also absorbs light in the same blue region of the spectrum as **GS**, this species is photoexcited to ^{1}MLCT excited states (3.3 in this case; Table 3.3). Upon relaxation down to the lowest triplet state (assuming efficient radiationless decay mechanisms as the ones shown at the FC region of the **GS** isomer), the ^{3}**MS2** intermediate is expected to be populated. Subsequently, a low energy barrier (0.27 eV) has to be surmounted to complete the isomerization towards to O-bonded isomer ^{3}**MS1**. In the vicinity of this excited-state minimum, a second T_1/S_0 crossing only 0.02 eV above ^{3}**MS1** was located, allowing for efficient ISC down to the photoproduct **MS1**. In Chapter 6 we will refer to this particular photoisomerization mechanism involving multiple ISC and IC as *pathway **I***.

This mechanism is similar to the sequential two-photon absorption mechanism described in a previous DFT study.[44]. Note however, that the nonadiabatic photoisomerization pathway proposed here is more favorable than that issued from the DFT calculations. Indeed, at the B3LYP+D3 level, a minimum energy triplet/singlet crossing point was located right at the bottom of the ^{3}**GS** potential energy well, providing an efficient funnel for the photostabilization of **GS** (Figure 3.1). Due to the energy shift of the T_1 PES with respect to the S_0 PES, this crossing is removed at the MS-CASPT2 level (Figure 3.10) and the first located funnel is productive for photoisomerization, as it allows for non-radiative decay to the **MS2** isomer. In addition, once the second photon has been absorbed and the system has relaxed to the ^{3}**MS2** intermediate, another minimum energy triplet/singlet crossing point was identified at the B3LYP+D3 level, which provides a photostabilization pathway for **MS2** (Figure 1). This funnel does not exist at the MS-CASPT2 level, resulting in a more efficient ^{3}**MS2**→^{3}**MS1** adiabatic pathway. Finally, the triplet/singlet funnel located in the photoproduct region is found at the bottom of the ^{3}**MS1** potential energy well at the MS-CASPT2 level, allowing for an efficient ^{3}**MS1**→^{3}**MS1** ISC. Note that the SOC at the first and second triplet/singlet crossings are 28 cm^{-1} and 20 cm^{-1}, respectively. These values are about one order of magnitude smaller than those found between S_1 and T_3 (Figure 3.6). It can be simply explained by the El-Sayed rule,[75] as S_0 and T_1 both involve a transition at these two crossing geometries (see Table 3.4).

Another remarkable observation is that the second part of the isomerization mechanism following absorption of a second blue light photon could possibly occur on the S_1 singlet excited state. Indeed, Figure 3.10 shows that the T_1 and S_1 PES between ^{3}**MS2** and ^{3}**MS1** are quasi degenerate, allowing for efficient ISC between T_1 and S_1. Analysis of the CASSCF wavefunctions shows that both electronic states are made of the same electronic configurations over a large segment along this potential energy profile.

It is also interesting to note that, in the less probable scenario where part of the electronic population would survive long enough on the initially excited S_1 state to undergo a complete singlet photoisomerization, the potential energy landscape shown in Figure 3.8 would guarantee an efficient sequential two-photon absorption singlet mechanism as well. Indeed, upon relaxation from the FC region in the S_1 state, it is clear that the system would decay back to S_0 in a downhill process by efficient IC in the region of **TS1** where the singlet electronic states strongly couple. This would lead to efficient formation of **MS2**, which upon absorption of a second photon would bring the system to S_4. Here, the system could decay back to S_0 in another region of strong electronic coupling at **TS2**, leading to the final **MS2** photoproduct. In Chapter 6 we will refer to this photoisomerization mechanism involving exclusively IC among the singlet states as *pathway **II***.

3.7 Conclusions

We have investigated the N→O linkage photoisomerization mechanism in the trans-[RuCl(NO)(Py)$_4$]$^{2+}$complex using accurate MS-CASPT2 calculations in order to confirm previous interpretations based on DFT calculations[44] and recent experimental observations.[41] Our results provide further evidence that a multistep sequential two-photon photoisomerization mechanism requiring several ISC processes is involved. The first 473 nm photon absorption from the stable N-bonded **GS** isomer triggers a partial linkage isomerization leading to the side-on (NO-bonded) metastable **MS2** isomer. This first isomerization step involves an efficient ISC pathway from the initially populated ^{1}MLCT excited states to the lowest ^{3}MLCT excited state. Vibrational relaxation of this state leads to a N-bonded triplet intermediate (denoted ^{3}**GS**) from which an adiabatic isomerization is forbidden because of the large potential energy barrier (> 1 eV) encountered on the corresponding triplet PES. The most probable route takes place through an ISC channel via a triplet/singlet funnel leading to the **MS2** isomer. This isomer absorbs efficiently at the same wavelength and the second 473 nm photon absorption induces the completion of the N→O linkage isomerization. This second isomerization step involves ISC from ^{1}MLCT states to the lowest triplet states, followed by relaxation to a NO-bonded triplet intermediate (denoted ^{3}**MS2**) from which adiabatic isomerization to an O-bonded triplet species (denoted ^{3}**MS1**) is possible. The formation of the singlet ground-state photoproduct, the O-bonded **MS1**, is achieved through an ISC channel occurring at another triplet/singlet funnel in the photoproduct region of the PES. Note that we cannot exclude that this second part of the photoisomerization process takes place in the singlet excited state due to the proximity between the S_1 and T_1 states between ^{3}**MS2** and ^{3}**MS1**. The potential energy landscape of the singlet states would also allow for a complete sequential two-photon absorption singlet photoisomerization mechanism. However, due to the high probability of ISC with lower triplet states, the mixed singlet/triplet scenario described above is more likely.

Overall, the N→O linkage photoisomerization mechanism is similar to the one obtained

from DFT calculations.[44] The main differences result in the position of the triplet/singlet funnels due to the higher energy gap between the singlet and triplet PES. At the B3LYP+D3 level, four funnels were located. Two of them were photostabilizing (i.e., **GS** and **MS2**, respectively), while the other two were photoreactive (i.e., allowing for the first and second isomerization steps). At the CASPT2 level, there are only two crossings left, which play the role of photochemical funnels. This study has also brought useful information on the potential involvement of singlet excited states in the photoisomerization mechanism. We hope that this work will stimulate further experimental and theoretical studies in order to clarify the role of these highly intertwined singlet and triplet electronic states. In particular, time-resolved absorption spectroscopy could bring additional insights into the transient species populated along the N→O linkage photoisomerization.
In Chapter 6, we will present our own theoretical contribution on nonadiabatic dynamics simulations to shed some light on this photoisomerization mechanism.
The results of this chapter are contained in this publication: F. Talotta, J.-L. Heully, F. Alary, I. M. Dixon, L. González, and M. Boggio-Pasqua, *J. Chem. Theory Comput.*, **2017**, 13 (12), 6120-6130, DOI: 10.1021/acs.jctc.7b00982.

3.8 Supporting Information in Appendix A

Table A.1 for ^{1}**GS*** optimized TD-DFT Cartesian coordinates. Table A.2 for MS4-CASPT2 energies along the S_1 relaxation pathway **GS**→^{1}**GS***. Table A.3 for MS4-CASPT2 energies along the thermal isomerization pathway. Table A.4 for MS4-CASPT2 energies along the photoisomerization pathway. Figure A1 for different SA7-CASSCF(16,13) stable active orbitals at **MS1**. Figure A2 for MS4-CASPT2 thermal isomerization pathway using alternative active space. Figure A3 for PM-CASSCF main electronic characters along the thermal isomerization pathway. Figure A5 for CASSCF triplet energy profiles along the photoisomerization pathway. Table A2 for S_0 and T_1 configurations at the triplet/singlet funnels.

Bibliography

[1] M. Irie. Diarylethenes for memories and switches. *Chem. Rev.*, 100:1685, 2000.

[2] Y. Yokoyama. Fulgides for memories and switches. *Chem. Rev.*, 100:1717, 2000.

[3] G. Berkovic, V. Krongauz, and V. Weiss. Spiropyrans and spirooxazines for memories and switches. *Chem. Rev.*, 100:1741, 2000.

[4] K. Szacilowski. Digital information processing in molecular systems. *Chem. Rev.*, 108:3481, 2008.

[5] U. Pischel, J. Andréasson, D. Gust, and V. F. Pais. Information processing with molecules—quo vadis? *ChemPhysChem*, 14:28, 2013.

[6] U. Al-Atar, R. Fernandes, B. Johnsen, D. Baillie, and N. R. Branda. A photocontrolled molecular switch regulates paralysis in a living organism. *J. Am. Chem. Soc.*, 131:15966, 2009.

[7] W. Szymański, J. M. Beierle, H. A. V. Kistemaker, W. A. Velema, and B. L. Feringa. Reversible photocontrol of biological systems by the incorporation of molecular photoswitches. *Chem. Rev.*, 113:6114, 2013.

[8] B. L. Feringa. The art of building small: From molecular switches to molecular motors. *J. Org. Chem.*, 72:6635, 2007.

[9] T. Kim, L. Zhu, R. O. Al-Kaysi, and C. J. Bardeen. Organic photomechanical materials. *ChemPhysChem*, 15:400, 2014.

[10] H. Durr and H. Bouas-Laurent. *Photochromism: Molecules and Systems*. Elsevier: Amsterdam, 2003.

[11] H. Bouas-Laurent and H. Durr. Organic photochromism. *Pure Appl. Chem.*, 73:639, 2001.

[12] J. C. Crano and R. J. Guglielmetti. *Organic Photochromic and Thermochromic Compounds*. Kluwer Academy Publishers: New Yorw, 2002.

[13] P. Coppens, I. Novozhilova, and A. Kovalevsky. Photoinduced linkage isomers of transition-metal nitrosyl compounds and related complexes. *Chem. Rev.*, 102:861, 2002.

[14] T. E. Bitterwolf. Photochemical nitrosyl linkage isomerism/metastable states. *Coord. Chem. Rev.*, 250:1196, 2006.

[15] J. J. Rack. Electron transfer triggered sulfoxide isomerization in ruthenium and osmium complexes. *Coord. Chem. Rev.*, 253:78, 2009.

[16] B. A. McClure and J. J. Rack. Isomerization in photochromic ruthenium sulfoxide complexes. *Eur. J. Inorg. Chem.*, 2010:3895, 2010.

[17] S. O. Sylvester, J. M. Cole, and P. G. Waddell. Photoconversion bonding mechanism in ruthenium sulfur dioxide linkage photoisomers revealed by in situ diffraction. *J. Am. Chem. Soc.*, 134:11860, 2012.

[18] O. P. J. Vieuxmaire, R. E. Piau, F. Alary, J.-L. Heully, P. Sutra, A. Igau, and M. Boggio-Pasqua. Theoretical investigation of phosphinidene oxide polypyridine ruthenium(II) complexes: Toward the design of a new class of photochromic compounds. *J. Phys. Chem. A*, 117:12821, 2013.

[19] Th. Woike and S. Haussühl. Infrared-spectroscopic and differential scanning calorimetric studies of the two light-induced metastable states in $K_2[Ru(NO_2)_4(OH)(NO)]$. *Solid State Commun.*, 86:333, 1993.

[20] D. V. Fomitchev and P. Coppens. X-ray diffraction analysis of geometry changes upon excitation: The ground-state and metastable-state structures of $K_2[Ru(NO_2)_4(OH)(NO)]$. *Inorg. Chem.*, 35:7021, 1996.

[21] P. C. Ford, J. Bourassa, K. Miranda, B. Lee, I. Lorkovic, S. Boggs, S. Kudo, and L. Laverman. Photochemistry of metal nitrosyl complexes. delivery of nitric oxide to biological targets. *Coord. Chem. Rev.*, 171:185, 1998.

[22] D. V. Fomitchev, P. Coppens, T. Li, K. A. Bagley, L. Chen, and G. B. Richter-Addo. Photo-induced metastable linkage isomers of ruthenium nitrosyl porphyrins. *Chem. Commun.*, page 2013, 1999.

[23] S. C. Da Silva and D. W. Franco. Metastable excited state and electronic structure of $[Ru(NH_3)_5NO]^{3+}$ and $[Ru(NH_3)_4(OH)NO]^{2+}$. *Spectrochim. Acta, Part A*, 55:1515, 1999.

[24] S. I. Gorelsky and A. B. P. Lever. Metastable states of ruthenium (II) nitrosyl complexes and comparison with $[Fe(CN)_5NO]^{2^{\smile}}$. *Int. J. Quantum Chem.*, 80:636, 2000.

[25] E. Tfouni, M. Krieger, B. R. McGarvey, and D. W. Franco. Structure, chemical and photochemical reactivity and biological activity of some ruthenium amine nitrosyl complexes. *Coord. Chem. Rev.*, 236:57, 2003.

[26] S. Ferlay, H. W. Schmalle, G. Francese, H. Stoeckli-Evans, M. Imlau, D. Schaniel, and T. Woike. Light-induced metastable states in oxalatenitrosylruthenium(II) and terpyridinenitrosylruthenium(II) complexes. *Inorg. Chem.*, 43:3500, 2004.

[27] D. Schaniel, T. Woike, C. Boskovic, and H.-U. Güdel. Evidence for two light-induced metastable states in $Cl_3[Ru(NH_3)_5NO]H_2O$. *Chem. Phys. Lett.*, 390:347, 2004.

[28] I. Szundi, M. J. Rose, I. Sen, A. A. Eroy-Reveles, P. K. Mascharak, and Ó. Einarsdóttir. A new approach for studying fast biological reactions involving nitric oxide: Generation of no using photolabile ruthenium and manganese no donors,. *Photochem. Photobiol.*, 82:1377, 2006.

[29] T. E. Bitterwolf. Photolysis of [Ru(bipy)$_2$(NO)Cl](PF$_6$)$_2$ in frozen ionic glass matrices. evidence for nitrosyl linkage isomerism and no-loss in a physiologically relevant nitric oxide source. *Inorg. Chem. Commun.*, 11:772, 2008.

[30] M. J. Rose and P. K. Mascharak. Photoactive ruthenium nitrosyls: Effects of light and potential application as no donors. *Coord. Chem. Rev.*, 252:2093, 2008.

[31] M. J. Rose, N. L. Fry, R. Marlow, L. Hinck, and P. K. Mascharak. Sensitization of ruthenium nitrosyls to visible light via direct coordination of the dye resorufin: Trackable no donors for light-triggered no delivery to cellular targets. *J. Am. Chem. Soc.*, 130:8834, 2008.

[32] H. Giglmeier, T. Kerscher, P. Klüfers, D. Schaniel, and T. Woike. Nitric-oxide photorelease and photoinduced linkage isomerism on solid [Ru(NO)(terpy)(L)]BPh$_4$ (l = glycolate dianion). *Dalton Trans.*, page 9113, 2009.

[33] A. D. Ostrowski and P. C. Ford. Metal complexes as photochemical nitric oxide precursors: Potential applications in the treatment of tumors. *Dalton Trans.*, page 10660, 2009.

[34] A. Zangl, P. Klüfers, D. Schaniel, and T. Woike. Photoinduced linkage isomerism of RuNO6 complexes with bioligands and related chelators. *Dalton Trans.*, 6:1034, 2009.

[35] D. Schaniel, B. Cormary, I. Malfant, L. Valade, T. Woike, B. Delley, K. W. Krämer, and H.-U. Güdel. Photogeneration of two metastable no linkage isomers with high populations of up to 76% in trans-[RuCl(Py)$_4$(NO)][PF$_6$]2·1/2H$_2$O. *Phys. Chem. Chem. Phys.*, 9:3717, 2007.

[36] B. Cormary, I. Malfant, M. Buron-Le Cointe, L. Toupet, B. Delley, D. Schaniel, N. Mockus, T. Woike, K. Fejfarová, V. Petříček, and M. Dušek. [Ru(py)$_4$Cl(NO)](PF$_6$)$_2$·0.5H$_2$O: A model system for structural determination and ab initio calculations of photo-induced linkage no isomers. *Acta Crystallogr., Sect. B: Struct. Sci.*, 65:612, 2009.

[37] N. L. Fry and P. K. Mascharak. Photoactive ruthenium nitrosyls as no donors: How to sensitize them toward visible light. *Acc. Chem. Res.*, 44:289, 2011.

[38] B. Cormary, S. Ladeira, K. Jacob, P. G. Lacroix, T. Woike, D. Schaniel, and I. Malfant. Structural influence on the photochromic response of a series of ruthenium mononitrosyl complexes. *Inorg. Chem.*, 51:7492, 2012.

[39] J. Akl, I. Sasaki, P. G. Lacroix, I. Malfant, S. Mallet-Ladeira, P. Vicendo, N. Farfán, and R. Santillan. Comparative photo-release of nitric oxide from isomers of substituted terpyridinenitrosyl-ruthenium(II) complexes: Experimental and computational investigations. *Dalton Trans.*, 43:12721, 2014.

[40] T. R. deBoer and P. K. Mascharak. Recent progress in photoinduced no delivery with designed ruthenium nitrosyl complexes. *Adv. Inorg. Chem.*, 67:145, 2015.

[41] L. Khadeeva, W. Kaszub, M. Lorenc, I. Malfant, and M. Buron-Le Cointe. Buron-le cointe, m. two-step photon absorption driving the chemical reaction in the model ruthenium nitrosyl system $[Ru(py)_4Cl(NO)](PF_6)2{\cdot}1/2H_2O$. *Inorg. Chem.*, 55:4117, 2016.

[42] M. Tassé, H. S. Mohammed, C. Sabourdy, S. Mallet-Ladeira, P. G. Lacroix, and I. Malfant. Synthesis, crystal structure, spectroscopic, and photoreactive properties of a ruthenium(II)-mononitrosyl complex. *Polyhedron*, 119:350, 2016.

[43] J. Sanz García, F. Alary, M. Boggio-Pasqua, I. M. Dixon, and J.-L. Heully. Is photoisomerization required for no photorelease in ruthenium nitrosyl complexes? *J. Mol. Model.*, 22:284, 2016.

[44] J. Sanz García, F. Alary, M. Boggio-Pasqua, I. M. Dixon, I. Malfant, and J.-L. Heully. Establishing the two-photon linkage isomerization mechanism in the nitrosyl complex trans-$[RuCl(NO)(py)_4]^{2+}$ by DFT and TDDFT. *Inorg. Chem.*, 54:8310, 2015.

[45] C. Daniel and C. Gourlaouen. Chemical bonding alteration upon electronic excitation in transition metal complexes. *Coord. Chem. Rev.*, 344:131, 2017.

[46] I. Ciofini, C. A. Daul, and C. Adamo. Phototriggered linkage isomerization in ruthenium-dimethylsulfoxyde complexes: Insights from theory. *J. Phys. Chem. A*, 107:11182, 2003.

[47] A. J. Göttle, I. M. Dixon, F. Alary, J.-L. Heully, and M. Boggio-Pasqua. Adiabatic versus nonadiabatic photoisomerization in photochromic ruthenium sulfoxide complexes: A mechanistic picture from density functional theory calculations. *J. Am. Chem. Soc.*, 133:9172, 2011.

[48] A. J. Göttle, F. Alary, I. M. Dixon, J.-L. Heully, and M. Boggio-Pasqua. Unravelling the s$\rightarrow$o linkage photoisomerization mechanisms in cis- and trans-$[Ru(bpy)_2(DMSO)_2]^{2+}$ using density functional theory. *Inorg. Chem.*, 53:6752, 2014.

[49] H. Li, L. Zhang, Y. Wang, and X. Fan. Theoretical studies on the photoisomerization mechanism of osmium(II) sulfoxide complexes. *RSC Adv.*, 5:58580, 2015.

[50] H. Li, L. Zhang, I. Zheng, X. Li, X. Fan, and Y. Zhao. Photoisomerization mechanism of ruthenium sulfoxide complexes: Role of the metal-centered excited state in the bond rupture and bond construction processes. *Chem. - Eur. J.*, 22:14285, 2016.

[51] G. A. Crosby and J. N. Demas. Quantum efficiencies on transition metal complexes. II. charge-transfer luminescence. *J. Am. Chem. Soc.*, 93:2841, 1971.

[52] J. N. Demas and D. G. Taylor. Intersystem crossing" yields in ruthenium(II) and osmium(II) photosensitizers. *Inorg. Chem.*, 18:3177, 1979.

[53] A. Juris, V. Balzani, F. Barigelletti, S. Campagna, P. Belser, and A. Von Zelewsky. Ru(II) polypyridine complexes: Photophysics, photochemistry, electrochemistry, and chemiluminescence. *Coord. Chem. Rev.*, 84:85, 1988.

[54] N. H. Damrauer, G. Cerullo, A. Yeh, T. R. Boussie, C. V. Shank, and J. K. McCusker. Femtosecond dynamics of excited-state evolution in [Ru(bpy)$_3$]$^{2+}$. *Science*, 275:54, 1997.

[55] A. T. Yeh, C. V. Shank, and J. K. McCusker. Ultrafast electron localization dynamics following photo-induced charge transfer. *Science*, 289:935, 2000.

[56] S. Campagna, F. Puntoriero, F. Nastasi, G. Bergamini, and V. Balzani. Photochemistry and photophysics of coordination compounds: Ruthenium. *Top. Curr. Chem.*, 280:117, 2007.

[57] C. Daul, E. J. Baerends, and P. Vernooijs. A density functional study of the mlct states of [Ru(bpy)$_3$]$^{2+}$ in d3 symmetry. *Inorg. Chem.*, 33:3538, 1994.

[58] J.-L. Heully, F. Alary, and M. Boggio-Pasqua. Spin-orbit effects on the photophysical properties of Ru(bpy)$_3^{2+}$. *J. Chem. Phys.*, 131:184308, 2009.

[59] C. Daniel, N. Ferré, M. Filatov, and M. Huix-Rotllant. Absorption spectroscopy, emissive properties, and ultrafast intersystem crossing processes in transition metal complexes: TD-DFT and spin-orbit coupling. *Top. Curr. Chem.*, 368:377, 2015.

[60] L. Freitag and L. González. Theoretical spectroscopy and photodynamics of a ruthenium nitrosyl complex. *Inorg. Chem.*, 53:6415, 2014.

[61] L. Freitag, S. Knecht, S. F. Keller, M. G. Delcey, F. Aquilante, T. B. Pedersen, R. Lindh, M. Reiher, and L. González. Orbital entanglement and CASSCF analysis of the ru–no bond in a ruthenium nitrosyl complex. *Phys. Chem. Chem. Phys.*, 17:14383, 2015.

[62] A. J. Atkins, F. Talotta, L. Freitag, M. Boggio-Pasqua, and L. González. Assessing excited state energy gaps with time-dependent density functional theory on ru(II) complexes. *J. Chem. Theory Comput.*, 13:4123, 2017.

[63] J. Finley, P.-Ă. Malmqvist, B. O. Roos, and L. Serrano-Andrés. The multi-state CASPT2 method. *Chem. Phys. Lett.*, 288:299, 1998.

[64] G. Ghigo, B. O. Roos, and P.-Ă. Malmqvist. A modified definition of the zeroth-order hamiltonian in multiconfigurational perturbation theory (CASPT2). *Chem. Phys. Lett.*, 396:142, 2004.

[65] J. P. Zobel, J. J. Nogueira, and L. González. The ipea dilemma in CASPT2. *Chem. Sci.*, 8:1482, 2017.

[66] F. Aquilante, J. Autschbach, R. K. Carlson, L. F. Chibotaru, M. G. Delcey, L. De Vico, I. F. Galván, N. Ferré, L. M. Frutos, L. Gagliardi, M. velli, A. Giussani, C. E. Hoyer, G. L. Manni, H. Lischka, D. Ma, P. Ă. Malmqvist, T. Müller, A. Nenov, M. Olivucci, T. B. Pedersen, D. Peng, F. ser, B. Pritchard, M. Reiher, I. Rivalta, I. Schapiro, J. Segarra-Martí, M. Stenrup, D. G. Truhlar, L. Ungur, A. Valentini, S. Vancoillie, V. P. Veryazov, nd Vysotskiy, O. Weingart, F. Zapata, and R. Lindh. Molcas 8: New capabilities for multiconfigurational quantum chemical calculations across the periodic table. *J. Comput. Chem.*, 37:506, 2016.

[67] C. Angeli, R. Cimiraglia, S. Evangelisti, T. Leininger, and J.-P. Malrieu. Introduction of n-electron valence states for multireference perturbation theory. *J. Chem. Phys.*, 114:10252, 2001.

[68] F. Weigend and R. Ahlrichs. Balanced basis sets of split valence, triple zeta valence and quadruple zeta valence quality for h to rn: Design and assessment of accuracy. *Phys. Chem. Chem. Phys.*, 7:3297, 2005.

[69] D. Andrae, U. Häußermann, M. Dolg, H. Stoll, and H. Preuß. Energy-adjusted ab initio pseudopotentials for the second and third row transition elements. *Theor. Chim. Acta*, 77:123, 1990.

[70] C. Riplinger, B. Sandhoefer, A. Hansen, and F. Neese. Natural triple excitations in local coupled cluster calculations with pair natural orbitals. *J. Chem. Phys.*, 139:134101, 2013.

[71] F. Neese. The orca program system. *WIREs Comput. Mol. Sci.*, 2:73, 2012.

[72] P.-Ă. Malmqvist, B. O. Roos, and B. Schimmelpfennig. The restricted active space (ras) state interaction approach with spin–orbit coupling. *Chem. Phys. Lett.*, 357:230, 2002.

[73] J. Wang, S. Manivasagam, and A. K. Wilson. Multireference character for 4d transition metal-containing molecules. *J. Chem. Theory Comput.*, 11:5865, 2015.

[74] B. J. Coe, T. J. Meyer, and P. S. White. Synthetic and structural studies on trans-tetrapyridine complexes of ruthenium(II). *Inorg. Chem.*, 34:593, 1995.

[75] J. Eng, C. Gourlaouen, E. Gindensperger, and C. Daniel. Spin-vibronic quantum dynamics for ultrafast excited-state processes. *Acc. Chem. Res.*, 48:809, 2015.

[76] M. Etinski, J. Tatchen, and C. M. Marian. Time-dependent approaches for the calculation of intersystem crossing rates. *J. Chem. Phys.*, 134:154105, 2011.

[77] M. Etinski, V. Rai-Constapel, and C. M. Marian. Time-dependent approach to spin-vibronic coupling: Implementation and assessment. *J. Chem. Phys.*, 140:114104, 2014.

[78] A. A. Granovsky. Extended multi-configuration quasi-degenerate perturbation theory: The new approach to multi-state multi-reference perturbation theory. *J. Chem. Phys.*, 134:214113, 2011.

[79] M. A. El-Sayed. Spin-orbit coupling and the radiationless processes in nitrogen heterocyclics. *J. Chem. Phys.*, 38:2834, 1963.

[80] J. K. McCusker. Femtosecond absorption spectroscopy of transition metal charge-transfer complexes. *Acc. Chem. Res.*, 36:876, 2003.

[81] L. S. Forster. Intersystem crossing in transition metal complexes. *Coord. Chem. Rev.*, 250:2023, 2006.

[82] M. Chergui. Ultrafast photophysics of transition metal complexes. *Acc. Chem. Res.*, 48:801, 2015.

[83] A. Vlček and S. Záliš. Modeling of charge-transfer transitions and excited states in d6 transition metal complexes by DFT techniques. *Coord. Chem. Rev.*, 251:258, 2007.

[84] T. J. Lee, J. E. Rice, G. E. Scuseria, and H. F. Schaefer. Theoretical investigations of molecules composed only of fluorine, oxygen and nitrogen: Determination of the equilibrium structures of FOOF, $(NO)_2$ and FNNF and the transition state cture for FNNF cis-trans isomerization. *Theor. Chim. Acta*, 75:81, 1989.

[85] T. J. Lee and P. R. Taylor. A diagnostic for determining the quality of single-reference electron correlation methods. *Int. J. Quantum Chem.*, 36:199, 1989.

Chapter 4

$NO^{\bullet}$ Photorelease in trans-$[RuCl(NO)(Py)_4]^{2+}$

4.1 Context and Previous Theoretical Studies

As explained in Chapter 1, besides their ability to undergo linkage photoisomerizations, ruthenium nitrosyl complexes can also release nitric oxide upon light irradiation (Figure 4.1). In particular, De Candia et al.[1] have shown that trans-$[RuCl(NO)(Py)_4]^{2+}$can photorelease $NO^{\bullet}$ albeit with a low quantum yield (ϕ_{NO}=1.6·10^{-3} mol·einstein^{-1}) in aqueous solution and upon blue light irradiation at 473 nm (see Figure 1.6). The mechanism for $NO^{\bullet}$ photorelease is important since this radical is involved in various physiological processes.

Previous experimental studies[2;3] in solid phase have shown that the photoproducts of both

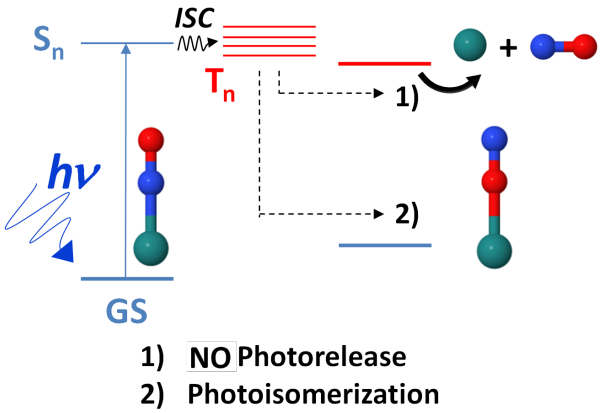

Figure 4.1 Scheme of the possible photoreactions pathways that ruthenium nitrosyl complexes may undergo after light irradiation.

N→O linkage photoisomerization and $NO^{\bullet}$ photorelease could be observed, suggesting that linkage isomers of nitric oxide are likely intermediates in the photolytic release of $NO^{\bullet}$. There are very few theoretical studies devoted to $NO^{\bullet}$ photorelease. The initial stages of $NO^{\bullet}$ photorelease was investigated dynamically for the trans-$[RuCl(NO)(Py)_4]^{2+}$complex (where $PaPy_3$=N,N'-bis(2-pyridylmethyl)amine-N-ethyl-2-pyridine-2-car-boxamide).[4] But no key excited-state intermediates could be assigned to be responsible for the photorelease from these simulations. Later, a static DFT study[5] investigating the lowest triplet potential energy surfaces of different ruthenium nitrosyl complexes identified the ^{3}**MS2** as the key intermediate for $NO^{\bullet}$ photorelease. The energy profiles for the $NO^{\bullet}$ photorelease pathways for the trans-$[RuCl(NO)(Py)_4]^{2+}$complex are shown in Figure 4.2. They are based on the use of the B3LYP-D3 functional. They show that the ^{3}**MS2** intermediate is the one that requires less energy to dissociate Ru-NO, in agreement with the fact that the ^{3}**MS2** intermediate is the highest energy triplet-state intermediate at this level of calculation. However, these energy profiles also reveal a wrong physical behavior at the asymptotic limit, as the energy is still substantially decreasing when the Ru-NO distance is increasing beyond 9 Å. If we write formally the chemical equations for the photorelease pathway, because the triplet excited states ^{3}**GS**, ^{3}**MS2** and ^{3}**MS1** have MLCT character (see Chapter 3), the ruthenium center is RuIII and one could write:

$$[Ru^{II}Cl^{-}(NO^{+})(Py)_4]^{2+} \xrightarrow{h\nu} [Ru^{III}Cl^{-}(NO^{0})(Py)_4]^{2+} \rightarrow [Ru^{III}Cl^{-}(Py)_4]^{\bullet 2+} + NO^{\bullet} \tag{4.1}$$

Although we know from a previous theoretical study[6] that it is not possible to assign such clear formal oxidation states to these species, it allows us to have a simple chemical representation of the expected fragments. From equation (4.1), the Ru-NO photodissociation should produce two doublet states (radicals). Thus, the expected spin densities of these fragments should be equal to 1 exactly. But in the B3LYP-D3 calculations, these spin densities are 1.2 and 0.8, respectively for $[Ru^{III}Cl^{-}(Py)_4]^{\bullet 2+}$ and $NO^{\bullet}$, indicating an artificial electron (charge) transfer between the $NO^{\bullet}$ and $[Ru^{III}Cl^{-}(Py)_4]^{\bullet 2+}$ fragments. In addition, the $NO^{\bullet}$ radical has a doubly-degenerate $X^2\Pi$ ground state, which cannot be physically described with a mono-configurational representation of the wavefunction. More recently, a CASSCF-in-DFT embedding approach was used to explore the ground and excited electronic states of the trans-$[RuCl(NO)(Py)_4]^{2+}$complex along the Ru-NO stretching normal mode.[7] However, vibrational relaxation in the excited states was not taken into account and no information on the intermediates responsible for the $NO^{\bullet}$ photorelease was provided.

In this chapter, we will present the results of accurate multireference ab initio MS-CASPT2 calculations along the $NO^{\bullet}$ photorelease pathways in order to verify the validity of the DFT calculations previously reported[5] on the trans-$[RuCl(NO)(Py)_4]^{2+}$complex and to identify the most likely intermediate for $NO^{\bullet}$ photorelease.

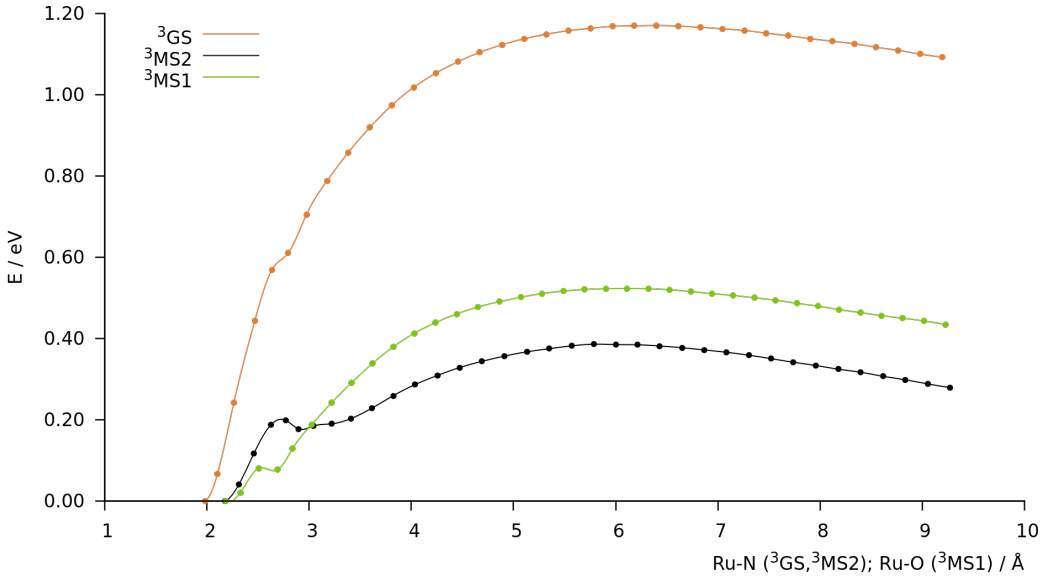

Figure 4.2 Minimum Energy Path (MEP) for the Ru-NO dissociation of trans-$[RuCl(NO)(Py)_4]^{2+}$at the DFT (B3LYP-D3) level in vacuum. The zero energy has been set to the energy of the ^{3}**GS**, ^{3}**MS2** and ^{3}**MS1** minima respectively for each MEP.[8]

4.2 Computational Section

As for the linkage photoisomerization study reported in Chapter 3, we have used the CASSCF/ CASPT2 approaches to describe the potential energy surfaces of the singlet ground state and lowest triplet excited states along the Ru-NO photodissociation pathways. Because of the issues with the B3LYP-D3 energy profiles, we have used the geometries coming out from relaxed scans along the Ru–NO bond distance using the CAM-B3LYP functional. The active space chosen for the reference CASSCF calculations is shown in Figure 4.3. It was reduced to a CASSCF(14,10), compared to the CASSCF(16,13) that was used in the photoisomerization study, deleting orbital $d_{x_2-y_2} + \sigma_{Py}$, its virtual counterpart $d_{x_2-y_2} - \sigma_{Py}$ and the virtual $d_{z^2} - \sigma^*$ (see Figure 3.2). The first two orbitals are notably not very important for the static correlation, and furthermore they are rapidly replaced by two other orbitals outside the active space. The third discarded orbital is also replaced with another orbital outside the active space, which breaks the degeneracy of the system along the Ru-NO dissociation potential energy surfaces. Other sizes of active space have been tested, in particular CASSCF(16,13) and CASSCF(14,11). Nevertheless, the CASSCF(14,10) proved to be the most stable with the proper asymptotic degeneracy expected for three consecutive pairs of singlet and triplet excited states (vide infra).
The CASSCF calculations were performed averaging over 6 states for each spin state (singlet and triplet), in order to obtain good asymptotic behavior (degeneracies of pairs of electronic states due to the doubly-degenerate $X^2\Pi$ state of $NO^\bullet$) of the potential energy surfaces at the asymptotic region. For the same reason, MS-CASPT2 was carried out

over 6 states. However, the MS-CASPT2 outcomes resulted to be extremely unstable at the asymptotic region because of artificial state mixing breaking the degeneracy of the doubly-degenerate $X^2\Pi$ state of NO•. This is a well-known issue of MS-CASPT2 which can occur when the electronic states are either nearly or perfectly degenerate.[9] Accordingly, then only the SS-CASPT2 excited-state energies were taken into account. All CASSCF and

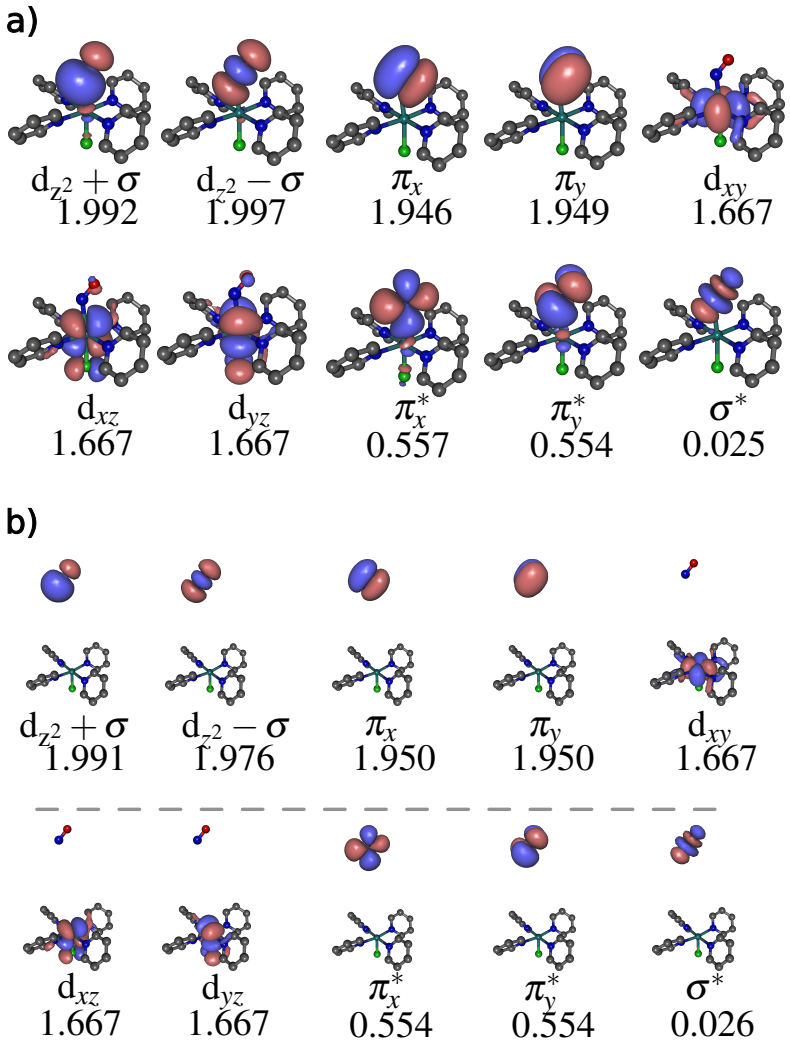

Figure 4.3 SA6-CASSCF(14,10) active space orbitals for the ^{3}**GS** isomer, and their respective average occupation numbers for the triplet states (a) at the ^{3}**GS** minimum and (b) at a Ru-(NO) distance of 12 Å.

CASPT2 calculations were performed with the OpenMolcas program package,[10] using the Cholesky decomposition algorithm with a two-electron decomposition threshold of 10^{-6}. This precision in the two-electron integrals was required to solve some degeneracy issues at the dissociation asymptotic region. The DFT calculations were performed with Gaussian 09.[11]

4.3 Results and Discussion

As explained in Chapter 3 through the calculations of singlet and triplet excited states along the initial relaxation pathway in the lowest singlet excited state populated upon blue light irradiation, and as further confirmed in Chapter 6 by "on-the-fly" nonadiabatic simulations, ICs and ISCs are expected to efficiently populate the lowest triplet excited state T_1. On this T_1 PES, three intermediates have been located: ^{3}**GS**, ^{3}**MS2** and ^{3}**MS1**. The sequential two-photon absorption N→O linkage photoisomerization mechanism presented earlier shows that, while ^{3}**GS** is expected to be populated very rapidly upon the first photon absorption, population of ^{3}**MS2** and ^{3}**MS1** require the absorption of a second photon from the metastable **MS2** ground-state isomer. This is made possible due to the fact that **MS2** absorbs light efficiently in the same spectral range as **GS**. Thus, while ^{3}**GS**, ^{3}**MS2** and ^{3}**MS1** are most likely sequentially populated along the triplet photoisomerization pathway (note that at this stage we cannot discard a singlet photoisomerization mechanism; see Chapter 3), these intermediates are all potential candidates for NO$^\bullet$ photorelease. Thus, we have computed the Ru-NO photodissociation potential energy profiles starting from each intermediate. The results of the CASPT2 calculations are represented in Figure 4.4. The first important result that comes out of these potential energy profiles is that the lowest pair of singlet states S_0/S_1 and the lowest pair of triplet states T_1/T_2 all dissociate to the same asymptote. Figures 4.4(a) and 4.4(b) show that the complex dissociates to $[RuCl(Py)_4]^{\bullet 2+}$ + NO$^\bullet$, with the pentacoordinated complex bearing its unpaired electron in the d_{xz} orbital of the Ru center, while NO$^\bullet$ has its unpaired electron either in a π_x or π_y orbital. Of course, the two doublet states of the dissociated fragments can be spin-coupled in a singlet or in a triplet state without changing the asymptotic limit. For the same reason, the next two pairs of singlet and triplet states are also degenerate between each other: S_2/S_3 and T_3/T_4 dissociate to an excited state of $[RuCl(Py)_4]^{\bullet 2+}$ + NO$^\bullet$ with the metal fragment bearing its unpaired electron in the dxy orbital of the Ru center and NO$^\bullet$ in its doublet degenerate $X^2\Pi$ state. Finally, the third pair of singlet states S_4/S_5 is degenerate with T_5/T_6 where the complex is now having its unpaired electron in the d_{yz} orbital of the ruthenium. It is of course important to remember that these potential energy profiles are based on the underlying CAM-B3LYP relaxed scans performed on the lowest triplet state T_1 using an unrestricted formalism. Thus, assuming that CAM-B3LYP provides reasonable structures along this scan (the CAM-B3LYP does not suffer from the artificial charge transfer between the dissociated fragments observed in B3LYP giving the expected spin densities of 1.0 for the metal complex and the NO$^\bullet$ fragments and the correct asymptotic behavior), the CASPT2 potential energy profiles for the T_1 state shown in Figures 4.4 (b),(d),(f) are a good approximation of the minimum energy paths for the photodissociation in the lowest triplet excited state from ^{3}**GS**, ^{3}**MS2** and ^{3}**MS1**, respectively. Note also that the relaxed pentacoordinated complex presents a C_2 symmetry resulting from Jahn-Teller effects (which break the C_4 symmetry of the doubly-degenerate E state).

Regarding photodissociation from ^{3}**GS** (Figure 4.4 b), there is a fairly good agreement between the CAM-B3LYP and CASPT2 potential energy profiles with dissociation

energies of 0.91 eV and 0.96 eV, respectively, and smooth dissociation curves (weak state coupling). For ^{3}**MS2** and ^{3}**MS1**, the situation is very different with large deviations between the CAM-B3LYP and CASPT2 curves (Figures 4.4 (d),(f)). While CAM-B3LYP predicts dissociation energies of 0.08 eV and 0.41 eV, respectively, the corresponding values at the CASPT2 level are 0.25 eV and 0.67 eV. In addition, Figure 4.4 (d) shows a complex picture for the photodissociation curves from ^{3}**MS2** with many crossings occurring between the lowest triplet states including T_1. In particular, a local potential energy well is created on the T_1 PES due to the T_1/T_2 crossing. It is worth noting that this minimum is also visible at the CAM-B3LYP level, and is also associated with a change of the electronic configuration in the unrestricted Kohn-Sham solution. Overall, while the energetics are substantially different between the DFT and wavefunction-based methods, the qualitative behavior is similar between the two approaches and the intermediate triplet species predicted to have the lowest Ru–NO dissociation energy is ^{3}**MS2**, in agreement with the previous DFT study.[5]

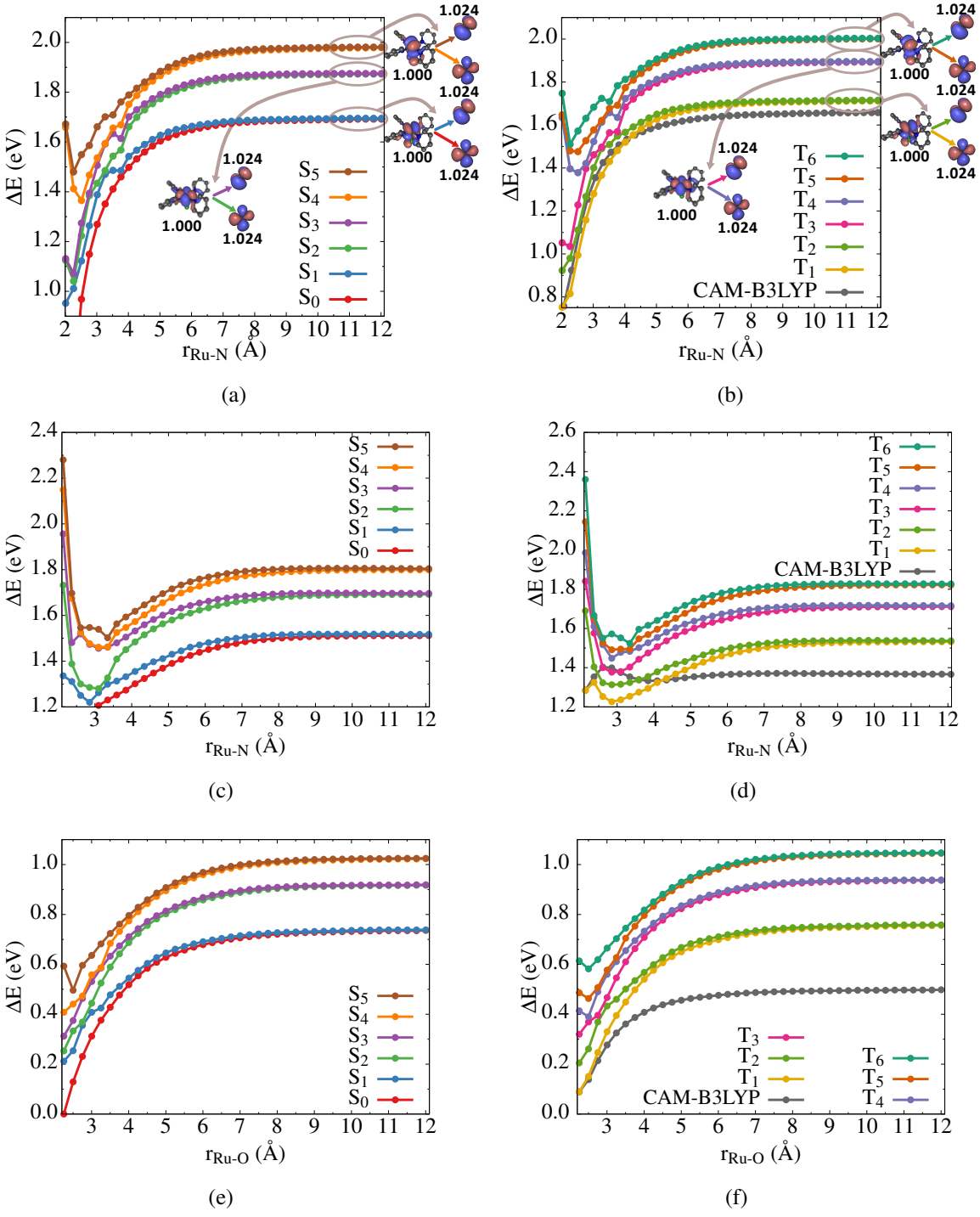

Figure 4.4 CASPT2 potential energy profiles along the Ru-NO or Ru-ON photodissociation for singlet states (left) and triplet states (right). Top, middle and bottom panels refer to photodissociation from ^{3}**GS**, ^{3}**MS2** and ^{3}**MS1**, respectively. The zero energy is set to the S_0 electronic state. The CAM-B3LYP result is shown in (b), (d) and (f) for each isomer. The asymptotic hole/particle molecular orbitals are also shown for each pair of degenerate states. The state specific CASSCF occupation numbers for the corresponding MOs are indicated in bold.

4.4 Conclusions

The calculations presented in this chapter confirm the conclusion of a previous DFT study,[5] which predicted the ^{3}**MS2** intermediate to be the most likely candidate for NO• photorelease. Here, by using a multiconfigurational wave function and by treating several pairs of singlet and triplet states simultaneously, we address correctly the bond dissociation process and the degeneracies between the electronic states. Of course, these calculations are only considering the NO• photorelease mechanism for an isolated complex. In solution, one needs to take into account solvent molecules explicitly, as a solvent molecule may come inside the coordination sphere of the ruthenium center as the NO• radical is being released. Overall, the photorelease mechanism for the isolated trans-[RuCl(NO)(Py)$_4$]$^{2+}$complex can be summarized as shown in Figure 4.5: Following blue-light irradiation of the GS isomer, the system is brought into a singlet excited state (^{1}ES) which efficiently relaxes (see Chapter 3 and Chapter 6) to the ^{3}**GS** excited-state intermediate. This species can possibly relax towards **MS2** from which the absorption of a second blue-light photon takes place, population again singlet excited states (^{1}ES'). From the side-on **MS2** isomer, the relaxation in the excited states will most likely predominantly populate the ^{3}**MS2** intermediate. This triplet side-on species can then either isomerize to the O-bonded ^{3}**MS1** (and eventually to **MS1**) or photorelease NO• because of the low Ru-NO dissociation energy required from this species. Thus, a partial isomerization is at least required to trigger NO• photorelease. The results of this chapter will be contained in a paper in preparation.

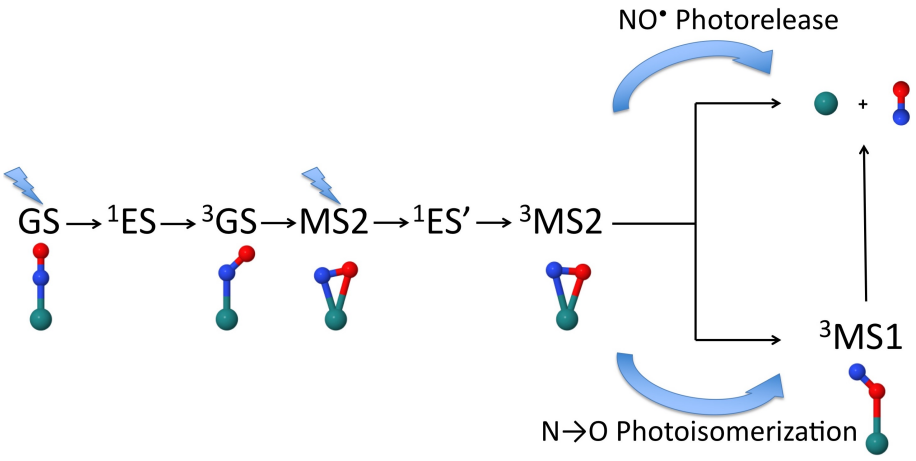

Figure 4.5 Scheme for the competitive and intricated N→O linkage photoisomerization and NO• photorelease mechanism.

Bibliography

[1] A. G. De Candia, J. P. Marcolongo, R. Etchenique, and L. D. Slep. Widely differing photochemical behavior in related octahedral Ru-NO6 compounds: Intramolecular redox isomerism of the excited state controlling the photodelivery of NO. *Inorg. Chem.*, 49(15):6925–6930, 2010. PMID: 20578716.

[2] T. Bitterwolf. Photolysis of $[Ru(bipy)_2(NO)Cl](PF_6)^{2+}$ in frozen ionic glass matrices. evidence for nitrosyl linkage isomerism and no-loss in a physiologically relevant nitric oxide source. 11:772–773, 2008.

[3] Nitric-oxide photorelease and photoinduced linkage isomerism on solid $[Ru(NO)(terpy)(L)]BPh_4$ (l = glycolate dianion). *Dalton Trans.*, 2009(42), 2009.

[4] L. Freitag and L. González. Theoretical spectroscopy and photodynamics of a ruthenium nitrosyl complex. *Inorg. Chem.*, 53:6415, 2014.

[5] J. Sanz García, F. Alary, M. Boggio-Pasqua, I. M. Dixon, and J.-L. Heully. Is photoisomerization required for NO photorelease in ruthenium nitrosyl complexes? *J. Mol. Model.*, 22:284, 2016.

[6] L. Freitag, S. Knecht, S. F. Keller, M. G. Delcey, F. Aquilante, T. B. Pedersen, R. Lindh, M. Reiher, and L. González. Orbital entanglement and CASSCF analysis of the Ru–NO bond in a ruthenium nitrosyl complex. *Phys. Chem. Chem. Phys.*, 17:14383, 2015.

[7] A. P. de Lima Batista, A. G. S. de Oliveira-Filho, and S. E. Galembeck. Photophysical properties and the no photorelease mechanism of a ruthenium nitrosyl model complex investigated using the CASSCF-in-DFT embedding approach. *Phys. Chem. Chem. Phys.*, 19:13860–13867, 2017.

[8] J. Sanz García. *Theoretical Study of New Nitrosyl Ruthenium Complexes: Mechanisms of Photoisomerization and Photorelease of NO*. PhD thesis, Université Toulouse 3 - Paul Sabatier, https://tel.archives-ouvertes.fr/tel-01402497, 2016.

[9] A. A. Granovsky. Extended multi-configuration quasi-degenerate perturbation theory: The new approach to multi-state multi-reference perturbation theory. *J.Chem. Phys.*, 134(21):214113, 2011.

[10] Openmolcas 2.1. https://gitlab.com/Molcas/OpenMolcas.

[11] H. B. Schlegel G. E. Scuseria M. A. Robb J. R. Cheeseman G. Scalmani V. Barone B. Mennucci G. A. Petersson H. Nakatsuji M. Caricato X. Li H. P. Hratchian A. F. Izmaylov J. Bloino G. Zheng J. L. Sonnenberg M. Hada M. Ehara K. Toyota R. Fukuda J. Hasegawa M. Ishida T. Nakajima Y. Honda O. Kitao H. Nakai T. Vreven J.

A. Montgomery Jr. J. E. Peralta F. Ogliaro M. Bearpark J. J. Heyd E. Brothers K. N. Kudin V. N. Staroverov R. Kobayashi J. Normand K. Raghavachari A. Rendell J. C. Burant S. S. Iyengar J. Tomasi M. Cossi N. Rega J. M. Millam M. Klene J. E. Knox J. B. Cross V. Bakken C. Adamo J. Jaramillo R. Gomperts R. E. Stratmann O. Yazyev A. J. Austin R. Cammi C. Pomelli J. W. Ochterski R. L. Martin K. Morokuma V. G. Zakrzewski G. A. Voth P. Salvador J. J. Dannenberg S. Dapprich A. D. Daniels Ö. Farkas J. B. Foresman J. V. Ortiz J. Cioslowski M. J. Frisch, G. W. Trucks and D. J. Fox.

Chapter 5

Assessment of the DFT Functionals

A set of density functionals coming from different rungs on Jacob's ladder were employed to evaluate the electronic excited states trans-$[RuCl(NO)(Py)_4]^{2+}$. While most studies on the performance of density functionals compare the vertical excitation energies, in this work we focus on the energy gaps between the electronic excited states, of the same and different multiplicity. Excited state energy gaps are important for example to determine radiationless transition probabilities. Besides energies, a functional should deliver the correct state character and state ordering. Therefore, wavefunction overlaps are introduced to systematically evaluate the effect of different functionals on the character of the excited states. As a reference, the energies and state characters from MS-CASPT2 retrieved from Chapter 3 are used. In comparison to MS-CASPT2, it is found that while hybrid functionals provide better vertical excitation energies, pure functionals typically give more accurate excited state energy gaps. Pure functionals are also found to reproduce the state character and ordering in closer agreement to MS-CASPT2 than the hybrid functionals.

5.1 Introduction

DFT is considered the modern day workhorse of theoretical chemistry [1–3]. This is because of its low computational cost versus comparitively good accuracy, in comparison to wavefunction methods with a similar cost, as explained in Chapter 2. Likewise, TD-DFT has seen widespread use for the calculation of the electronic spectra of molecules. [4–9] However, both, DFT and TD-DFT suffer from the fact that the exact form of the XC functional used in determining the electronic properties is not known and thus, has to be approximated. As a consequence, there exist many functionals which are parameterized differently for determining specific properties. As there is not just one class of functionals but many which comprise the different rungs of Jacob's ladder, [10] approaching a new problem always involves choosing the correct functional best suited for your system and property of interest. This requires systematic testing [11] and comparison

to a benchmark, be it experimental or coming from very accurate quantum chemical methods. One limitation of DFT, and of any single-configurational method, is its inability to describe multi-reference systems. For instance, in many transition metals the issue of multi-reference character is quite prevalent, especially in the 3d elements. One quintessentially pathological case is Cr_2[12].

For the calculation of excited state properties, the use of TD-DFT is very practical, especially for large molecules, but it has additional limitations. A well-known problem is the severe underestimation of charge-transfer excited states[13;14]. This can be most problematic when using XC functionals based on GGA, as the use of HF exact exchange within a functional partially alleviates this error.[15] Better improvement is achieved with range-separated functionals like CAM-B3LYP[16], which split the two-electron operator into a short- and long-range component. Rydberg states also tend to be poorly treated by most DFT functionals due to the wrong asymptotic character of the potential far away from the atom by most functionals. Including HF exact exchange also partially helps as the HF exchange has the correct $\frac{1}{R}$ dependence. However, the LB94 functional[17] is more suitable in this case, since it employs a model potential that fixes the character at long range. Because the correct asymptotic character is also lost at short range and alters more local properties, the SAOP functional[18;19] was designed with a model potential that fixes the asymptotic character of both the long and short range. The strengths and weaknesses of TD-DFT are discussed in Refs. 20 and 21. Furthermore, the use of TD-DFT in dynamics is discussed in detail in Ref. 22.

A number of benchmark studies exist in the literature[23;24] covering properties for different systems, most often organic molecules where large scale testing over hundreds of molecules is not prohibitively expensive. One example is the benchmark study of Jacquemin and coworkers on the calculation of excitation energies of a series of small organic molecules with TD-DFT.[25] Other benchmark studies have focused on the functional performance for indigoïd dyes[26], singlet-triplet vertical energies of organic molecules[27], endoperoxides[28], etc. Note also the excellent review of TD-DFT benchmarking performed before 2013 by Laurent et al.[3]. Comparative studies of DFT on transition metal complexes are also abundant in the literature. A review from Truhlar and Cramer provides an overview of a number of TD-DFT applications to transition metal complexes up to 2009.[1] In Ref. 29, a systematic evaluation of the d-d transitions in aquated ion complexes using TD-DFT and Ligand Field DFT is provided. Many of the transition metal complex benchmarks consider a specific collection of transition metal complexes with a given motif. One example is the analysis of bacteriochlorins by Petit et al.[30], who also investigated the effects of basis set on TD-DFT for optical excitations in transition metal complexes[31]. Schultz et al.[32] studied the effect of functional choice on a series of 3d transition metal atom cations. Garino et al.[33] wrote a review on the photochemistry of transition metal complexes calculated using DFT. Barone and coworkers[34] investigated the vertical excitation energies of several Pt(II) and Ir(II) complexes with TD-DFT in comparison with the experiment. See also the work of Körbel et al.[35] on small transition metal complexes comparing TD-DFT with Bethe-Salpeter calculations. In all of these studies only vertical excitation energies are

considered, as these are easiest to compare to experiment and under/overestimations can be fixed with a post energy shift in the spectrum, as, for example, done in X-ray spectroscopy of transition metal complexes.[36–39] In contrast, the assessment of calculated energy gaps between excited states has been mostly overlooked despite it being significantly affected by the approximation used. One representative example is the splitting of the pre-edge peaks in acetyl and vinylferrocene K-edge spectra,[36] where the splittings can be overestimated up to 1 eV. Accurate energy gaps are also important for the correct simulation of non-adiabatic excited state dynamics as the separation between the electronic states drives the probability to populate a lower-lying state. For example, in trajectory surface-hopping molecular dynamics methods[40], the energy gap between two electronic states strongly influences the selection of the active state. Likewise, when dynamical transitions from singlet to triplet states are considered,[41;42] the size of the singlet-triplet and triplet-triplet gaps is also of paramount importance to promote intersystem crossing. In the context of radiationless transitions, the nature of the excited states involved within a transition is also relevant. For example, for intersystem crossing from singlet to triplet states, the character of the wavefunctions will determine the extent of SOC between those states in the context of the El-Sayed rules.[43;44] A few number of recent papers have focused on the accuracy of SOCs obtained from different methods.[45–47]

In this chapter, we present an extensive TD-DFT benchmark study of vertical singlet, triplet, and singlet-triplet energy gaps of the trans-$[RuCl(NO)(Py)_4]^{2+}$ metal complexes. Here we evaluate the energy gaps between the lowest singlet and triplet excited states and the corresponding state characters of the complex using density functionals from different rungs on Jacob's ladder. Besides providing a data set to assess the performance of different density functionals on excited state properties, the final goal behind this study is to identify the most appropriate functional or set of those with which eventually we will perform TD-DFT excited state molecular dynamics described in Chapter 6.[48]

5.2 Computational Section

The TD-DFT calculations were done utilising the Gaussian09 program package[49]. The geometry of trans-$[RuCl(NO)(Py)_4]^{2+}$ at the B3LYP including Grimme's dispersion correction and BP86 levels of theory, were taken from previous work, Refs. 50. The subsequent TD-DFT single point calculations[51–53] were performed using a cc-pVDZ[54;55] basis set on the hydrogens, a cc-pVTZ[56] basis set for carbon, oxygen and nitrogen. For ruthenium the Stuttgart relativistic core potential including 28 electrons was used with its associated basis set[57] and two f and one g polarization functions[58]. An ultrafine integration grid was used and no symmetry was employed. All TD-DFT calculations were performed once with and once without TDA.[59;60] The lowest four 4 singlet and 4 triplet excited states were calculated. The functionals used to calculate the excited states were one LDA (HFS[61–63]), four GGA XC functionals (PBE[64;65], BP86[66], BLYP[67–69], N12[70]), four metaGGA functionals (TPSS[71], M06-L, MN12-L[72],

SOGGA11[73]),nine Hybrid functionals (B3LYP, BHHLYP, PBE0[74;75], B971[76], B972[77], BHH[68;78], HISSbPBE[79], HSEH1PBE[80–86], N12SX[87]), four range-separatedfunctionals (CAM-B3LYP[16], wB97XD[88], LC-wPBE[89–91], M11[92]), and seven metaHybrid functionals (TPSSH[93;94], M06[23], M06-2X[23], M06HF[95;96], MN12SX[87], tHCTHhyb[97], BMK[98]).

In order to assess the performance of the XC functionals, a comparison MS-CASPT2[99–102] was done. Although MS-CASPT2 has weaknesses and one should exercise caution when using it as a reference –as it depends strongly on the choice of the active space or on the so-called IPEA shift[103;104]– for transition metal complexes of this size other accurate options, such as the algebraic diagrammatic construction method to third-order ADC(3) are not computationally feasible.[105]. On the positive side, MS-CASPT2 can deal with static and dynamic correlation for arbitrary states and regardless the spin, and is therefore expected to be more consistent than TD-DFT. For organic molecules, deviations between TD-DFT and MS-CASPT2 and experimental values can be as small as 0.3 eV[104;106;107] or slightly larger[108]. It is also noticeable that TD-DFT tends to provide less accurate values for triplets than for singlet states. Hence, since we need a one-to-one energy comparison and experimentally it is not possible to have a complete list of energies for the relevant low-lying singlet and triplet states, we resort to employ the results obtained with MS-CASPT2 as a theoretical reference. In the next section we discuss the effect of the different density functionals on the energies and state characters of trans-$[RuCl(NO)(Py)_4]^{2+}$ in comparison to the results obtained for the MS-CASPT2 in Chapter 3.

5.3 Results and discussion

5.3.1 Density Functional Dependence

In Table 5.1 we collect the spin-free vertical excitation energies and oscillator strengths of trans-$[RuCl(NO)(Py)_4]^{2+}$ obtained with MS-CASPT2(16,13), and as an example those obtained with BP86 and B3LYP using the TDA approximation. BP86 underestimates the energies more severely than B3LYP, 0.35 eV and 0.04 eV for the S_1 and 0.44 eV and 0.46 eV for the T_1, respectively compared to MS-CASPT2(16,13). For all the 29 XC functionals employed, the MSE and MAE with respect to MS-CASPT2(16,13) vertical excitation energies for the first 4 singlet and 4 triplet excited states are presented in Figures 5.1A and 5.2A without and with TDA, respectively. Regardless of TDA, the LDA and GGA XC functionals provide similar MSE and MAE values underestimating to a similar extent both the singlet and triplet energies, within 0.1 eV difference. Important is that the MSE and MAE are of the same size, indicating that the error in the excitation energies is systematic. The use of meta-variants of the GGA functionals tends to decrease the errors in the vertical transition energies, with the exception of SOGGA11. The hybrid XC functionals and their meta and range-separated counterparts show more variation in their MSE and MAE values compared to the GGA and LDA XC functionals. Nevertheless, 13 out of the 20 hybrid XC

Table 5.1 Symmetries, characters, spin-free MS-CASPT2(16,13), BP86 and B3LYP with TDA excitation energies (in eV) and oscillator strengths f of the lowest four singlet and triplet excited states of trans-$[RuCl(NO)(Py)_4]^{2+}$.

	MS-CASPT2(16,13)		BP86 TD-DFT		B3LYP TD-DFT	
State	ΔE	f	ΔE	f	ΔE	f
S_1	3.03	0.002	2.78	0.005	2.99	0.002
S_2	3.03	0.002	2.78	0.005	2.99	0.002
S_3	3.66	0.000	2.88	0.000	3.05	0.000
S_4	3.79	0.000	2.95	0.000	3.20	0.0000
T_1	2.92	–	2.48	–	2.46	–
T_2	2.93	–	2.48	–	2.68	–
T_3	3.09	–	2.56	–	2.68	–
T_4	3.11	–	2.70	–	2.72	–

functionals investigated show smaller errors for the singlet vertical transition energies than the GGA functionals, whilst several have errors on par with those observed for the GGA XC functionals. M06HF shows significantly increased errors for the singlet energies. For the triplet vertical excitation energies 12 out of the 20 hybrid XC functionals are better than GGA functionals.

Interestingly, the commonly used B3LYP functional here shows an average performance almost identical to the GGA functionals, although a detailed comparison of B3LYP with BP86 shows differences for the different states. In general, in the hybrid functionals the errors can be seen as systematic, but there are exceptions in particular functionals.

The use of TDA has a noticeable effect on the triplet states calculated using the hybrid functionals. For the LDA and GGA XC functionals one observes a minor reduction in the errors for the triplet states. For the hybrid XC functionals the errors for the triplet states is now similar or or smaller than for the GGA XC functionals. This is most notable in the case of M06HF where both the singlet and triplet state MSE and MAE are reduced by at least twofold. An important note is also that several of the functionals that showed more systematic errors without TDA now have unsystematic errors on the inclusion of TDA. An example here is MN12SX for the triplet excited states and BMK for the singlet excited states.

An initial conclusion from this data would be to use a hybrid XC functional with TDA for the calculation of the vertical excitation energies of trans-$[RuCl(NO)(Py)_4]^{2+}$. B972 for both the singlet and triplet excited states seems to be a suitable functional. The MSE and MAE for the energy gaps of the singlet and triplet excited states relative to the S_1 are shown in Figures 5.1B and 5.2B without and with TDA, respectively. The trend of GGA

Figure 5.1 Mean signed errors (MSE) and mean absolute errors (MAE) of the excitation energies (without TDA) (panel A) and the energy gaps for singlets (S) and triplet (T) states (panel B) of trans-$[RuCl(NO)(Py)_4]^{2+}$ computed against MS-CASPT2(16,13). Reprinted with permission from *J. Chem. Theory Comput*. 2017, 13, 9, 4123-4145. Copyright 2017, American Chemical Society.

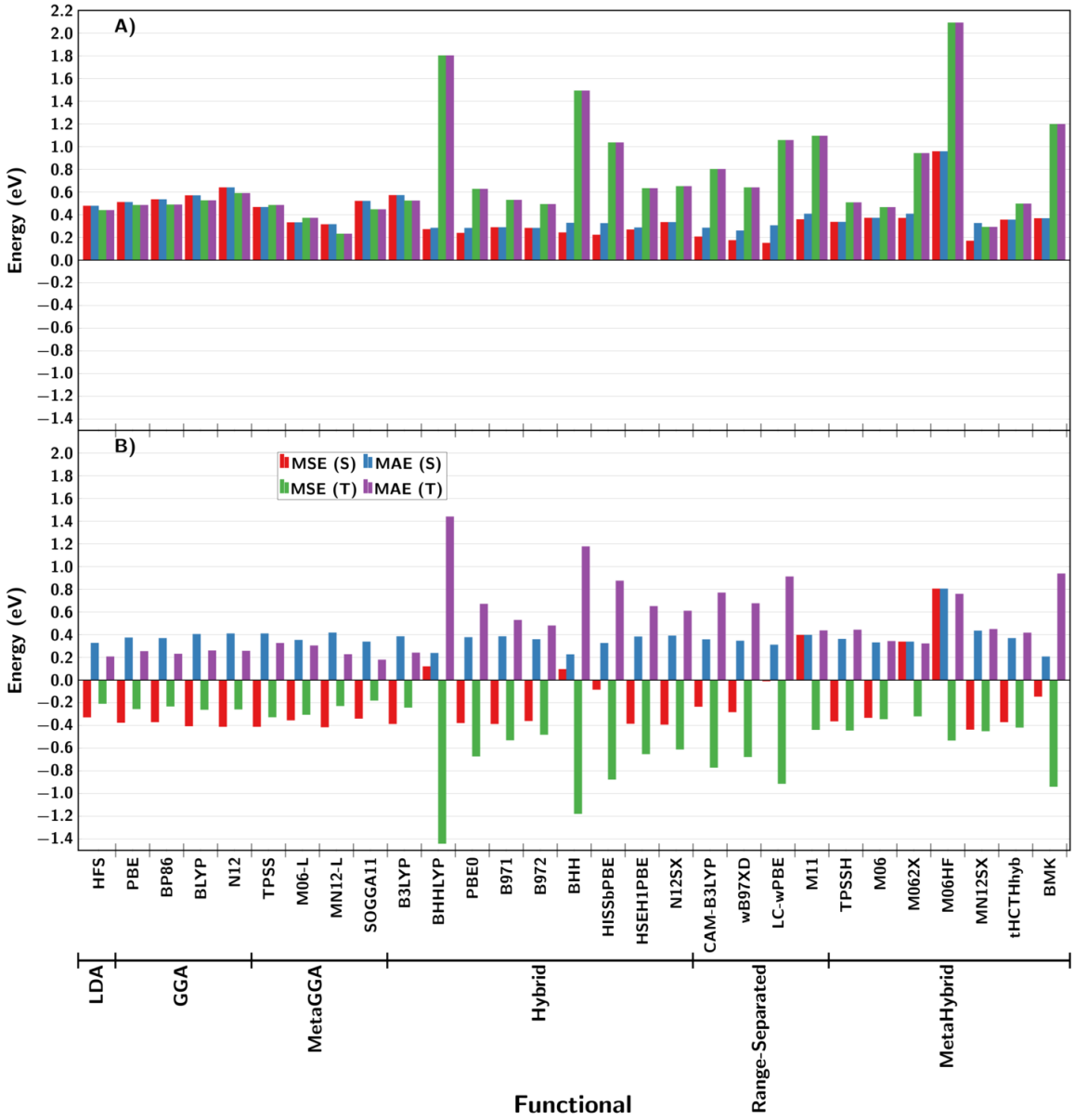

Figure 5.2 Mean signed errors (MSE) and mean absolute errors (MAE) of the excitation energies (with TDA) (panel A) and the energy gaps for singlets (S) and triplet (T) states (panel B) of trans-$[RuCl(NO)(Py)_4]^{2+}$ computed against MS-CASPT2(16,13). Note that the scale is different from that used in Figure 5.1. Reprinted with permission from *J. Chem. Theory Comput*. 2017, 13, 9, 4123-4145. Copyright 2017, American Chemical Society.

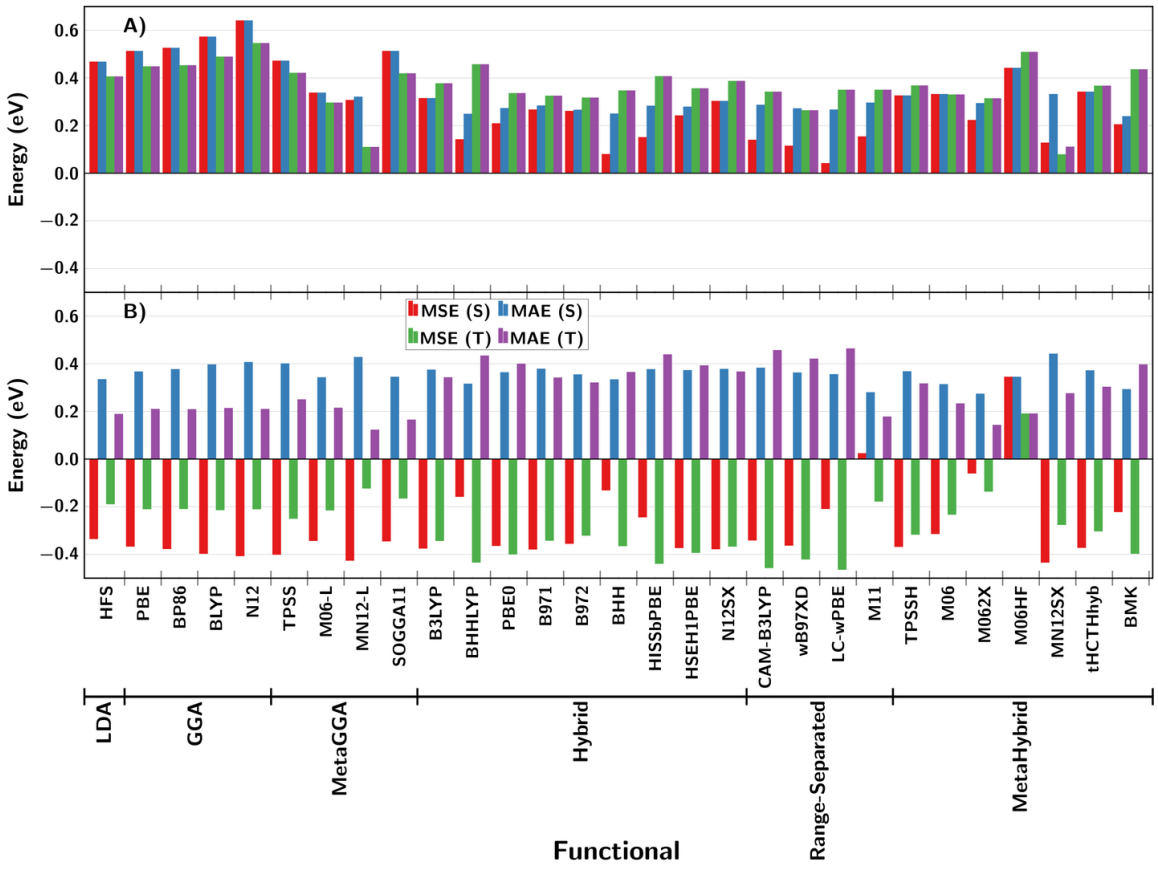

XC functionals providing better relative energies than the hybrid XC functionals when not using TDA is not so well defined. The reduction in errors going from the vertical excitation energies to the relative energies is not observed for the singlet energy gaps calculated with GGA XC functionals, although the MSE and MAE for the triplets is reduced. However, the hybrid XC functionals without TDA on average show larger errors in their energy gaps relative to the S_1 than the GGA XC functionals, specifically for the triplet energy gaps. There are a few hybrid XC functionals which provide similar MSE and MAE for the energy gaps as to the GGA XC functionals, namely B3LYP, M06 and M062X.
As observed for the vertical excitation energies, the use of TDA has a larger effect on the MSE and MAE of the hybrid XC functionals than the GGA and LDA XC functionals. Though the errors are marginally reduded for triplet energy gaps by using TDA with the GGA XC functionals, the change is negligible. However, the trend observed that the GGA XC functionals give smaller errors for the energy gaps compared to the hybrids does not hold for trans-$[RuCl(NO)(Py)_4]^{2+}$ as all the tested functionals provide similar MSE and MAE for the singlet excited states. Nonetheless, for the triplet excited states the GGA XC functionals still hold an advantage over the hybrid XC functionals, which give an MSE and MAE approximately twice that of the GGA XC functionals.
Furthermore, the errors calculated for the GGA functionals are systematic in nature, which does not hold true for all the calculated hybrid functionals. From these results, one may conclude that the use of standard GGA functionals, such as PBE or BP86, should be more suitable to describe energy gaps than the hybrid XC functionals, even though several of the hybrid XC functionals may also be suitable.

5.3.2 State Character

BP86 with TDA (BP86/TDA) as it energetically showed adequate performance, will be used to compare the performance of the other functionals. Table 5.2 lists the major orbital transitions obtained in Chapter 3 with MS-CASPT2 and BP86/TDA. The corresponding orbitals are shown in Figure 3.2 and Figure 5.3, respectively. The major character of the BP86/TDA orbitals coincides with those from MS-CASPT2 although the DFT orbitals are more delocalized with more inclusion of π orbitals from the pyridine ligands.
When comparing the character of the transitions one sees that the S_1 and S_2 of MS-CASPT2 are reproduced by BP86/TDA. Both states are composed of single transitions from the HOMO d_{xy} to the unoccupied antibonding orbitals with the NO ligand. However, larger deviations occur for the S_3 and S_4 where both have a significant contribution of the d_{xy} to the antibonding $d_{x^2-y^2}$ orbital. In general, the transitions predicted by BP86/TDA are in qualitative agreement with the MS-CASPT2 calculation, even if parts of the S_3 and S_4 states are not reproduced.

The triplet states show the same behaviour as the singlet states, with both the T_1 and T_2 of the MS-CASPT2 calculation being reproduced by BP86/TDA. Moreover, the T_3 of MS-CASPT2 corresponds to the T_3 calculated with BP86/TDA for the major contributors to the excited state. However, BP86/TDA shows more transitions mixing in and so a

Figure 5.3 Primary orbitals of trans-$[RuCl(NO)(Py)_4]^{2+}$ calculated with BP86. Reprinted with permission from *J. Chem. Theory Comput*. 2017, 13, 9, 4123-4145. Copyright 2017, American Chemical Society.

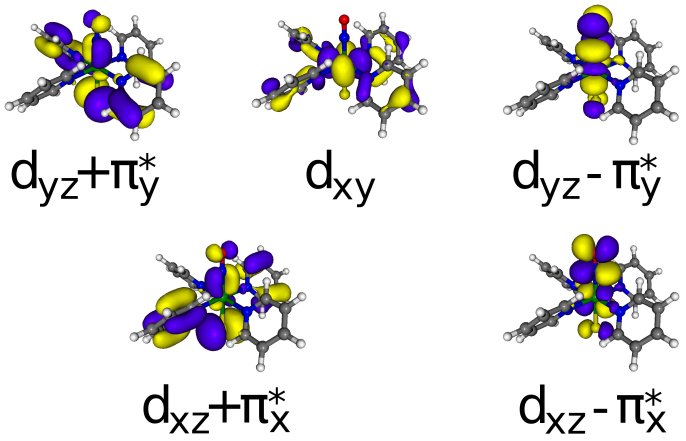

lower coefficient for the main transitions. The T_4 has no correspondence between the MS-CASPT2 and BP86/TDA calculation.

Since the BP86/TDA functional reproduces qualitatively the singlet excited states in the correct order and lowest three triplet states compared to MS-CASPT2, we take BP86/TDA as a reference to assess the performance of the other functionals in describing the excited states of trans-$[RuCl(NO)(Py)_4]^{2+}$ using the overlap between the two different wave functions. These are compared with the same technical details and including the TDA. Due to the number of functionals, only a few are selected as representatives of different functional categories (only the range-separated do not have a representative shown here). Figure 5.4 shows the wavefunction overlaps for selected functionals for trans-$[RuCl(NO)(Py)_4]^{2+}$ as well as a comparison of the effect of TDA on the wave function for BP86 and B3LYP. It is now very easy to see that PBE gives very similar state characters as BP86 with a slight mixing of the S_1 and S_2 states; the same mixing is observed for the T_1 and T_2 triplet states. These observations hold for all the GGA functionals tested here, with N12 showing stronger mixing of the two lowest excited states in both singlets and triplets.

In the case of the hybrid functional B3LYP one observes that the S_3 and S_4 have slightly different state characters than BP86/TDA. Much larger differences are present for the triplet states. Now the T_1 and T_2 have switched places with the T_3 and the T_1 and T_2 have also switched, but as with PBE the T_1 and T_2 show mixing compared to the BP86/TDA triplet states. The other hybrid functionals tested (wave function overlaps not shown) also show varying degrees of state mixing and state reordering in both the singlet and triplet states as well as completely differing state characters of the lower excited states in some cases (i.e., BHHLYP). Since the state ordering of the lowest three triplet states is reproduced well by

Table 5.2 Comparison of primary character of excitations within MS-CASPT2 and BP86 with TDA (BP86/TDA) for the lowest four singlet and triplet excitations of trans-$[RuCl(NO)(Py)_4]^{2+}$.

	State Character			
State	MS-CASPT2	Weight	BP86/TDA	Weight
S_1	$d_{xy} \rightarrow d_{yz} - \pi_y^*$	0.85	$d_{xy} \rightarrow d_{xz} - \pi_x^*$	0.99
S_2	$d_{xy} \rightarrow d_{xz} - \pi_x^*$	0.85	$d_{xy} \rightarrow d_{yz} - \pi_y^*$	0.99
S_3	$d_{xy} \rightarrow d_{x^2-y^2} - \sigma_{Py}$	0.41	$d_{xz} + \pi_x^* \rightarrow d_{yz} - \pi_y^*$	0.28
	$d_{xz} + \pi_x^* \rightarrow d_{yz} - \pi_y^*$	0.21	$d_{yz} + \pi_y^* \rightarrow d_{xz} - \pi_x^*$	0.28
	$d_{yz} + \pi_y^* \rightarrow d_{xz} - \pi_x^*$	0.17	$d_{xz} + \pi_x^* \rightarrow d_{xz} - \pi_x^*$	0.22
			$d_{yz} + \pi_y \rightarrow d_{yz} - \pi_y^*$	0.22
S_4	$d_{yz} + \pi_y^* \rightarrow d_{xz} - \pi_x^*$	0.32	$d_{xz} + \pi_x^* \rightarrow d_{xz} - \pi_x^*$	0.48
	$d_{xy} \rightarrow d_{x^2-y^2} - \sigma_{Py}$	0.31	$d_{yz} + \pi_y^* \rightarrow d_{yz} - \pi_y^*$	0.48
	$d_{xz} + \pi_x^* \rightarrow d_{yz} - \pi_y^*$	0.18		
T_1	$d_{xy} \rightarrow d_{yz} - \pi_y^*$	0.88	$d_{xy} \rightarrow d_{xz} - \pi_x^*$	0.99
T_2	$d_{xy} \rightarrow d_{xz} - \pi_x^*$	0.88	$d_{xy} \rightarrow d_{yz} - \pi_y^*$	0.99
T_3	$d_{yz} + \pi_y^* \rightarrow d_{yz} - \pi_y^*$	0.45	$d_{yz} + \pi_y \rightarrow d_{yz} - \pi_y^*$	0.22
	$d_{xz} + \pi_x^* \rightarrow d_{xz} - \pi_x^*$	0.45	$d_{xz} + \pi_x \rightarrow d_{xz} - \pi_x^*$	0.22
			$d_{yz} + \pi_y \rightarrow d_{xz} - \pi_x^*$	0.19
			$d_{xz} + \pi_x \rightarrow d_{yz} - \pi_y^*$	0.19
T_4	$d_{xy} \rightarrow d_{x^2-y^2} - \sigma_{Py}$	0.67	$d_{yz} + \pi_y \rightarrow d_{xz} - \pi_x^*$	0.42
			$d_{xz} + \pi_x \rightarrow d_{yz} - \pi_y^*$	0.42

the BP86/TDA calculation compared to the MS-CASPT2, one can conclude that the state reordering predicted by B3LYP for the triplets is incorrect.

Figure 5.4 Wave function overlap of the singlet (A) and triplet (B) states of trans-$[RuCl(NO)(Py)_4]^{2+}$ calculated using different functionals with respect to BP86/TDA. Reprinted with permission from *J. Chem. Theory Comput.* 2017, 13, 9, 4123-4145. Copyright 2017, American Chemical Society.

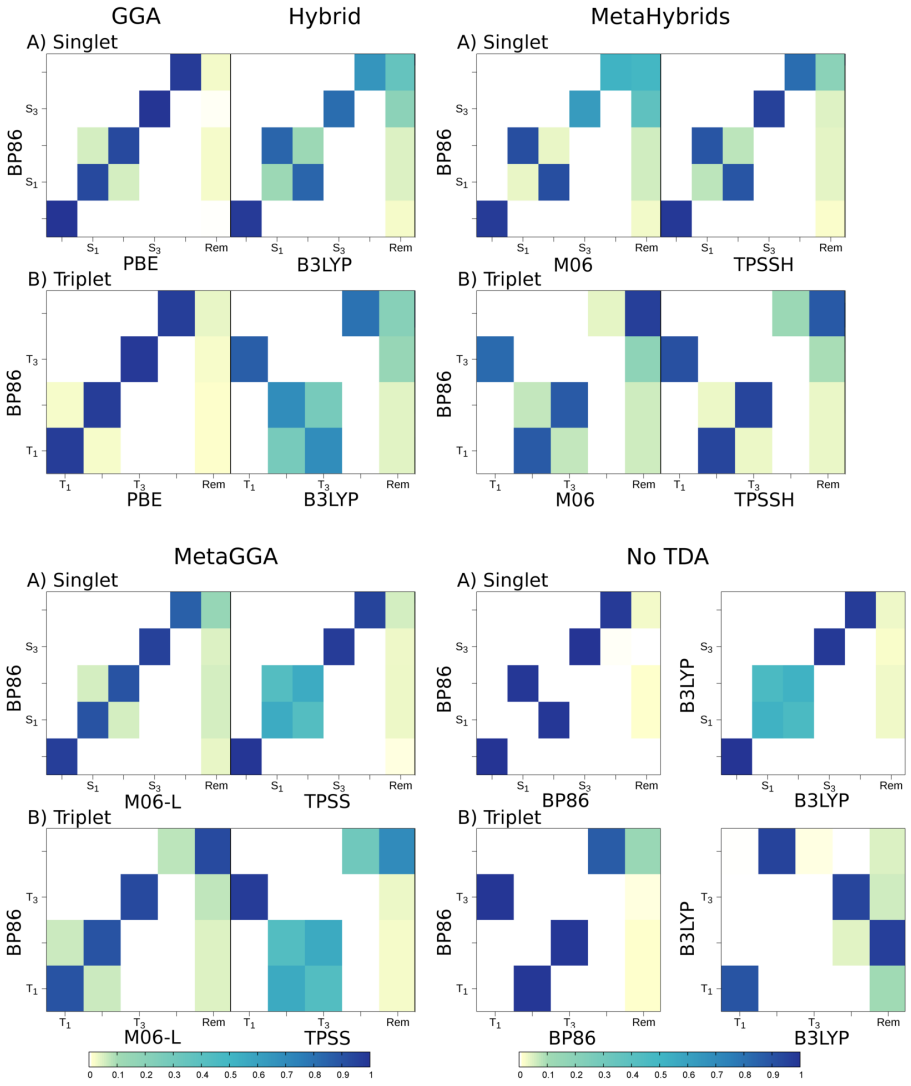

The chosen metaHybrid XC functionals (M06 and TPSSH) show the same behaviour as B3LYP for both the singlet and the triplet excited states. However, M06 shows a larger deviation of the reproduced state character of the S_3 and S_4 of the reference BP86/TDA calculation compared to B3LYP or TPSSH. For the triplet states the lowest 3 triplets have

been reordered as was the case for B3LYP and the fourth triplet state in both M06 and TPSSH for the majority does not correspond to the fourth triplet excited state calculated with BP86/TDA. Thus the same conclusion as for B3LYP must be derived.
The calculated overlaps for two metaGGA functionals (M06-L and TPSS) provide for the singlet excited states the same picture as PBE, although TPSS shows more state mixing of the S_1 and S_2 than M06-L. For the triplet states TPSS predicts an incorrect reordering of the lowest three triplet states, while M06-L reproduces the state characters of the lowest 3 triplets and as with PBE the T_1 and T_2 show some mixing. The only deviation is for the T_4 which in M06-L only retains a small margin of the state character calculated with BP86/TDA. Thus, the same conclusion as for B3LYP must be derived.
Finally, we find it interesting to consider the effect of TDA on the state characters. In the singlet excited states of BP86 the S_1 and S_2 are switched. Even larger deviations are observed for the triplet states: the T_3 is the T_1 when not using TDA and the T_1 and T_2 become the T_2 and T_3. With B3LYP, again the singlet states are mildly affected with the S_1 and S_2 being more mixed when not using TDA but the triplets are severely affected by the inclusion of TDA. The T_1 remains primarily the same but the T_2 calculated when including TDA is not present at all in the absence of TDA and the T_3 and T_4 are reordered. Thus, one can conclude that the use of TDA is highly recommended for reproducing the correct state ordering in trans-$[RuCl(NO)(Py)_4]^{2+}$, especially for the triplet excited states.

5.4 Conclusions

While in many literature benchmark studies, the performance of a TD-DFT is assessed with regards to its accuracy in the calculation of the vertical excitation energies with respect to the ground state energy, in many applications it is also required that energy gaps with respect to a state different from the ground state are also adequately described. For instance, the prediction of molecular mechanisms using nonadiabatic molecular dynamics methods is very sensitive to energy gaps between excited states, as the coupling between two (or more) states is determined by their energy gap and so nonadiabatic population transfer depends on the energy difference between the involved states. Certainly, the shape and slope of the potential energy surfaces can also influence the outcome of photodynamics simulations and in doubtful cases, it can be useful to explore the performance of different functionals to describe relaxation pathways, as e.g. done in Ref. 109. With dynamics applications in mind and since in general, the gradients of the potential energy surfaces are difficult to analyze systematically, in this chapter we have focused on the analysis of the energy gaps between the electronic excited states of the trans-$[RuCl(NO)(Py)_4]^{2+}$ and its associated wavefunction characters using different density functionals. As a reference, the results of multiconfigurational MS-CASPT2 calculation was employed. We found that the trends observed in the accuracy of the excitation energies are different from those observed for the energy gaps between excited states and therefore, the common assessment of a functional should also include a benchmark of the energy gaps. Hence, when considering excitation

energies from the electronic ground state, we found that there is not a clear distinction on the performance of the functionals. The excited state energy gaps of the singlet excited states are all described similarly with all the functionals. However, for the triplet states the GGA functionals perform predominantly better than the family of hybrid functionals. A noticeable exception is M06HF, which gives errors for the triplet state energy gaps as small as with the pure functionals.

Particular attention was put to investigate the effect of the functional on the character of the electronic wavefunction in each state. While it is possible to compare the composition of each state by examining one-by-one the determinant contributions and orbitals involved, here a more efficient procedure based on wavefunction overlaps was employed to systematically evaluate changes in the state character of the states. Since BP86 showed the best state ordering and state mixing in comparison to the multiconfigurational MS-CASPT2 reference, it was taken as a baseline to compare all other functionals. In general, we found that all pure GGA and metaGGA functionals performed similarly, while the hybrid functionals showed a significant mixing with respect to the BP86 functional. In particular, the deviations of the hybrid B3LYP are more noticeable for the higher energy singlet states with some states not described at all. The triplet states also show dramatic state reordering with B3LYP. MetaHybrids deliver the same behaviour as B3LYP for the singlet and triplet states. Assuming that the order and character predicted by MS-CASPT2 is correct, one is left to conclude pure functionals, such as BP86 or PBE or metaGGAs, such as M06-L or TPSS, might be more adequate to describe the electronic excited states of the trans-$[RuCl(NO)(Py)_4]^{2+}$system, in particular, if one is interested to calculate non-radiative properties or perform non-adiabatic dynamics. For properties that depend on vertical excitation energies, such as absorption spectra or luminescence spectra, hybrid functionals are better options for this Ru(II) complex and this should in principle hold for other Ru polypyridyl complexes. The TDA, is also recommended to use.

In Chapter 6 we will use the BP86 functional together with TDA to perform surface hopping dynamics on the trans-$[RuCl(NO)(Py)_4]^{2+}$ complex.

The results of this chapter are contained in this publication: A. J. Atkins, F. Talotta, L. Freitag, M. Boggio-Pasqua, and L. González, *J. Chem. Theory Comput.*, **2017**, 13 (9), 4123-4145, DOI: 10.1021/acs.jctc.7b00379

Bibliography

[1] C. J. Cramer and D. G. Truhlar. Density functional theory for transition metals and transition metal chemistry. *Phys. Chem. Chem. Phys.*, 11(46):10757–10816, 2009.

[2] M. Orio, D. A. Pantazis, and F. Neese. Density functional theory. *Photosynth. Res.*, 102(2-3):443–453, 2009.

[3] A. D. Laurent and Daniel. J. TD-DFT benchmarks: A review. *Int. J. Quantum Chem.*, 113(17):2019–2039, 2013.

[4] L.-N. Yun, Z.-Z. Sun, S.-L. Chen, and Z.-S. Li. The effects of various anchoring groups on optical and electronic properties of dyes in dye-sensitized solar cells. *Dyes Pigments*, 99(1):29–35, 2013.

[5] X. Shang, D. Han, Dongfeng Li, and G. Zhang. DFT/TDDFT investigation on the electronic structures and photophysical properties of phosphorescent iridium(III) complexes with 2-(pyridin-2-yl)-benzo[d]imidazole ligand. *J. Lumin.*, 147:127–133, 2014.

[6] P. J. Lestrange, P. D. Nguyen, and X. Li. Calibration of energy-specific TDDFT for modeling k-edge XAS spectra of light elements. *J. Chem. Theory Comput.*, 11:2994–2999, 2015.

[7] I.-T. Wang, T.-H.and Wang, W.-L. Huang, and L.-Y. Huang. A DFT study on structures, frontier molecular orbitals and UV–vis spectra of $RuX(PPh_3)(NHCPh_2)L$ (X = Tp and Cp; L = Cl and N_3). *Spectrochim. Acta A*, 121:650–656, 2014.

[8] S. Kupfer, M. Wächtler, J. Guthmuller, Jürgen Popp, B. Dietzek, and L. González. A novel ru(II) polypyridine black dye investigated by resonance raman spectroscopy and TDDFT calculations. *J. Phys. Chem. C*, 116(37):19968–19977, 2012.

[9] M. K. Nazeeruddin, F. De Angelis, S. Fantacci, A. Selloni, Guido Viscardi, P. Liska, Seigo Ito, Bessho Takeru, and M. Grätzel. Combined experimental and DFT-TDDFT computational study of photoelectrochemical cell ruthenium sensitizers. *J. Am. Chem. Soc.*, 127(48):16835–16847, 2005.

[10] J. P. Perdew and K. Schmidt. Jacob's ladder of density functional approximations for the exchange-correlation energy. *AIP Conf. Proc.*, 577(1):1–20, 2001.

[11] V. Krewald, F. Neese, and D. A. Pantazis. Redox potential tuning by redox-inactive cations in nature's water oxidizing catalyst and synthetic analogues. *Phys. Chem. Chem. Phys.*, 18(16):10739–10750, 2016.

[12] T. Müller. Large-scale parallel uncontracted multireference-averaged quadratic coupled cluster: The ground state of the chromium dimer revisited. *J. Phys. Chem. A*, 113(45):12729–12740, 2009.

[13] M. J. G. Peach, P. Benfield, T. Helgaker, and D. J. Tozer. Excitation energies in density functional theory: An evaluation and a diagnostic test. *J. Chem. Phys.*, 128(4):044118, 2008.

[14] J. Autschbach. Charge-transfer excitations and t.e-dependent density functional theory: Problems and some proposed solutions. *Chem. Phys. Chem.*, 10(11):1757–1760, 2009.

[15] A. Dreuw, J. L. Weisman, and M. Head-Gordon. Long-range charge-transfer excited states in time-dependent density functional theory require non-local exchange. *J. Chem. Phys.*, 119(6):2943–2946, 2003.

[16] T. Yanai, D. P. Tew, and C. H. Handy. A new hybrid exchange–correlation functional using the coulomb-attenuating method (CAM-B3LYP). *Chem. Phys. Lett.*, 393(1–3):51–57, 2004.

[17] R. van Leeuwen and E. J. Baerends. Exchange-correlation potential with correct asymptotic behavior. *Phys. Rev. A*, 49(4):2421–2431, 1994.

[18] O.V. Gritsenko, P.R.T. Schipper, and E.J. Baerends. Approximation of the exchange-correlation Kohn–Sham potential with a statistical average of different orbital model potentials. *Chem. Phys. Lett.*, 302(3–4):199–207, 1999.

[19] P. R. T. Schipper, O. V. Gritsenko, S. J. A. van Gisbergen, and E. J. Baerends. Molecular calculations of excitation energies and (hyper)polarizabilities with a statistical average of orbital model exchange-correlation potentials. *J. Chem. Phys.*, 112(3):1344–1352, 2000.

[20] M.E. Casida and M. Huix-Rotllant. Progress in t.e-dependent density-functional theory. *Annu. Rev. Phys. Chem.*, 63(1):287–323, 2012.

[21] N. T. Maitra. Perspective: Fundamental aspects of time-dependent density functional theory. *J. Chem. Phys.*, 144(22):220901, 2016.

[22] M. E. Casida, B. Natarajan, and T. Deutsch. Non-born–oppenheimer dynamics and conical intersections. In Miguel A.L. Marques, Neepa T. Maitra, Fernando M.S. Nogueira, E.K.U. Gross, and Angel Rubio, editors, *Fundamentals of Time-Dependent Density Functional Theory*, volume 837, pages 279–299. Springer Berlin Heidelberg.

[23] Y. Zhao and D. G. Truhlar. The m06 suite of density functionals for main group thermochemistry, thermochemical kinetics, noncovalent interactions, excited states, and transition elements: two new functionals and systematic testing of four m06-class functionals and 12 other functionals. *Theor. Chem. Acc.*, 120(1-3):215–241, 2008.

[24] A. Karton, A. Tarnopolsky, J.-F. Lamère, G. C. Schatz, and J. M. L. Martin. Highly accurate first-principles benchmark data sets for the parametrization and validation of density functional and other approximate methods. derivation of a robust, generally applicable, double-hybrid functional for thermochemistry and thermochemical kinetics †. *J. Phys. Chem. A*, 112(50):12868–12886, 2008.

[25] D. Jacquemin, V. Wathelet, E. A. Perpete, and C. Adamo. Extensive TD-DFT benchmark: Singlet-excited states of organic molecules. *J. Chem. Theory Comput.*, 5(9):2420–2435, 2009.

[26] E. A. Parpete. and Denis J. TD-DFT benchmark for indigoïd dyes. *J. Mol. Struc.-Theochem*, 914(1):100–105, 2009.

[27] D. Jacquemin, E.A. Parpete, I. Ciofini, and C. Adamo. Assessment of functionals for TD-DFT calculations of singlet–triplet transitions. *J. Chem. Theory Comput.*, 6(5):1532–1537, 2010.

[28] L. Martínez-Fernández, L. González, and I. Corral. Can TD-DFT predict excited states in endoperoxides? *Comp. Theor. Chem.*, 975(1–3):13–19, 2011.

[29] F. Vlahović, M. Perić, M. Gruden-Pavlović, and M. Zlatar. Assessment of TD-DFT and LF-DFT for study of *d–d* transitions in first row transition metal hexaaqua complexes. *J. Chem. Phys.*, 142(21):214111, 2015.

[30] L. Petit, C. Adamo, and N. Russo. Absorption spectra of first-row transition metal complexes of bacteriochlorins: A theoretical analysis. *J. Phys. Chem. B*, 109(24):12214–12221, 2005.

[31] L. Petit, P. Maldivi, and C. Adamo. Predictions of optical excitations in transition-metal complexes with t.e dependent-density functional theory: Influence of basis sets. *J. Chem. Theory Comput.*, 1(5):953–962, 2005.

[32] N. E. Schultz, Y. Zhao, and D. G. Truhlar. Benchmarking approximate density functional theory for s/d excitation energies in 3d transition metal cations. *J. Comput. Chem.*, 29(2):185–189, 2008.

[33] C. Garino and L. Salassa. The photochemistry of transition metal complexes using density functional theory. *Philos. T. Roy. Soc. A*, 371(1995):20120134, 2013.

[34] C. Latouche, D. Skouteris, F. Palazzetti, and V. Barone. TD-DFT benchmark on inorganic pt(II) and ir(III) complexes. *J. Chem. Theory Comput.*, 11(7):3281–3289, 2015.

[35] S. Körbel, P. Boulanger, I. Duchemin, X. Blase, M. A. L. Marques, and S. Botti. Benchmark many-body GW and bethe–salpeter calculations for small transition metal molecules. *J. Chem. Theory Comput.*, 10(9):3934–3943, 2014.

[36] A. J. Atkins, C. R. Jacob, and M. Bauer. Probing the electronic structure of substituted ferrocenes with high-resolution XANES spectroscopy. *Chem. Eur. J.*, 18(23):7021–7025, 2012.

[37] A. J. Atkins, M. Bauer, and C.toph R. Jacob. The chemical sensitivity of x-ray spectroscopy: high energy resolution XANES versus x-ray emission spectroscopy of substituted ferrocenes. *Phys. Chem. Chem. Phys.*, 15(21):8095–8105, 2013.

[38] A. J. Atkins, M. Bauer, and C.toph R. Jacob. High-resolution x-ray absorption spectroscopy of iron carbonyl complexes. *Phys. Chem. Chem. Phys.*, 17(21):13937–13948, 2015.

[39] S. DeBeer G., Taras P., and F. Neese. Prediction of iron k-edge absorption spectra using t.e-dependent density functional theory†. *J. Phys. Chem. A*, 112(50):12936–12943, 2008.

[40] M. Barbatti. Nonadiabatic dynamics with trajectory surface hopping method. *WIREs Comput. Mol. Sci.*, 1(4):620–633, 2011.

[41] M. Richter, P. Marquetand, J. González-Vázquez, I. Sola, and L. González. SHARC: *ab Initio* molecular dynamics with surface hopping in the adiabatic representation including arbitrary couplings. *J. Chem. Theory Comput.*, 7(5):1253–1258, 2011.

[42] S. Mai, P. Marquetand, and L. González. A general method to describe intersystem crossing dynamics in trajectory surface hopping. *Int. J. Quantum Chem.*, 115:1215–1231, 2015.

[43] S. K. Lower and M. A. El-Sayed. The triplet state and molecular electronic processes in organic molecules. *Chem. Rev.*, 66(2):199–241, 1966.

[44] M. A. El-Sayed. Triplet state. its radiative and nonradiative properties. *Accounts Chem. Res.*, 1(1):8–16, 1968.

[45] V. Jovanović, I. Lyskov, M. Kleinschmidt, and C. M. Marian. On the performance of DFT/MRCI-r and MR-MP2 in spin–orbit coupling calculations on diatomics and polyatomic organic molecules. *Mol. Phys.*, 115(1):109–137, 2017.

[46] F. Dinkelbach, M. Kleinschmidt, and C. M. M.n. Assessment of interstate spin–orbit couplings from l.ear response amplitudes. *J. Chem. Theory Comput.*, 13:749–766, 2017.

[47] X. Gao, S. Bai, D. Fazzi, T. Niehaus, M. Barbatti, and W. Thiel. Evaluation of spin-orbit couplings with l.ear-response t.e-dependent density functional methods. *J. Chem. Theory Comput.*, 13:515–524, 2017.

[48] F. F. de Carvalho and I. Tavernelli. Nonadiabatic dynamics with intersystem crossings: A time-dependent density functional theory implementation. *J. Chem. Phys.*, 143(22):224105, 2015.

[49] M. J. Frisch, G. W. Trucks, H. B. Schlegel, G. E. Scuseria, M. A. Robb, J. R. Cheeseman, G. Scalmani, V. Barone, B. Mennucci, G. A. P.sson, H. Nakatsuji, M. Caricato, X. Li, H. P. Hratchian, A. F. Izmaylov, J. Bloino, G. Zheng, J. L. Sonnenberg, M. Hada, M. Ehara, K. Toyota, R. Fukuda, J. Hasegawa, M. Ishida, T. Nakajima, Y. Honda, O. Kitao, H. Nakai, T. Vreven, J. A. Montgomery, Jr., J. E. Peralta, F. Ogliaro, M. Bearpark, J. J. Heyd, E. Brothers, K. N. Kudin, V. N. Staroverov, T. Keith, R. Kobayashi, J. Normand, K. Raghavachari, A. Rendell, J. C. Burant, S. S. Iyengar, J. Tomasi, M. Cossi, N. Rega, J. M. Millam, M. Klene, J. E. Knox, J. B. Cross, V. Bakken, C. Adamo, J. Jaramillo, R. Gomperts, R. E. Stratmann, O. Yazyev, A. J. Austin, R. Cammi, C. Pomelli, J. W. Ochterski, R. L. M., K. Morokuma, V. G. Zakrzewski, G. A. Voth, P. Salvador, J. J. Dannenberg, S. Dapprich, A. D. D.s, O. Farkas, J. B. Foresman, J. V. Ortiz, J. Cioslowski, , D. J. Fox, and Gaussian, Inc. Gaussian09 Revision D.01. Gaussian Inc. Wallingford CT 2013.

[50] J.S. García, F. Alary, M. Boggio-Pasqua, I. M. Dixon, I. Malfant, and J.L. Heully. Establishing the two-photon linkage isomerization mechanism in the nitrosyl complex trans-$[RuCl(NO)(py)_4]^{2+}$ by DFT and TDDFT. *Inorg. Chem.*, 54:8310–8318, 2015.

[51] C. Adamo and Denis. J. The calculations of excited-state properties with t.e-dependent density functional theory. *Chem. Soc. Rev.*, 42:845–856, 2013.

[52] F. Furche and R. Ahlrichs. Adiabatic time-dependent density functional methods for excited state properties. *J. Chem. Phys.*, 117(16):7433, 2002.

[53] R. E. Stratmann, G. E. Scuseria, and M. J. Frisch. An efficient implementation of time-dependent density-functional theory for the calculation of excitation energies of large molecules. *J. Chem. Phys.*, 109(19):8218–8224, 1998.

[54] T. H. Dunning Jr. Gaussian basis sets for use in correlated molecular calculations. i. the atoms boron through neon and hydrogen. *J. Chem. Phys.*, 90(2):1007–1023, 1989.

[55] R. A. Kendall, T. H. Dunning Jr., and R. J. Harrison. Electron affinities of the first-row atoms revisited. systematic basis sets and wave functions. *J. Chem. Phys.*, 96(9):6796–6806, 1992.

[56] D. E. Woon and T. H. Dunning Jr. Gaussian basis sets for use in correlated molecular calculations. iii. the atoms aluminum through argon. *J. Chem. Phys.*, 98(2):1358–1371, 1993.

[57] D. Andrae, U. Häussermann, M. Dolg, H. Stoll, and H. Preuß. Energy-adjusted *ab initio* pseudopotentials for the second and third row transition elements. *Theor. Chim. Acta*, 77:123, 1990.

[58] J.M.L. Martin and A. Sundermann. Correlation consistent valence basis sets for use with the stuttgart–dresden–bonn relativistic effective core potentials: The atoms Ga–Kr and In–Xe. *J. Chem. Phys.*, 114:3408, 2001.

[59] S. Hirata and M. Head-Gordon. Time-dependent density functional theory within the tamm-dancoff approximation. *Chem. Phys. Lett.*, 314(3):291–299, 1999.

[60] S. Hirata and M. Head-Gordon. Time-dependent density functional theory for radicals: An improved description of excited states with substantial double excitation character. *Chem. Phys. Lett.*, 302(5–6):375–382, 1999.

[61] P. Hohenberg and W. Kohn. Inhomogeneous electron gas. *Phys. Rev.*, 136:B864–B871, 1964.

[62] W. Kohn and L. J. Sham. Self-consistent equations including exchange and correlation effects. *Phys. Rev.*, 140:A1133–A1138, 1965.

[63] J. C. Slater. *The Self-Consistent Field for Molecular and Solids, Quantum Theory of Molecular and Solids*, volume 4. McGraw-Hill, 1974.

[64] J. P. Perdew, Kieron Burke, and M. Ernzerhof. Generalized gradient approximation made simple. *Phys. Rev. Lett.*, 77(18):3865–3868, 1996.

[65] J. P. Perdew, K. Burke, and M. Ernzerhof. Generalized gradient approximation made simple [phys. rev. lett. 77, 3865 (1996)]. *Phys. Rev. Lett.*, 78:1396–1396, 1997.

[66] J. P. Perdew. Density-functional approximation for the correlation energy of the inhomogeneous electron gas. *Phys. Rev. B*, 33(12):8822–8824, 1986.

[67] A. D. Becke. Density-functional exchange-energy approximation with correct asymptotic behavior. *Phys. Rev. A*, 38(6):3098–3100, 1988.

[68] C. Lee, W. Y.g, and R. G. Parr. Development of the colle-salvetti correlation-energy formula into a functional of the electron density. *Phys. Rev. B*, 37(2):785–789, 1988.

[69] T. V. Russo, R.L. Martin, and P.J. Hay. Density functional calculations on first–row transition metals. *J. Chem. Phys.*, 101(9):7729–7737, 1994.

[70] R. Peverati and D. G. Truhlar. Exchange-correlation functional with good accuracy for both structural and energetic properties while depending only on the density and its gradient. *J. Chem. Theory Comput.*, 8(7):2310–2319, 2012.

[71] J. Tao, J. P. Perdew, V. N. Staroverov, and G. E. Scuseria. Climbing the density functional ladder: Nonempirical Meta–Generalized gradient approximation designed for molecules and solids. *Phys. Rev. Lett.*, 91(14):146401, 2003.

[72] R. Peverati and D. G. Truhlar. An improved and broadly accurate local approximation to the exchange-correlation density functional: The MN12-L functional for electronic structure calculations in chemistry and physics. *Phys. Chem. Chem. Phys.*, 14:13171–13174, 2012.

[73] R. Peverati, Y. Zhao, and D. G. Truhlar. Generalized gradient approximation that recovers the second-order density-gradient expansion with optimized across-the-board performance. *J. Phys. Chem. Lett.*, 2:1991–1997, 2011.

[74] M. Ernzerhof and G. E. Scuseria. Assessment of the Perdew–Burke–Ernzerhof exchange-correlation functional. *J. Chem. Phys.*, 110(11):5029–5036, 1999.

[75] C. Adamo and V. Barone. Toward reliable density functional methods without adjustable parameters: The PBE0 model. *J. Chem. Phys.*, 110(13):6158–6170, 1999.

[76] F. A. Hamprecht, A. J. Cohen, D. J. T., and N. C. Handy. Development and assessment of new exchange-correlation functionals. *J. Chem. Phys.*, 109(15):6264–6271, 1998.

[77] P. J. Wilson, T. J. Bradley, and D. J. Tozer. Hybrid exchange-correlation functional determined from thermochemical data and ab initio potentials. *J. Chem. Phys.*, 115(20):9233–9242, 2001.

[78] A. D. Becke. A new mixing of hartree-fock and local density-functional theories. *J. Chem. Phys.*, 98(2):1372–1377, 1993.

[79] T. M. Henderson, A. F. Izmaylov, G. E. Scuseria, and A. Savin. Assessment of a middle-range hybrid functional. *J. Chem. Theory Comput.*, 4(8):1254–1262, 2008.

[80] J. Heyd and G. E. Scuseria. Efficient hybrid density functional calculations in solids: Assessment of the heyd-scuseria-ernzerhof screened coulomb hybrid functional. *J. Chem. Phys.*, 121(3):1187–1192, 2004.

[81] J. Heyd and G. E. Scuseria. Assessment and validation of a screened coulomb hybrid density functional. *J. Chem. Phys.*, 120(16):7274–7280, 2004.

[82] J. Heyd, J. E. Peralta, G. E. Scuseria, and R. L. M. Energy band gaps and lattice parameters evaluated with the heyd-scuseria-ernzerhof screened hybrid functional. *J. Chem. Phys.*, 123(17):174101, 2005.

[83] J. Heyd, G. E. Scuseria, and M. Ernzerhof. Erratum: Hybrid functionals based on a screened coulomb potential [j. chem. phys. 118, 8207 (2003)]. *J. Chem. Phys.*, 124(21):219906, 2006.

[84] G. M. Henderson, A. F. Izmaylov, G. Scalmani, and G. E. Scuseria. Can short-range hybrids describe long-range-dependent properties? *J. Chem. Phys.*, 131(4):044108, 2009.

[85] A. F. Izmaylov, G. E. Scuseria, and M. J. Frisch. Efficient evaluation of short-range hartree-fock exchange in large molecules and periodic systems. *J. Chem. Phys.*, 125(10):104103, 2006.

[86] A. V. Krukau, O. A. Vydrov, A. F. Izmaylov, and G. E. Scuseria. Influence of the exchange screening parameter on the performance of screened hybrid functionals. *J. Chem. Phys.*, 125(22):224106, 2006.

[87] R. Peverati and D. G. Truhlar. Screened-exchange density functionals with broad accuracy for chemistry and solid-state physics. *Phys. Chem. Chem. Phys.*, 14:16187–16191, 2012.

[88] J.-D. Chai and M. Head-Gordon. Long-range corrected hybrid density functionals with damped atom-atom dispersion corrections. *Phys. Chem. Chem. Phys.*, 10:6615–6620, 2008.

[89] O. A. Vydrov and G. E. Scuseria. Assessment of a long-range corrected hybrid functional. *J. Chem. Phys.*, 125(23):234109, 2006.

[90] T. Vreven, M. J. Frisch, K. N. Kudin, H. B. Schlegel, and K. Morokuma. Geometry optimization with QM/MM methods II: Explicit quadratic coupling. *Mol. Phys.*, 104(5-7):701–714, 2006.

[91] O. A. Vydrov, G. E. Scuseria, and J. P. Perdew. Tests of functionals for systems with fractional electron number. *J. Chem. Phys.*, 126(15):154109, 2007.

[92] R. Peverati and D. G. Truhlar. Improving the accuracy of hybrid meta-gga density functionals by range separation. *J. Phys. Chem. Lett.*, 2(21):2810–2817, 2011.

[93] V. N. Staroverov, G. E. Scuseria, J. Tao, and J. P. Perdew. Comparative assessment of a new nonempirical density functional: Molecules and hydrogen-bonded complexes. *J. Chem. Phys.*, 119(23):12129–12137, 2003.

[94] V. N. S., G. E. Scuseria, J. Tao, and J. P. Perdew. Erratum: Comparative assessment of a new nonempirical density functional: Molecules and hydrogen-bonded complexes [j. chem. phys. 119, 12129 (2003)]. *J. Chem. Phys.*, 121(22):11507–11507, 2004.

[95] Y. Zhao and D. G. Truhlar. Comparative dft study of van der waals complexes: Rare-gas dimers, alkaline-earth dimers, zinc dimer, and zinc-rare-gas dimers. *J. Phys. Chem. A*, 110(15):5121–5129, 2006.

[96] Y. Zhao and D. G. Truhlar. Density functional for spectroscopy: No long-range self-interaction error, good performance for rydberg and charge-transfer states, and better performance on average than b3lyp for ground states. *J. Phys. Chem. A*, 110(49):13126–13130, 2006.

[97] A. D. Boese and N. C. Handy. New exchange-correlation density functionals: The role of the kinetic-energy density. *J. Chem. Phys.*, 116(22):9559–9569, 2002.

[98] A. D. Boese and J.M.L. Martin. Development of density functionals for thermochemical kinetics. *J. Chem. Phys.*, 121(8):3405–3416, 2004.

[99] K. Andersson, P. A. Malmqvist, B. O. Roos, A. J. Sadlej, and K. Wolinski. Second-order perturbation theory with a CASSCF reference function. *J. Phys. Chem.*, 94(14):5483–5488, 1990.

[100] K. Andersson, P. Malmqvist, and B. O. Roos. Second-order perturbation theory with a complete active space self-consistent field reference function. *J. Chem. Phys.*, 96(2):1218–1226, 1992.

[101] S. Finley, P. Malmqvist, B. O. Roos, and L. Serrano-Andrés. The multi-state CASPT2 method. *Chem. Phys. Lett.*, 288(2):299–306, 1998.

[102] F. Aquilante, P. Malmqvist, T. B. Pedersen, A. Ghosh, and B. O. Roos. Cholesky Decomposition-Based Multiconfiguration Second-Order Perturbation Theory (CD-CASPT2): Application to the Spin-State Energetics of CoIII(diiminato)(NPh). *J. Chem. Theory Comput.*, 4(5):694–702, 2008.

[103] G. Ghigo, B. O. Roos, and P. Malmqvist. A modified definition of the zeroth-order hamiltonian in multiconfigurational perturbation theory (CASPT2). *Chem. Phys. Lett.*, 396(1):142–149, 2004.

[104] J. P. Zobel, J. J. Nogueira, and L. González. The IPEA dilemma in CASPT2. *Chem. Sci.*, 8(2):1482–1499, 2017.

[105] F. Plasser and A. Dreuw. High-level ab initio computations of the absorption spectra of organic iridium complexes. *J. Phys. Chem. A*, 119(6):1023–1036, 2015.

[106] M. Schreiber, M. R. Silva-Junior, S. P. A. Sauer, and W. Thiel. Benchmarks for electronically excited states: CASPT2, CC2, CCSD, and CC3. *J. Chem. Phys.*, 128(13):134110, 2008.

[107] M. R. Silva-Junior, M. Schreiber, S. P. A. Sauer, and W. Thiel. Benchmarks for electronically excited states: T.e-dependent density functional theory and density functional theory based multireference configuration interaction. *J. Chem. Phys.*, 129(10):104103, 2008.

[108] C. E. Hoyer, S. Ghosh, D. G. Truhlar, and L. Gagliardi. Multiconfiguration pair-density functional theory is as accurate as CASPT2 for electronic excitation. *J. Phys. Chem. Lett.*, 7(3):586–591, 2016.

[109] O. Valsson, C. Filippi, and M. E. Casida. Regarding the use and misuse of retinal protonated schiff base photochemistry as a test case for time-dependent density-functional theory. *J. Chem. Phys.*, 142(14):144104, 2015.

Chapter 6

Non-adiabatic Study

This chapter presents the results of the excited state dynamics simulation of the trans-$[RuCl(NO)(Py)_4]^{2+}$photochromic system. The outcome of this study are in line with the hypotheses formulated in Chapter 3. Using non-adiabatic excited state dynamics in gas phase, we investigate the role of the singlet and triplet excited states in the isomerization mechanism, establish the branching ratio between different pathways. The considerably long simulation time of the dynamics simulations achieved thanks to improvements of the SHARC/ADF procedure described in Chapter 2, allowed to identify slow quenching funnels that take place after 200 fs and make the NO photoisomerization process less efficient.

6.1 Motivation

The CASPT2 study presented in Chapter 3 represent a major breakthrough in the understanding of the mechanism behind the photoisomerization of the trans-$[RuCl(NO)(Py)_4]^{2+}$nitrosyl complex. However, the static picture outlined by the electronic structure calculations cannot provide more insight about the photodynamics of the system. In this context, the surface hopping dynamic simulations[1;2] represent a useful computational tool for a better understand the photochemistry of this system, especially when facing such a complex mechanistic picture with many accessible pathways. In the past years, the surface-hopping dynamics including arbitrary coupling (SHARC)[2–5] procedure described in Chapter 2 has been used to a large extent in the investigation of the photochemistry of small organic molecules[6–11]. Moreover, those simulations included the proper description of the non-adiabatic dynamic effects and internal conversions between the electronic states. Recently, the SHARC procedure has been successfully applied to uncover the photodynamics of a similar ruthenium complex.[12] However, despite the good results obtained, this study remains the only attempt of dynamics simulations on such ruthenium complexes and furthermore there are no studies on such photodynamics of

ruthenium nitrosyl molecules with the proper description of the non adiabatic effects. To a large extent, this is due to the high computational cost of the simulations, but also to the difficult seeking of a fast and reliable quantum mechanical method capable of accurately describing the electronic structure of the system at a reasonable cost. For these reasons the propagation time for such ruthenium nitrosyl molecules has been always limited to no more than 50 fs.[12;13] The new improvements of the ADF code carried out during the secondment at SCM described in Chapter 2 allowed to extend the simulation time up to 1 ps.
In the present chapter we report the full dimensional surface hopping dynamics on the trans-$[RuCl(NO)(Py)_4]^{2+}$ruthenium nitrosyl complex including non adiabatic effects. Our aim is to investigate the role of the singlet and triplet excited states for the first part of the isomerization mechanism (from **GS** to **MS2**), by establishing the branching ratio between the different pathways, and identifying the most important quenching funnels that make the entire N→O isomerization process less efficient. The trajectories will describe three distinct photoisomerization pathways: two of them (pathway **I** and pathway **II**) have been introduced in Chapter 3 (see Section 3.6), whereas a third one (called pathway **III**) is a new unprecedented mechanism.

6.2 Computational Details

The dynamics simulations were performed with our in-house software `SHARC 1.0`. Due to the large size of the system we decided to use TDDFT for the on-the-fly calculation of the electronic properties. The computation of the energies, gradients and spin-orbit couplings, have been entrusted to a new version of the `ADF` program package[14], accurately optimized for the SHARC procedure (see Chapter 2). All the DFT and TDDFT calculations have been performed with BP86.[15;16] This functional has been widely used for TM complexes,[17–20] and furthermore it has been proven in Chapter 5 to be the best choice for this particular ruthenium complex, although there still exist some import differences between the BP86 PES and the MS-CASPT2 ones of Chapter 3, as already mentioned in Chapter 5. The TZ2P basis set has been used on the Ru, N, O and Cl atoms, whereas the TZP set has been used on the C, and H atoms. Non-adiabatic couplings were obtained using the wavefunction overlaps.[21] The DFT/TD-DFT calculations with ADF have been performed with a `Density ZlmFit` and a `BeckeGrid` set to `Normal`. The Coupled Perturbed Kohn-Sham (CPKS) equations convergence threshold[22–25] for the excited state gradients has been set to 0.0001. The number of Davidson vectors has been set to 60, whereas the convergence tolerance has been set to 10^{-6}. The trajectories have been propagated with a simulation time step of 0.5 fs and a total simulation time of 1000 fs. The number of substeps was set to 25. As decoherence, the Granucci-Persico-Zoccante scheme was used[26]. As hopping scheme, the "Standard SHARC surface hopping probabilities" scheme has been used.
To characterize the excited states at each time step we used the TheoDORE program package[27–31], which provides an accurate and objective assessment for the charge transfers

observed in such transition metal complexes (MLCT, LMCT, LLCT, etc) by looking at properties based on of the one-electron transition density matrix (1TDM). The charge transfer numbers have been computed using the Löwdin formula.
According to the available experimental data, at the FC geometry **GS** only the bright states S_1/S_2 are populated by the blue light[32;33]. Initially, these two states must be equally populated as they form a Jahn-Teller degeneracy. In addition, the BP86 and MS-CASPT2 potential state energies listed in Table 5.1 show that the photoisomerization mechanism should develop just on the three lowest singlet states (S_0, S_1, S_2) and the three lowest triplet states (T_1, T_2, T_3). Accordingly, the trajectories have been prepared initially in the pair of states S_1/S_2 and then propagated on the six states S_0, S_1, S_2, T_1, T_2, T_3.

6.3 Results and Discussion

6.3.1 The Absorption Spectrum of the GS Isomer

Figure 6.1 shows the Wigner sampled[34–36] absorption spectra for the two degenerate MLCT states, S_1 and S_2. Because of this degeneracy, the two absorption bands appear almost identical in terms of energies and oscillator strengths.

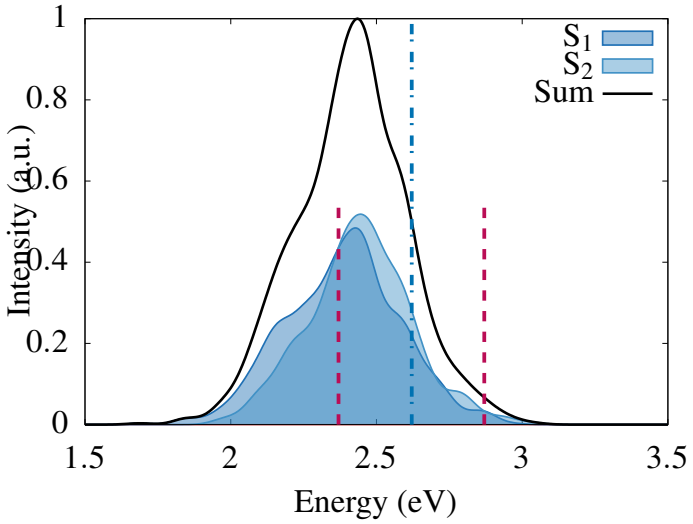

Figure 6.1 TD-BP86 convoluted absorption spectra of the trans-$[RuCl(NO)(Py)_4]^{2+}$ molecule from the first two excited states S_1 and S_2, obtained from a Wigner distribution of **GS** including 500 initial geometries. The vertical blue dashed line represents the experimental excitation energy of 2.61 eV (473 nm) and the red dashed lines delimit the energy window of ±0.25 eV centered at 2.61 eV, from which initial geometries and velocities were taken to propagate the SHARC trajectories.

The overall spectrum displays a small red-shift of 0.2 eV compared to the energy of

2.61 eV used by the experimentalists. This red-shift is common with GGA functionals which tend to underestimate the energies of CT states.[13;37] Note also that the wavelength used experimentally is tuned to optimize the photoconverison efficiency, and thus does not correspond necessarily to the maximum of the $S_0 \rightarrow S_1/S_2$ absorption band. For the selection of the initial conditions, an energy window of ± 0.25 eV has been considered, in order to mimic the broad character of the light used in the experiments and to take into account the inaccuracy in the BP86 excited energies. In this energy window, the SHARC procedure[38] selected 144 trajectories, of which 74 are on the S_1 state and 70 on the S_2 state. From them, 47 trajectories (33%) propagated during 1 ps. These trajectories will pertain pathway **I**. The remaining 97 trajectories (67%) stopped within the first 200 fs, i.e. as soon as they reached the zone near **TS1** where the S_0 and S_1 get close in energy –a situation that TD-DFT cannot handle– and the calculation is terminated. This breakdown of DFT was expected to some extent because, as already mentioned above in Chapter 3, some of envisaged pathways ought to visit the zone near **TS1** (see Figure 3.8 and Section 3.6), where the S_0 and S_1 get close in energy.

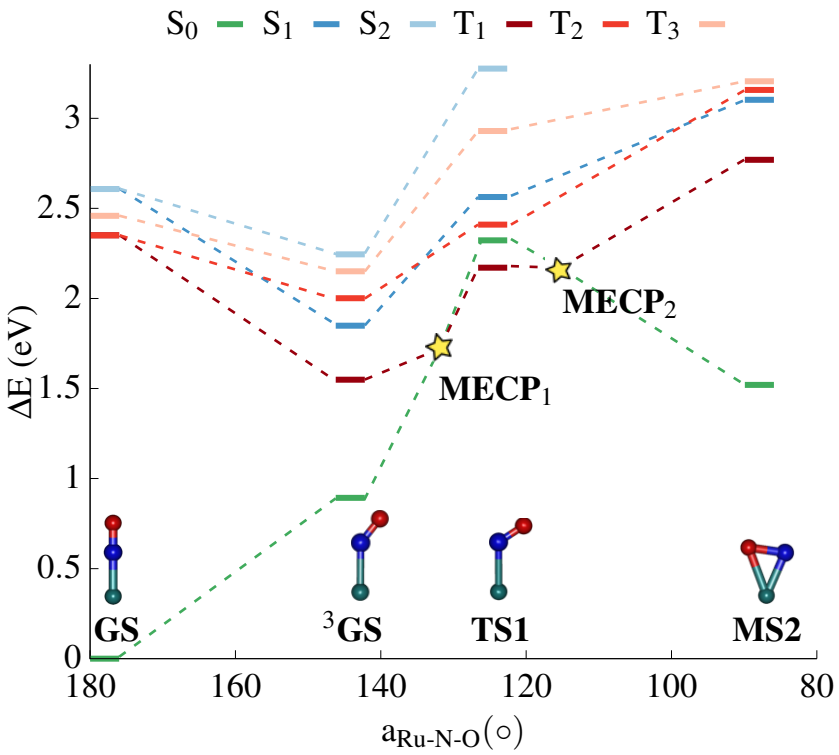

Figure 6.2 DFT and TD-DFT energy correlation diagram for the first three singlet (blue lines) and three triplet states (red lines), according to BP86. The thick solid lines represent the vertical energies at the corresponding geometry, whereas the dashed lines link the states together. All the geometries have been optimized in their ground state S_0, except for the ^{3}**GS** geometry that has been optimized using the TD-DFT gradients on the lowest triplet excited state T_1. Corresponding geometrical parameters and energies are listed in Table 6.1

Geom	$r_{Ru\text{-}N}$ (Å)	$r_{Ru\text{-}O}$ (Å)	$r_{N\text{-}O}$ (Å)	$a_{Ru\text{-}N\text{-}O}$ (∘)	ΔE (eV)
GS	1.765	2.925	1.158	180.0	0.00 (S_0)
^{3}**GS**	1.893	2.910	1.178	141.7	1.55 (T_1)
MECP$_1$	1.953	2.879	1.180	131.9	1.72 (S_0/T_1)
TS1	2.001	2.812	1.163	122.6	2.32 (S_0)
MECP$_2$	2.000	2.719	1.172	115.3	2.17 (S_0/T_1)
MS2	1.934	2.202	1.201	85.9	1.52 (S_0)

Table 6.1 Geometrical parameters and energies (related state in round bracket) for the critical points involved in the **GS** to **MS2** photoisomerization. The $MECP_1$ and $MECP_2$ between S_0 and T_1 have been optimized using the ORCA 4.0 optimiser and the DFT (for S_0) and TD-DFT (for T_1) gradients provided by ADF. The ^{3}**GS** geometry has been optimised using the TD-DFT gradients on the lowest triplet excited state T_1.

These two states get close in energy also in BP86 as shown in Figure 6.2. Therefore although shorter, such trajectories own very meaningful information about the nonradiative deactivation processes. The trajectories that halted in a singlet state will pertain pathway **II** whereas the trajectories that halted on a triplet state will pertain pathway **III**.

6.3.2 Excited-State Dynamics of Pathway I

Figure 6.3 **(A)** presents the temporal evolution of the classical population ensemble for the subset of trajectories that reached 1 ps (pathway **I**). The population data has been fitted and bootstrapped[39] in order to get an estimation of the time constants associated to the various population transfers. Initially the singlet excited states S_1 and S_2 are equally populated (∼50%), but within few fs, a series of ISCs induce a readily depopulation of S_1 and S_2 towards the triplet states. This leads to an inversion of population between singlets and triplets at ∼100 fs, as shown in the inset of Figure 6.3 **(A)**. The fitting procedure estimates a time constant of 160 ± 30 fs for this process, corresponding to ∼750 fs to get a triplet yield of 99%. This can be considered an ultrafast ISC, although less efficient than measured and calculated in other transition metal complexes.[12;13;40–42]. A closer look at the individual state populations reveals that the moderate decay rate of the singlets is essentially due to a slow depopulation of the S_1 state. For instance, within 300 fs the population of S_2 drops to 2% whereas S_1 still remains substantially populated (∼15%). At the same time, the net hopping event analysis in Table 6.2 between each pair of states reveals that S_2 relaxes towards the T_3 state (17 hops), whereas S_1 relaxes towards the T_2 state (26 hops). Accordingly, the non adiabatic transition $S_2 \rightarrow T_3$ results to be more efficient than the one from S_1 to T_2. This large difference between the two pair of states can be explained by looking at the magnitude of the spin-orbit interaction between the excited states. The spin-orbit values at FC region are listed in Table 6.3. Near the FC region, the S_2/T_3 pair

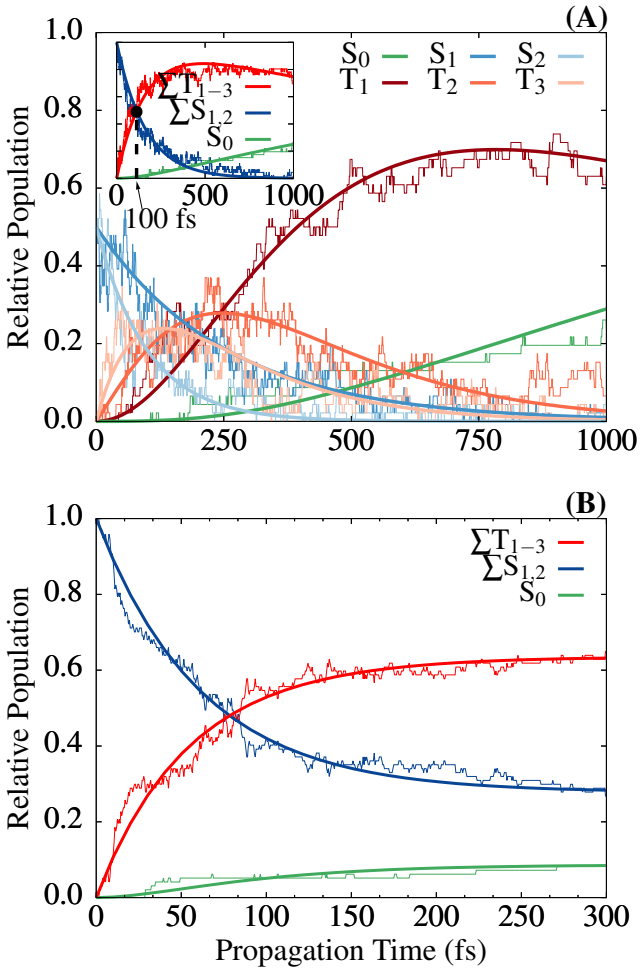

Figure 6.3
(A): Time evolution of the state populations of the electronic ground and excited states of trans-$[RuCl(NO)(Py)_4]^{2+}$for the trajectories that reached 1 ps. The inset shows the population of the S_0 state, as well as the population of S_1 and S_2 combined together as $\sum S_{1,2}$, and T_1, T_2 and T_3 combined together as $\sum T_{1-3}$.
(B): Population of the S_0 state, as well as the population of S_1 and S_2 combined together as $\sum S_{1,2}$, and T_1, T_2 and T_3 combined together as $\sum T_{1-3}$ for the trajectories that reached 200 fs.
Thick lines show the fitted functions on top of the corresponding raw population data.

shows a SOC of $\sim$100 cm^{-1}, whereas S_1 and T_2 shows a weaker SOC of $\sim$40 cm^{-1}. The 1TDM analysis of the excited states at the FC region in Figure 6.4, shows that the smaller value of the SOC between S_1 and T_2 is compatible with the El-Sayed rule,[43] in the sense that S_1 and T_2 share the same character in their electronic transitions, whereas T_3 owns a complete different character from S_1 or S_2. Upon relaxation to T_3, the system continues to deactivate nonradiatively towards T_2, and eventually T_2 decays to T_1. These initial findings are in reasonable agreement with the general mechanism of pathway **I**,

	S_0	S_1	S_2	T_1	T_2	T_3	Sum
S_0	0	0	0	12	-1	0	11
S_1	0	0	3	1	-26	-1	-23
S_2	0	-3	0	-1	0	-17	-21
T_1	-12	-1	1	0	43	-2	29
T_2	1	26	0	-43	0	19	3
T_3	0	1	17	2	-19	0	1

Table 6.2 Number of net hopping events between each active electronic state for the trajectories that reached 1 ps.

State	T_1	T_2	T_3
S_0	287	287	287
S_1	280	39	100
S_2	39	280	100

Table 6.3 Spin-orbit coupling values in cm^{-1} at the N-bonded isomer **GS**.

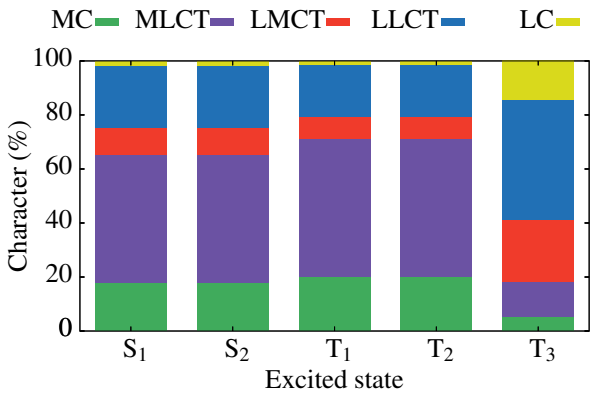

Figure 6.4 Decomposition of the charge transfer numbers at the **GS** geometry, for the excited states taken into account in the SHARC dynamics. Note the different decomposition of T_3 with respect to the other excited states.

predicted by the stationary DFT[44] and MS-CASPT2 calculations described in Chapter 3, and underline the role played by the ISC and triplet states in the NO photoisomerization of trans-$[RuCl(NO)(Py)_4]^{2+}$.

To get more insight into the dynamics of this subset of trajectories, we analysed the geometrical changes induced by the various relaxation processes discussed above. For such N→O linkage isomerization, the most important internal coordinates to track are

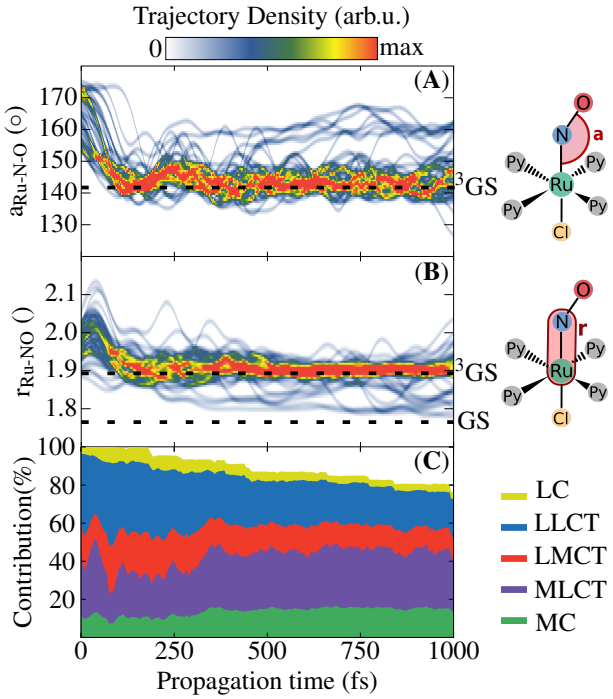

Figure 6.5 Time-dependent distribution of the Ru-N-O angle (**A**) and Ru-NO bond distance (**B**) for the 47 trajectories related to pathway **I**. The Ru-N-O data has been smoothed out with a Gaussian smoothing kernel, applied at intervals equal to the Ru-N-O vibrational period of 64 fs. Similarly, the Ru-NO data has been smoothed out with a period of 80 fs. The two set of data have been convoluted later, using a Gaussian convolution kernel. Panel (**C**) shows the time evaluation of the state character (IL, LLCT, LMCT, MLCT, and MC) as a staked population, calculated from the charge transfer number decomposition, averaged over all the states of the 47 trajectories.

the Ru-N-O angle and Ru-NO bond distance, here shown in Figure 6.5 (**A**) and (**B**) as a convoluted distribution of the trajectories ensemble. In the early part of the propagation, the geometries undergo a coherent bending of the nitrosyl ligand from almost linear Ru-N-O configuration of **GS** isomer to ca. 142° in about 160 fs. The TheoDORE analysis of the excited states character in Figure 6.5 (**C**) reveals the interesting correlation between the Ru-N-O bending and the increase of the MLCT character, in the picture noticeable by a peak of the MLCT band within the first around 80 fs. This correlation has already been found in other nitrosyl complexes.[13;45;46] The eventual angle of 142° is consistent with the Ru-N-O bending angle of the ^{3}**GS** isomer, de facto the nearest reachable minimum along the N→O isomerization pathway (see Table 6.1 & Figure 6.2). Meanwhile, the Ru-NO bond distance undergoes a notable elongation, increasing from ca. 1.76 Å (the value of **GS** isomer) to ca. 2.20 Å in the time interval between 0 and 60 fs. Again, the elongation of this bond can be related to the increasing MLCT character of the excited states. Within 160 fs this distance gets stabilised to a value of ca. 1.90 Å, consistent with the Ru-NO bond length of ^{3}**GS**. Accordingly, from a structural point of view, all trajectories reach the minimum ^{3}**GS** in 160 fs, albeit such short time range is not enough for most trajectories

to relax to the lowest triplet state T_1. The singlet S_1 is still substantially populated at this stage. Interestingly, the TD-DFT single point calculations reveal that ^{3}**GS** also doubles as a minimum for S_1. Therefore, it is not surprising to see some trajectories remaining in S_1 for some time, considering also the weak SOC between S_1 and its nearest triplet state T_2. Upon relaxation to ^{3}**GS**, most trajectories fluctuate in this energy well till the end of the propagation time, as shown by the thickening of the ensemble in Figure 6.5 (**A**) and (**B**) around the ^{3}**GS** equilibrium values. However few other trajectories deviate from this minimum and relax back to the original Frank-Condon geometry **GS** through ISC between T_1 and S_0. A closer look to the internal coordinates of the $T_1 \rightarrow S_0$ hopping geometries in Figure 6.6 revels that the ISCs occur near **MECP**$_1$, located between the ^{3}**GS** and **MS2**,

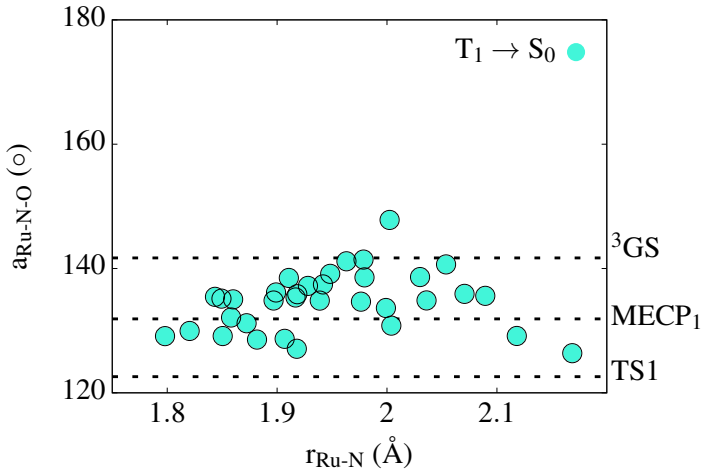

Figure 6.6 Geometrical parameters for the hopping geometries $T_1 \rightarrow S_0$.

0.17 eV higher in energy than ^{3}**GS** as shown in & Table 6.1. The trace of such hoppings can be seen in Figure 6.3 by the growth of the ground state S_0 population starting from 250 fs and the downturn of the T_1 population noticeable after 750 fs. Alternatively, such hoppings can be observed in Figure 6.5 (**C**) through the norm depletion of the 1TDM. The net hops analysis confirms that the T_1 depletion is directly related to the occurrence of the crossings near **MECP**$_1$. This relaxation pathway represents a major quenching funnel that could make the entire photoisomerization process quite inefficient, since it takes the system back to the starting point. However, the large time constant of 1600$\pm$600 fs associated to this process, reveals the inefficiency of such ISCs compared to the shorter time scales observed before. For instance, in our simulations, out of 144 trajectories just 8 (5%) undergo $T_1 \rightarrow S_0$ ISC within 1 ps.

The major dynamics events related to pathway **I** are summarized in the right part of Figure 6.8 right. The overall behaviour agrees with the general photoisomerization mechanism proposed in Figure **??** by the previous DFT[44] and CASPT2[47] static studies. However, note that none of such trajectories reach the intermediate state **MS2**. To a large extent this is due to the systematic underestimation of the triplet excitation energies by TD-DFT/BP86 with respect to the MS-CASPT2 ones[48]. The larger energy difference

between singlet and triplet states has a large impact on the final photodynamics scenario, and obviously affects the position of the two T_1/S_0 minimum energy crossing points. In particular, the position of $\mathbf{MECP}_2$ is of crucial importance, as this crossing point affords a way to go from ^{3}**GS** to **MS2** (see Figure 6.2). According to TD-DFT/BP86, this funnel is located 0.62 eV higher than the minimum ^{3}**GS** (see Table 6.2 and Figure 6.2). Therefore, to reach the intermediate **MS2**, the trajectories ought to visit the crossing point region and surmount a large activation barrier, making **MS2** less susceptible to be populated. In this scenario, the trajectories switch in favour of the ^{3}**GS**→**GS** pathway through $\mathbf{MECP}_1$ due to the more affordable energy barrier of 0.17 eV between ^{3}**GS** and $\mathbf{MECP}_1$. Those facts suggest that the **GS**→**MS2** isomerization process does not seem to be feasible with TD-DFT/BP86 and any other DFT functional because of the systematic underestimation of triplet excitation energy[48]. In contrast, the MS-CASPT2 results[47] show more favourable energy landscapes that would promote the population of the intermediate **MS2**. Furthermore, such simulations will improve rate and efficiency of the ISCs, as the energy gap between singlets and triplets is smaller at CASPT2 level. Those facts suggest that the **GS**→**MS2** isomerization process is hindered with TD-DFT/BP86, while it would be more favorable if MS-CASPT2 dynamical simulations could be performed, where the gaps between singlet and triplets states is smaller. However, due to the large system size and the high computational costs of the multiconfigurational methods, it is not possible to run such non-adiabatic simulations with CASPT2.

6.3.3 Excited-State Dynamics of Pathway II and Pathway III

We now briefly discuss the mechanism behind the trajectories related to pathway **II** and **III**, which account for the 64% of trajectories, see Figure 6.8, left. These trajectories terminated within 30 to 200 fs, as soon as the two singlet states S_1 and S_0 were close in energy (gap of ca. 0.2 eV or less around the **TS1**) and the multireference character of the ground state wavefunction becomes significant. As can be seen from Figure 6.3 (**B**), within 200 fs, the singlet population of singlet excited population reaches 35% and the triplets 65%, however by considering all the 144 these rates become 24% for the singlet and 43% for the triplet populations. The associated values of the Ru-N-O angle and Ru-NO bond length in Figure 6.7 show that all the trajectories halt in between ^{3}**GS** and **TS1**. The singlet trajectories that halt in a singlet state undergo a series of IC transitions that lead to the population of S_1 and S_0 in the region around **TS1**. Note in Figure 6.7 that none of these trajectories halted on S_2, suggesting a rapid depopulation of this state, as already seen and discussed in the first set of trajectories. However, in this case the readily depopulation is also due to the rapid energy growth of S_2 in the region between ^{3}**GS** and **TS1** (see Figure 6.2). Indeed, at ^{3}**GS** the stationary BP86 calculations predict an S_1-S_2 energy gap of 0.32 eV, whereas at **TS1** this gap becomes 0.7 eV. On the other hand, in the same region the S_0 energy increases with the Ru-N-O bending angle, whereas the S_1 energy decreases and as a result, the S_0-S_1 energy gap reduces. Particularly, near the transition state **TS1** the gap is predicted

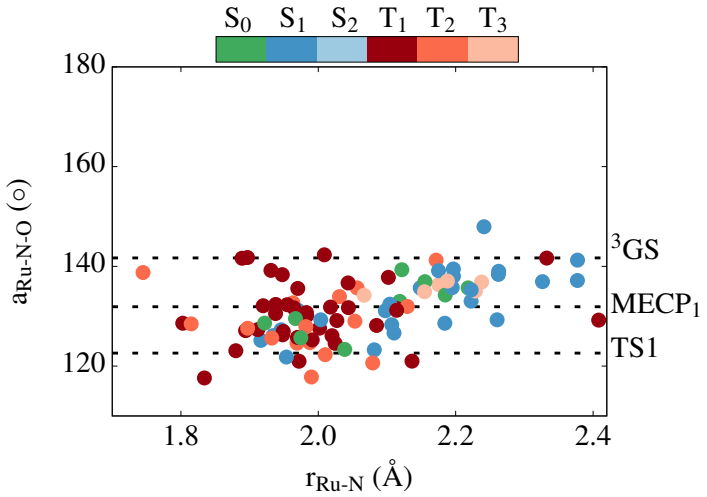

Figure 6.7 Geometrical parameters of the crashed geometries.

by stationary calculations to be around 0.24 eV but the dynamical simulations demonstrate that these two states can get much closer in this region. These findings suggest the presence of a S_1/S_0 conical intersection nearby **TS1** that promotes the efficient formation of **MS2** through the singlet manifold –as suggested by the MS-CASPT2 calculations in Chapter 3. Accordingly, it can be assumed that the singlet trajectories will continue through this conical intersection undergoing another IC which eventually populates **MS2**, in agreement with pathway **II** discussed in Section **??**. This mechanism is also shown in Figure 6.8 left by the blue dashed arrows. To support this scenario, two crashed trajectories have been restarted from a Ru-N-O angle of 105° in order to overtake the S_1/S_0 near-degeneracy region. The simulations shown that **MS2** is readily reached within 30 fs, reinforcing our assumption regarding this subset of trajectories.

The remaining trajectories that halted on a triplet state undergo in first part of the simulation a series of efficient ISC and IC transitions noticeable in Figure 6.3 (**B**), similarly to what was found in pathway **I**, although here the ISC is faster (80 fs) and therefore, more efficient. These trajectories could reach **MS2** through the **MECP**$_2$ funnel, which affords an easily accessible way as it only involves spin-flipping with no energy barriers from the uppermost triplet states. Indeed, according to the BP86 stationary calculations, this crossing point is located at the same energy of the T_1 state at the **TS1** geometry (see Figure 6.2). Thus, it can be fairly assumed that this subset of triplet trajectories would have reached **MS2** through **MECP**$_2$ if no convergence problems were encountered. This new route called pathway **III**, differs from pathway **I** does not involve the minimum ^{3}**GS** but directly concerns IC and ISC relaxations towards **MECP**$_2$. Accordingly, it should be more efficient because no energy barriers are involved. Nevertheless, it can also be assumed that these trajectories relax back to the ^{3}**GS** minimum.

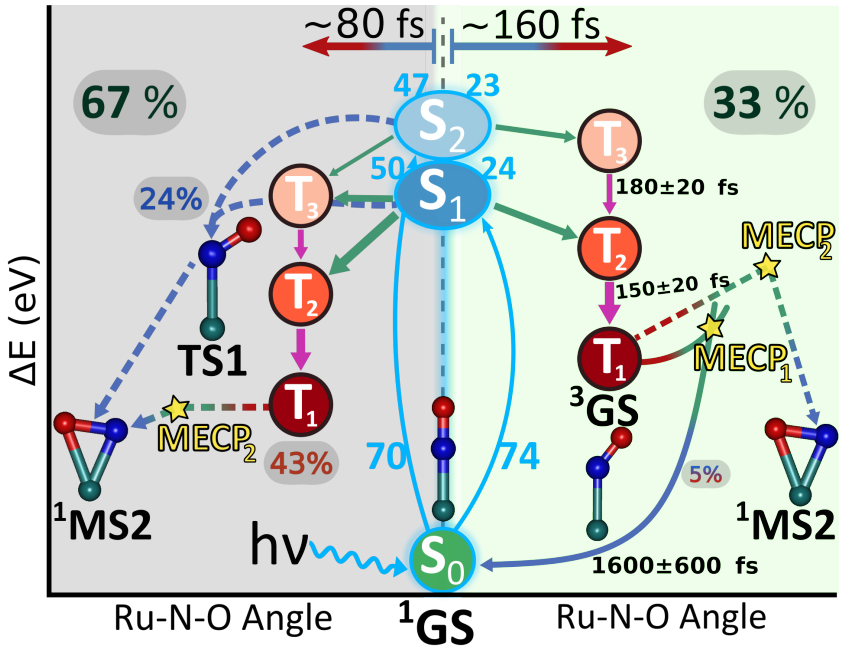

Figure 6.8 Kinetic and mechanistic model for the photoisomerization of trans-$[RuCl(NO)(Py)_4]^{2+}$, according to the SHARC dynamics. On the right (light green background) the deactivation diagram of pathway **I** (subset of trajectories that reached 1000 fs). On the left (grey background) the deactivation diagram of pathway **II** (subset of terminated trajectories). 70 and 74 (light blue digits) trajectories were prepared in the excited states S_1 and S_2, respectively. Out of the 70 (74) trajectories, 23 (24) followed pathway **I**, 21 (14) **II**, and 29 (33) **III** respectively. Solid arrows indicate the net population transfer between pairs of adiabatic states: in green for ISC between singlet and triplet states, in blue for IC between singlet states, in red for IC between triplet states. The width of the arrows is proportional to the number of net hops listed in Table 6.2 and Table **??**. Dashed arrows depict isomerization steps not directly observed in the SHARC dynamics, but assumed with the help of stationary MS-CASPT2 calculations.

6.4 Conclusions

In summary, we investigated the ultrafast dynamics of the trans-$[RuCl(NO)(Py)_4]^{2+}$complex. Non-adiabatic simulations show that NO photoisomerization can take place via three mechanisms in a ratio of 4:2:3, which involve intersystem crossing plus internal conversion for the first and the third route, or internal conversion only for the second one. The routes compete within the first 200 fs. A first subset of trajectories (33%) pertain pathway **I** undergoing IC and ISC relaxation towards the triplet T_1. The propagation shows that ISCs occur with a rate constant of 160±30 fs, confirming the ultrafast character of this non-adiabatic transition for this ruthenium nitrosyl complex. Time dependent geometry analysis identified nuclear motion corresponding to this relaxation to be towards the first minimum ^{3}**GS** in the triplet state T_1. Moreover, the long simulation time of 1 ps have given the opportunity to observe a

small amount (5%) of trajectories that come back to the starting isomer **GS**, highlighting one of the possible quenching funnel that can slow down the entire photoisomerization process. A second subset of trajectories (24%) halted in the region near **TS1** on a singlet state S_1 or S_0 within the first 200 fs. These trajectories belong to pathway **II** which does not involve ISC, but only IC relaxation towards **TS1** or the near conical intersection to eventually reach **MS2** via another IC. The third subset of trajectories (43%) halted on a triplet state in the first 200 fs in the region near **TS1**, and relate to a new assumed route called pathway **III**. Similarly to pathway **I**, these trajectories undergo ICs and ISCs, but with a faster time scale of 80 fs, which makes ISC even more efficient. Once on the triplet state these trajectories could either reach **MS2** via ISC through the near $\mathbf{MEPC}_2$ or relax back to the minimum ^{3}**GS**. In both cases these pathways do not involve energy barriers.
The results of this chapter will be contained in a paper in preparation.

Bibliography

[1] J. C. Tully. Molecular dynamics with electronic transitions. *J. Chem. Phys.*, 93(2):1061–1071, 1990.

[2] S. Mai, P. Marquetand, and L. González. A general method to describe intersystem crossing dynamics in trajectory surface hopping. *Int. J. Quantum Chem*, 115(18):1215–1231.

[3] M. Richter, P. Marquetand, J. González-Vázquez, I. Sola, and L. González. SHARC: ab initio molecular dynamics with surface hopping in the adiabatic representation including arbitrary couplings. *J. Chem. Theory Comput.*, 7(5):1253–1258, 2011.

[4] S. Mai, P. Marquetand, and L. González. Nonadiabatic dynamics: The SHARC approach. *Wiley Interdisciplinary Reviews: Computational Molecular Science*, 0(0):e1370.

[5] S. Mai, P. Marquetand, and L. González. Nonadiabatic dynamics: The sharc approach. *WIREs Comput. Mol. Sci.*, 2018.

[6] L. Favero, G. Granucci, and M. Persico. Dynamics of acetone photodissociation: a surface hopping study. *Phys. Chem. Chem. Phys.*, 15:20651–20661, 2013.

[7] S. Mai, P. Marquetand, M. Richter, J. González-Vázquez, and L. González. Singlet and triplet excited-state dynamics study of the keto and enol tautomers of cytosine. *Chem. Phys. Chem.*, 14(13):2920–2931.

[8] C. E. Crespo-Hernández, L. Martínez-Fernández, C. Rauer, C. Reichardt, S. Mai, M. Pollum, P. Marquetand, L. González, and I. Corral. Electronic and structural elements that regulate the excited-state dynamics in purine nucleobase derivatives. *J. Am. Chem. Soc.*, 137(13):4368–4381, 2015.

[9] M. Marazzi, S. Mai, D. Roca-Sanjuán, M. G. Delcey, R. Lindh, L. González, and A. Monari. Benzophenone ultrafast triplet population: Revisiting the kinetic model by surface-hopping dynamics. *J. Phys. Chem. Lett.*, 7(4):622–626, 2016.

[10] S. Mai, P. Marquetand, and L. González. Intersystem crossing pathways in the noncanonical nucleobase 2-thiouracil: A time-dependent picture. *J. Phys. Chem. Lett*, 7(11):1978–1983, 2016.

[11] S. Mai, P. Marquetand, and L. González. Non-adiabatic and intersystem crossing dynamics in SO_2. ii. the role of triplet states in the bound state dynamics studied by surface-hopping simulations. *J. Chem. Phys.*, 140(20):204302, 2014.

[12] A. J. Atkins and L. González. Trajectory surface-hopping dynamics including intersystem crossing in $[Ru(bpy)_3]^{2+}$. *Journal Phys. Chem. Lett.*, 8(16):3840–3845, 2017.

[13] L. Freitag and L. González. Theoretical spectroscopy and photodynamics of a ruthenium nitrosyl complex. *Inorg. Chem.*, 53(13):6415–6426, 2014.

[14] G. te Velde, F. M. Bickelhaupt, E. J. Baerends, C. Fonseca Guerra, S. J. A. van Gisbergen, J. G. Snijders, and T. Ziegler. Chemistry with adf. *J. Comput. Chem.*, 22(9):931–967, 2001.

[15] A. D. Becke. Density-functional exchange-energy approximation with correct asymptotic behavior. *Phys. Rev. A*, 38:3098–3100, 1988.

[16] J. P. Perdew. Density-functional approximation for the correlation energy of the inhomogeneous electron gas. *Phys. Rev. B*, 33:8822–8824, 1986.

[17] G.S.M. Tong, E.L.-M. Wong, and Che C.-M. Density functional theory study of trans-dioxo complexes of iron, ruthenium, and osmium with saturated amine ligands, trans-$[M(O)_2(NH_3)_2(NMeH_2)_2]^{2+}$ (M=Fe, Ru, Os), and Detection of $[Fe(qpy)(O)_2]^{n+}$ (n=1, 2) by high-resolution ESI mass spectrometry. *Chemistry A European Journal*, 14(18):5495–5506.

[18] J. Kuta, S. Patchkovskii, M. Z. Zgierski, and P. M. Kozlowski. Performance of DFT in modeling electronic and structural properties of cobalamins. *J. Comp. Chem.*, 27(12):1429–1437.

[19] P. Lodowski, M. Jaworska, T. Andruniów, M. Kumar, and P. M. Kozlowski. Photodissociation of CoC bond in methyl- and ethylcobalamin: An insight from TD-DFT calculations. *J. Phys. Chem. B*, 113(19):6898–6909, 2009.

[20] S. DeBeer George, T. Petrenko, and F. Neese. Prediction of iron K-Edge absorption spectra using time-dependent density functional theory. *J. Phys. Chem. A*, 112(50):12936–12943, 2008.

[21] F. Plasser, M. Ruckenbauer, S. Mai, M. Oppel, P. Marquetand, and L. González. Efficient and flexible computation of many-electron wave function overlaps. *Journal of Chemical Theory and Computation*, 12(3):1207–1219, 2016.

[22] R. Fournier. Second and third derivatives of the linear combination of gaussian type orbitalsâlocal spin density energy. *J. Chem. Phys.*, 92(9):5422–5429, 1990.

[23] B. I. Dunlap and J. Andzelm. Second derivatives of the local-density-functional total energy when the local potential is fitted. *Phys. Rev. A*, 45:81–87, Jan 1992.

[24] A. Komornicki and G. Fitzgerald. Molecular gradients and hessians implemented in density functional theory. *J. Chem. Phys.*, 98(2):1398–1421, 1993.

[25] S. M. Colwell, C. W. Murray, N. C. Handy, and R. D. Amos. The determination of hyperpolarisabilities using density functional theory. *Chem. Phys. Lett.*, 210(1):261 – 268, 1993.

[26] G. Granucci, M. Persico, and A. Zoccante. Including quantum decoherence in surface hopping. *J. Chem. Phys.*, 133(13):134111, 2010.

[27] F. Plasser, M. Wormit, and A. Dreuw. New tools for the systematic analysis and visualization of electronic excitations. i. formalism. *J. Chem. Phys.*, 141(2):024106, 2014.

[28] F. Plasser and A. Dreuw. High-level ab initio computations of the absorption spectra of organic iridium complexes. *J. Phys. Chem. A*, 119(6):1023–1036, 2015.

[29] F. Plasser. TheoDORE 1.4: Theoretical density, orbital relaxation and exciton analysis. `http://theodore-qc.sourceforge.net/`, Last accessed on 28-06-2018.

[30] S. Mai, F. Plasser, J. Dorn, M. Fumanal, C. Daniel, and L. González. Quantitative wave function analysis for excited states of transition metal complexes. *Coord. Chem. Rev.*, 361:74 – 97, 2018.

[31] F. Plasser and H. Lischka. Analysis of excitonic and charge transfer interactions from quantum chemical calculations. *J. Chem. Theory Comput.*, 8(8):2777–2789, 2012.

[32] B. J. Coe, T. J. Meyer, and P. S. White. Synthetic and structural studies on trans-tetrapyridine complexes of ruthenium(II). *Inorg. Chem.*, 34(3):593–602, 1995.

[33] L. Khadeeva, W. Kaszub, M. Lorenc, I. Malfant, and M. Buron-Le Cointe. Two-step photon absorption driving the chemical reaction in the model ruthenium nitrosyl system $[Ru(py)_4Cl(NO)](PF_6)_2 \cdot 1/2H2O$. *Inorg. Chem.*, 55(9):4117–4123, 2016.

[34] J. P. Dahl and M. Springborg. The morse oscillator in position space, momentum space, and phase space. *J. Chem. Phys.*, 88(7):4535–4547, 1988.

[35] R. Schinke. *Photodissociation Dynamics: Spectroscopy and Fragmentation of Small Polyatomic Molecules*. Cambridge Monographs on Atomic, Molecular and Chemical Physics. Cambridge University Press, 1993.

[36] Barbatti M. and Sen K. Effects of different initial condition samplings on photodynamics and spectrum of pyrrole. *Int. J. Quantum Chem*, 116(10):762–771.

[37] D. Jacquemin, E. A. Perpète, I. Ciofini, and C. Adamo. Assessment of functionals for TD-DFT calculations of singlettriplet transitions. *J. Chem. Theory Comput.*, 6(5):1532–1537, 2010.

[38] M. Barbatti, G. Granucci, M. Persico, M. Ruckenbauer, M. Vazdar, M. Eckert-Maksić, and H. Lischka. The on-the-fly surface-hopping program system Newton-X: Application to ab initio simulation of the nonadiabatic photodynamics of benchmark systems. . *Photochem. Photobiol A: Chemistry*, 190(2):228 – 240, 2007. Theoretical Aspects of Photoinduced Processes in Complex Systems.

[39] S. Nangia, A. W. Jasper, T. F. Miller, and D. G. Truhlar. Army ants algorithm for rare event sampling of delocalized nonadiabatic transitions by trajectory surface hopping and the estimation of sampling errors by the bootstrap method. *J. Chem. Phys.*, 120(8):3586–3597, 2004.

[40] C. Bressler, C. Milne, V.-T. Pham, A. ElNahhas, R. M. van der Veen, W. Gawelda, S. Johnson, P. Beaud, D. Grolimund, M. Kaiser, C. N. Borca, G. Ingold, R. Abela, and M. Chergui. Femtosecond xanes study of the light-induced spin crossover dynamics in an iron(II) complex. *Science*, 323(5913):489–492, 2009.

[41] A. Cannizzo, C. J. Milne, C. Consani, W. Gawelda, C. Bressler, F. van Mourik, and M. Chergui. Light-induced spin crossover in fe(II)-based complexes: The full photocycle unraveled by ultrafast optical and X-ray spectroscopies. *Coord. Chem. Rev.*, 254(21-22):2677–2686, 2010.

[42] O. Bräm, F. Messina, E. Baranoff, A. Cannizzo, M. K. Nazeeruddin, and M. Chergui. Ultrafast relaxation dynamics of Osmium–polypyridine complexes in solution. *J. Phys. Chem. C*, 117(31):15958–15966, 2013.

[43] M. A. El-Sayed. Spin—orbit coupling and the radiationless processes in nitrogen heterocyclics. *J. Chem. Phys.*, 38(12):2834–2838, 1963.

[44] J. Sanz García, F. Alary, M. Boggio-Pasqua, I. M. Dixon, I. Malfant, and J.-L. Heully. Establishing the two-photon linkage isomerization mechanism in the nitrosyl complex trans-$[RuCl(NO)(py)_4]^{2+}$ by DFT and TDDFT. *Inorg Chem.*, 54(17):8310–8318, 2015.

[45] M. Radoń, E. Broclawik, and K. Pierloot. Electronic structure of selected $FeNO_7$ complexes in heme and non-heme architectures: A density functional and multireference ab initio study. *J. Phys. Chem. B*, 114(3):1518–1528, 2010.

[46] T. S. Kurtikyan, V. A. Hayrapetyan, G. G. Martirosyan, R. K. Ghazaryan, A. V. Iretskii, H. Zhao, K. Pierloot, and P. C. Ford. Nitrosyl isomerism in amorphous Mn(TPP)(NO) solids. *Chem. Commun.*, 48:12088–12090, 2012.

[47] F. Talotta, J.-L. Heully, F. Alary, I. M. Dixon, L. González, and M. Boggio-Pasqua. Linkage photoisomerization mechanism in a photochromic ruthenium nitrosyl complex: New insights from an MS-CASPT2 study. *J. Chem. Theory Comput.*, 13(12):6120–6130, 2017.

[48] A. J. Atkins, F. Talotta, L. Freitag, M. Boggio-Pasqua, and L. González. Assessing excited state energy gaps with time-dependent density functional theory on ru(II) complexes. *J. Chem. Theory Comput.*, 13(9):4123–4145, 2017.

Summary

The main goal of this thesis was the investigation of the photochemistry of the trans-$[RuCl(NO)(Py)_4]^{2+}$molecule, a particular type of ruthenium nitrosyl complex that acts as a photochromic system. The study of photochemical and photophysical processes has been addressed with both static ab-initio calculations and semiclassical molecular dynamics simulations in gas phase. A detailed understanding of the photoisomerization and photodissociation mechanisms of the nitrosyl group NO is important for determining which factors make both processes either slow or inefficient.

During the period spent in Université Paul Sabatier, these photochemical mechanisms have been studied through accurate SA-CASSCF/MS-CASPT2 calculations, by characterizing ground and excited states for both singlet and triplet spin multiplicities. For the photoisomerization mechanism, the MS-CASPT2 absorption spectra of the three isomers **GS**, **MS2**, **MS1** revealed a two-photon sequential absorption mechanism, in agreement with previous experiments[1] and DFT[2] calculations. The analysis of the singlet and triplet MS-CASPT2 PESs along the S_1 pathway (**GS**$\rightarrow{}^1$**GS***), together with the singlet-triplet spin-orbit coupling calculations, helped to clarify the first step of the photoisomerization process, hinting for a non-radiative pathway relying on a very efficient singlet to triplet ISC just after light absorption. Indeed, the close proximity of the singlet and triplet PESs near the FC region and the significant SOC along the S_1 relaxation pathway, should promote a quick relaxation of the singlet excited states towards the triplets. Furthermore, the S_1 and S_2 states cross several times with the triplets T_2 and T_3, making ISC even easier near such crossing points. These results confirm previous hypothesis of earlier DFT studies. Further multiconfigurational calculations on linear interpolated scans on singlet (**GS**$\rightarrow$**TS1**$\rightarrow$**MS2**$\rightarrow$**TS1**$\rightarrow$**MS1**) and triplet (^{3}**GS**$\rightarrow{}^3$**TS1**$\rightarrow{}^3$**MS2**$\rightarrow{}^3$**TS2**$\rightarrow{}^3$**MS1**) PESs shed light on the role of the excited states for the subsequent reaction steps. The shape of the MS-CASPT2 PESs reinforced the multistep sequential two-photon mechanism through the intermediate species **MS2** involving several ISC and IC transitions. However, despite the good agreement between CASPT2 and DFT regarding the singlet states, a relevant difference exists when comparing the triplet states coming from the two methods. Indeed, according to the MS-CASPT2 calculations all the triplet states are shifted up in energy by about 0.6 eV respect to the triplets in DFT. This large change in relative energies has important consequences on the position of the singlet/triplet crossing point. Accordingly, the whole photoisomerization process is predicted to be easier at the CASPT2 level than at

the DFT level because of this shift of the triplets, in line with the experimental outcomes which show a nearly complete photoconversion yield for this complex. Moreover, the MS-CASPT2 topology of the S_1 and S_2 PESs hints for a new unprecedented non-radiative pathway only involving singlet states. In this case, the molecule should relax through a series of efficient IC from the higher singlet excited states towards the ground state S_0. Indeed, the analysis of the CASSCF wavefunction reveals that S_1 and S_0 are strongly coupled near **TS1** and **TS2**, suggesting the presence of a S_1/S_0 conical intersection which could make this "IC only" pathway more likely to occur.
For the photodissociation pathway, the same multiconfigurational CASSCF/CASPT2 methods were employed. The results showed that the ^{3}**MS2** isomer is the best candidate for $NO^\bullet$ photorelease because of the low Ru-NO dissociation energy required from this species in agreement with previous DFT results, despite the fact that DFT and CASPT2 energetics are different. According to this mechanism, the complex should first undergo a partial photoisomerization in order to attain ^{3}**MS2**. From there the complex can either continue the photoisomerization or undergo photodissociation.
The work in this thesis also contained the optimization of the ADF quantum chemistry program package, carried out during the secondment at SCM in Amsterdam. The aim of such modifications was to speed-up the TD-DFT electronic structure calculations performed on-the-fly during dynamical calculations. Thanks to the implementation of the multiple gradients and the independent number of singlet and triplet excited states made the ADF code much faster, making possible to extend the total dynamics simulations time. Before running dynamics simulations with SHARC, a detailed assessment of many DFT functionals against the CASPT2 results has been carried out. Mean signed error and mean absolute error of the DFT vertical excitations and energy gaps relative to the S_1 state against the MS-CASPT2 ones have been computed with and without TDA. The analysis of the errors for the vertical excitations reveals that for all the GGA and LDA functionals, the MSE and MAE provide similar values regardless of TDA, underestimating to a similar extent both singlet and triplet energies within 0.2 eV. The hybrid XC functionals and their meta and range-separated counterparts show more variation in their MSE and MAE values. Nevertheless, the majority of the XC functionals investigated show smaller errors for the singlet and triplet vertical transition energies than the GGA functionals. The use of TDA affects particularly the triplet states calculated using the hybrid functionals. The analysis of MSE and MAE for the energy gaps of the singlet and triplet excited states relative to S_1 revealed that the GGA XC functionals provide better relative energies than the hybrid XC functionals when TDA is used. From these results it comes out that the use of standard GGA functionals such as PBE or BP86 is more suitable to describe the excitation energies and the energy gaps than the hybrid XC functionals. The comparison of the relative energies was only one benchmark criteria. Indeed, the assessment of the excited state character is also very important. To this end the analysis of the state character through wavefunction overlap revealed that the S_1, S_2, T_1, T_2, T_3 states of MS-CASPT2 are reproduced in the correct order by the GGA functional BP86 when using TDA. Furthermore, BP86 shows adequate performances in terms of energies and therefore

this functional was selected for the semiclassical dynamics simulations.
During the time spent in Vienna University, the first part of the photoisomerization mechanism (**GS**→**MS2**) has been studied using the SHARC dynamics simulations. In this way, it was possible to directly observe ISC and IC and thus to verify the results coming from the static MS-CASPT2 calculations. The simulations identified three different photoisomerization pathways from which two are in agreement with the ones assumed in the MS-CASPT2 calculations, whereas a third one represents a novel relaxation pathway. As expected, due to the significant spin-orbit coupling most of trajectories (43%+33%) undergo ultrafast ISC in a time scale between 80 and 100 fs whereas the remain part (24%) populates a singlet state, either S_1 or S_0. The analysis of the classical population ensemble and the geometrical changes induced by the various relaxation processes revealed that the 33% of trajectories undergoing ultrafast ISC+IC, eventually relax on the T_1 state of the ^{3}**GS** isomer, de-facto the first reachable minimum along the photoisomerization pathway. This result is in agreement with one of the envisaged MS-CASPT2 pathways, and furthermore it highlights the ultrafast nature of the ISC process. From here a small amount of trajectories (5%) slowly undergo a $T_1 \rightarrow S_0$ ISC back to starting isomer **GS** through the near $MECP_1$. This former pathway also assumed by MS-CASPT2 and the previous DFT calculations represents a quenching funnel that can potentially delay the entire photoisomerization mechanism. However, these trajectories do not reach the **MS2** intermediate because of the systematic underestimation of the triplet states by BP86/TDA with respec to the MS-CASPT2 energies. Those facts suggest that the **GS**→**MS2** isomerization process is hindered with TD-DFT/BP86, while it would be more favorable if MS-CASPT2 dynamical simulations could be performed, where the gaps between singlet and triplets states are smaller. A second set of trajectories corresponding to 24% halted within the first 200 fs because they reach the near degeneracy region nearby the **TS1** species. These trajectories undergo multiple ICs and are compatible with the second pathway assumed by the CASPT2 calculations which involves singlet states only. The eventual set of trajectories (43%) undergo efficient ISC+ICs, halting within the first 200 fs in the zone near **TS1**. These trajectories can potentially reach **MS2** undergoing ISC which should be eased by the near $MECP_2$ or they can relax back to the ^{3}**GS** minimum.
Both IC and ISC+IC pathways show that gas phase simulations are capable of qualitatively modeling some of the trans-$[RuCl(NO)(Py)_4]^{2+}$photoisomerization pathways. However, for a better understanding of the underlying processes, a proper treatment of the environment and the surrounding solvent are needed, specially when investigating the photodissociation process. Using a QM/MM scheme, both the static as well as the dynamics simulations presented in this thesis can be improved. By comparing the results obtained using QM/MM to the gas phase ones, the effect of the solvent in both photoisomerization and photorelease processes can be properly evaluated.

Bibliography

[1] L. Khadeeva, W. Kaszub, M. Lorenc, I. Malfant, and M. Buron-Le Cointe. Two-step photon absorption driving the chemical reaction in the model ruthenium nitrosyl system $[Ru(py)_4Cl(NO)](PF_6)_2 \cdot 1/2H_2O$. *Inorg. Chem.*, 55(9):4117–4123, 2016.

[2] J. Sanz García, F. Alary, M. Boggio-Pasqua, I. M. Dixon, I. Malfant, and J.-L. Heully. Establishing the two-photon linkage isomerization mechanism in the nitrosyl complex trans-$[RuCl(NO)(py)_4]^{2+}$ by DFT and TDDFT. *Inorg Chem.*, 54(17):8310–8318, 2015.

Appendix A

Supporting Information for Chapter 3

Listing A.1 ^{1}**GS*** optimized TD-B3LYP Cartesian coordinates (in Å). The following basis sets have been used: cc-pVDZ for H atoms, cc-pVTZ for C, N, O and Cl atoms and a Stuttgart relativistic small-core effective potential for ruthenium with its associated polarized basis set including two f and one g polarization functions. This calculation was performed with Gaussian09 (Rev. D01).,

Ru	−0.003661660221	−0.023321766967	0.030234952276
Cl	0.097637418817	−0.089427656597	−2.362477324127
N	−0.011547087936	2.106654833418	0.002174075358
N	2.120489603610	0.014497587109	0.055579103502
N	−0.009266288966	−2.152641334388	−0.008898739024
N	−2.128985876660	0.017198348944	−0.025618665801
N	−0.020142105207	−0.049769597530	1.928296255994
O	0.587925351475	−0.467138013900	2.817715003406
C	−0.573219234833	2.798548238163	1.020618331201
H	−1.005447393744	2.217764763078	1.823418255196
C	−0.613864962820	4.176523379414	1.047250459551
H	−1.082792262058	4.678892094134	1.882737476164
C	−0.047819899548	4.890224347104	−0.004204443647
H	−0.062710223458	5.973025437463	−0.007508735445
C	0.535947715765	4.185024584624	−1.048403400232
H	0.990100467470	4.693980507811	−1.888099580058
C	0.533753115205	2.803419482237	−1.019884603287
H	0.960968236093	2.223314103332	−1.823596564537
C	2.799381733304	0.743714665220	0.970365746911
H	2.217070471475	1.313610649147	1.679096329283
C	4.177103310337	0.794126243239	1.006612963356
H	4.666582190659	1.401853404150	1.755787507817
C	4.906327024051	0.061564879079	0.076243529151
H	5.988964890980	0.080786022991	0.084239039222
C	4.216015642814	−0.690004483798	−0.864502570387
H	4.735891945147	−1.274278410241	−1.611957647639
C	2.834544471858	−0.686983025650	−0.855221016257
H	2.269853383915	−1.240525541468	−1.588717451842
C	−0.752824202399	−2.814613275206	−0.924513235619
H	−1.310012690702	−2.211321726724	−1.623482040287
C	−0.792282332806	−4.193760835442	−0.983334716433
H	−1.408215872676	−4.672060051675	−1.733066223905
C	−0.034955928104	−4.936248142408	−0.086931328621
H	−0.044643241039	−6.018608393560	−0.117471052378
C	0.739440992460	−4.259823363142	0.848560713047
H	1.352890645153	−4.790851488196	1.564047574596

C	0.724822112323	−2.880170107830	0.862641320019
H	1.324530535543	−2.337655711781	1.578227012805
C	−2.790247429982	0.555234237771	−1.075703183798
H	−2.181986629902	0.930166050875	−1.884496707328
C	−4.169375712897	0.611044537174	−1.127069901031
H	−4.647741687948	1.056679028011	−1.988991892899
C	−4.912814117965	0.089435774292	−0.075632578852
H	−5.995205556678	0.117082801691	−0.095710176853
C	−4.237700050719	−0.469187572201	1.004655298965
H	−4.770298948791	−0.890897682775	1.846525360889
C	−2.859047975424	−0.480962956249	0.999789851063
H	−2.313421884970	−0.904104862740	1.830609000515

Listing A.2 MS4-CASPT2 singlet and triplet absolute energies for the linear interpolation **GS**→^{1}**GS***

LITP	S_0	S_1	S_2	S_3
GS	−6109.28149111	−6109.17020873	−6109.17018488	−6109.14670835
0.1	−6109.28104599	−6109.17421617	−6109.17379261	−6109.14863598
0.2	−6109.27961893	−6109.17831267	−6109.17642607	−6109.15348125
0.3	−6109.27721892	−6109.18229216	−6109.17809245	−6109.15522667
0.4	−6109.27407298	−6109.18612893	−6109.17893374	−6109.15461475
0.5	−6109.27018279	−6109.18966427	−6109.17895382	−6109.15599949
0.6	−6109.26557628	−6109.19280795	−6109.17821045	−6109.15824221
0.7	−6109.26031453	−6109.19548146	−6109.17677308	−6109.16052695
0.8	−6109.25453851	−6109.19770028	−6109.17479731	−6109.16256188
0.9	−6109.24800556	−6109.19914762	−6109.17211640	−6109.16394288
^{1}**GS***	−6109.24059076	−6109.19967612	−6109.16998629	−6109.16589457

LITP	T_1	T_2	T_3	T_4
GS	−6109.17402707	−6109.17399932	−6109.16808637	−6109.16730675
0.1	−6109.18510893	−6109.17916100	−6109.17099322	−6109.16347936
0.2	−6109.18269207	−6109.18011911	−6109.17365909	−6109.16595064
0.3	−6109.18708753	−6109.18139397	−6109.17592340	−6109.16390714
0.4	−6109.19171188	−6109.18195363	−6109.17803428	−6109.16155688
0.5	−6109.19621258	−6109.18186749	−6109.18024031	−6109.16723932
0.6	−6109.20041518	−6109.18423387	−6109.18286596	−6109.16959659
0.7	−6109.20409726	−6109.18603514	−6109.17892769	−6109.17274910
0.8	−6109.20712051	−6109.18873686	−6109.17899908	−6109.17675064
0.9	−6109.20909115	−6109.19088403	−6109.17769071	−6109.17352806
^{1}**GS***	−6109.20991726	−6109.19226761	−6109.17821596	−6109.16971753

Listing A.3 MS4-CASPT2 singlet absolute energies for the linear interpolation **GS→MS1**

LITP	S_0	S_1	S_2	S_3
GS	−6109.28149362	−6109.17020831	−6109.17018434	−6109.14670968
1	−6109.27478121	−6109.18196557	−6109.17505422	−6109.15538025
2	−6109.25674087	−6109.18999581	−6109.16974402	−6109.16313471
3	−6109.23115889	−6109.19123865	−6109.16860975	−6109.16691065
4	−6109.20931842	−6109.19347995	−6109.17789305	−6109.16940873
TS1	−6109.19288250	−6109.18142377	−6109.16948817	−6109.15982365
6	−6109.19715721	−6109.17539111	−6109.16137262	−6109.15441030
7	−6109.20528618	−6109.16995423	−6109.15347752	−6109.14423372
8	−6109.21440553	−6109.16327079	−6109.14549008	−6109.13561156
9	−6109.22154648	−6109.15345971	−6109.14155683	−6109.13317073
MS2	−6109.22509301	−6109.14960753	−6109.13822564	−6109.12824238
11	−6109.21448794	−6109.16511242	−6109.15030634	−6109.13787013
12	−6109.20025336	−6109.16301486	−6109.14646840	−6109.13621476
13	−6109.19067407	−6109.15846941	−6109.15504183	−6109.14866003
14	−6109.18529689	−6109.16867795	−6109.16062826	−6109.15471858
TS2	−6109.17729396	−6109.17100068	−6109.16696409	−6109.16374376
16	−6109.17822969	−6109.17306820	−6109.16661434	−6109.16318353
17	−6109.19291509	−6109.16652675	−6109.15858234	−6109.15651831
18	−6109.20455241	−6109.15576000	−6109.14598652	−6109.14457969
19	−6109.21439280	−6109.15030352	−6109.14709364	−6109.13849111
MS1	−6109.21796004	−6109.14818042	−6109.14817886	−6109.13958832

Listing A.4 MS4-CASPT2 triplet absolute energies for the linear interpolation ^{3}**GS→**^{3}**MS1**

LITP	T_1	T_2	T_3	T_4
^{3}**GS**	−6109.20950477	−6109.20400048	−6109.18951096	−6109.16124162
1	−6109.20567174	−6109.19694452	−6109.18473913	−6109.15393904
2	−6109.19600544	−6109.18274088	−6109.17904778	−6109.15756109
3	−6109.18663027	−6109.17990672	−6109.17449729	−6109.15409447
4	−6109.17894163	−6109.17289445	−6109.16757596	−6109.15692323
^{3}**TS1**	−6109.17187641	−6109.16404232	−6109.15796645	−6109.15511333
6	−6109.16832811	−6109.16555477	−6109.15268146	−6109.14881464
7	−6109.16893256	−6109.16342439	−6109.14737337	−6109.14247303
8	−6109.17139279	−6109.15793985	−6109.15484114	−6109.14133159
9	−6109.17435930	−6109.15735708	−6109.15125383	−6109.13434186
^{3}**MS2**	−6109.17691761	−6109.15979388	−6109.14361123	−6109.12667296
11	−6109.17301607	−6109.15701681	−6109.14914157	−6109.13686223
12	−6109.16715327	−6109.15620700	−6109.14934869	−6109.14712513
13	−6109.16791531	−6109.16199397	−6109.15515499	−6109.15233555
14	−6109.16787272	−6109.16663213	−6109.16187515	−6109.15706046
^{3}**TS2**	−6109.17062306	−6109.16848127	−6109.16528136	−6109.15891498
16	−6109.17369233	−6109.17004037	−6109.16764168	−6109.16272596
17	−6109.17641538	−6109.17505724	−6109.16664615	−6109.16648632
18	−6109.17949550	−6109.17814557	−6109.16959589	−6109.16604273
19	−6109.18257818	−6109.17879071	−6109.17168611	−6109.16716039
^{3}**MS1**	−6109.18333745	−6109.17802199	−6109.17215623	−6109.16910662

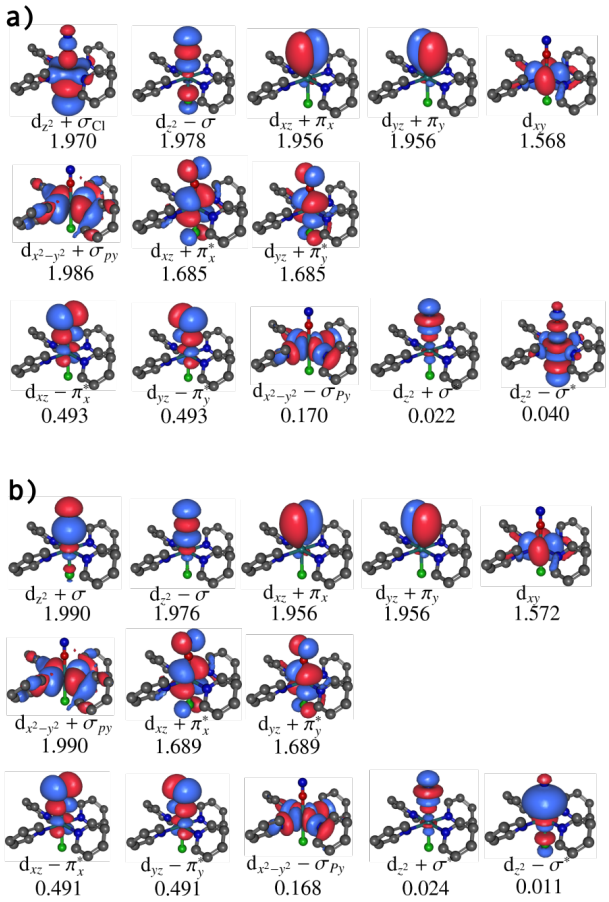

Figure A1 The two different stable solutions of the SA7-CASSCF(16,13) active space at the **MS1** geometry. a) Same solution as the one shown in Figure 3.2 for **GS**. b) Alternative solution with more involvement of the Cl atom. Reprinted with permission from *J. Chem. Theory Comput*. 2017, 13, 12, 6120-6130. Copyright 2017, American Chemical Society.

		MS4-CASPT2 States			
		T_1	T_2	T_3	T_4
CASPT2 States	T_1	0.45	0.15	-	0.45(0.99)
	T_2	0.55(0.99)	0.19	-	0.35
	T_3	-	0.66(0.99)	-	0.20
	T_4	-	-	0.99(0.99)	-

Table A1 Mixing coefficients between the four triplet CASPT2 states introduced by MS-CASPT2 at 0.1 along the LITP. Values in parentheses are the mixing coefficients at the GS geometry for comparison.

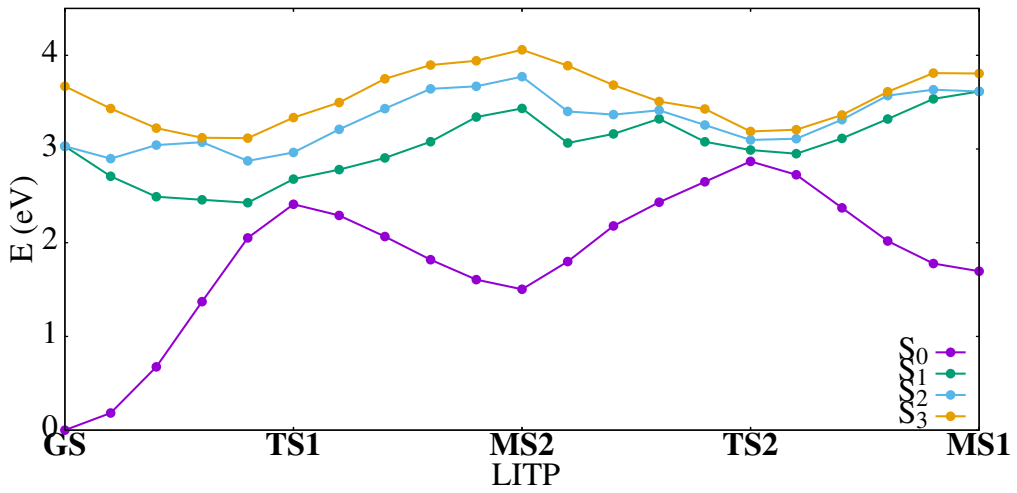

Figure A2 MS4-CASPT2 singlet potential energy profiles along the S_0 (thermal) linkage isomerization pathway (linearly interpolated transit path: LITP) between **GS**, **TS1**, **MS2**, **TS2** and the **MS1** DFT-optimized structures, using the alternative active space shown in Figure A1 (to compare with Figure 5 in Chapter 3). Reprinted with permission from *J. Chem. Theory Comput*. 2017, 13, 12, 6120-6130. Copyright 2017, American Chemical Society.

Table A2 S_0 and T_1 configurations at the triplet/singlet funnels along with the respective weights (C^2) in the perturbation modified CASSCF wavefunctions and associated spin-orbit couplings (SOC).

	crossing point 1	C_0^2	crossing point 2	C_0^2
S_0	$d_{xz} + \pi_x^* \rightarrow d_{xz} - \pi_x^*$	0.77	$d_{xz} + \pi_x^* \rightarrow d_{xz} - \pi_x^*$	0.86
T_1	$d_{yz} + \pi_y^* \rightarrow d_{yz} - \pi_y^*$	0.83	$d_{yz} + \pi_y^* \rightarrow d_{yz} - \pi_y^*$	0.87
SOC(cm^{-1}	28.41		19.55	

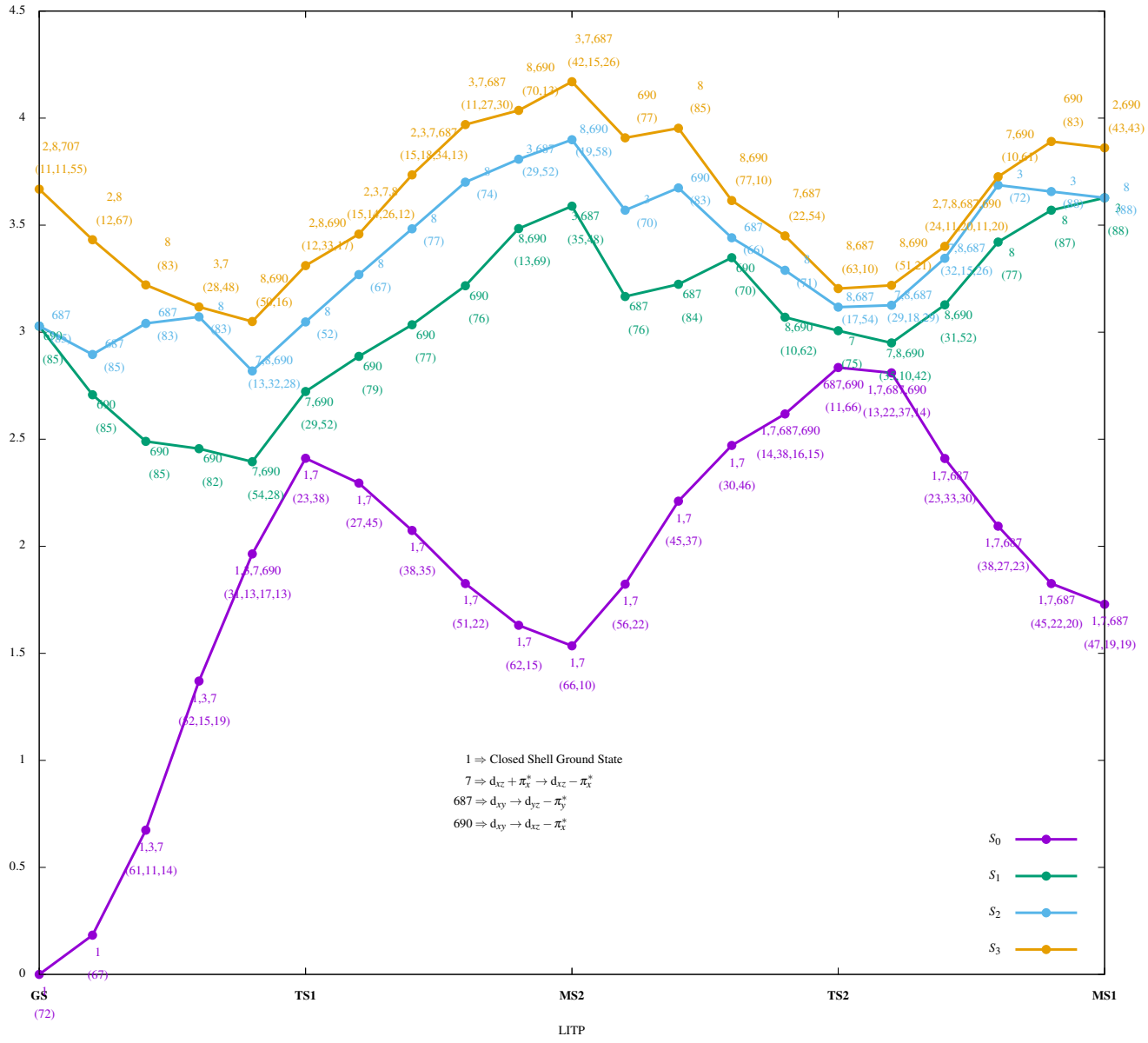

Figure A3 MS-CASPT2 energy profiles along with the main electronic characters of perturbation modified CASSCF wavefunctions for the four lowest singlet states (values in parentheses give the weight in percentage of the configuration given just above and defined at the bottom) along the thermal isomerization pathway. Reprinted with permission from *J. Chem. Theory Comput.* 2017, 13, 12, 6120-6130. Copyright 2017, American Chemical Society.

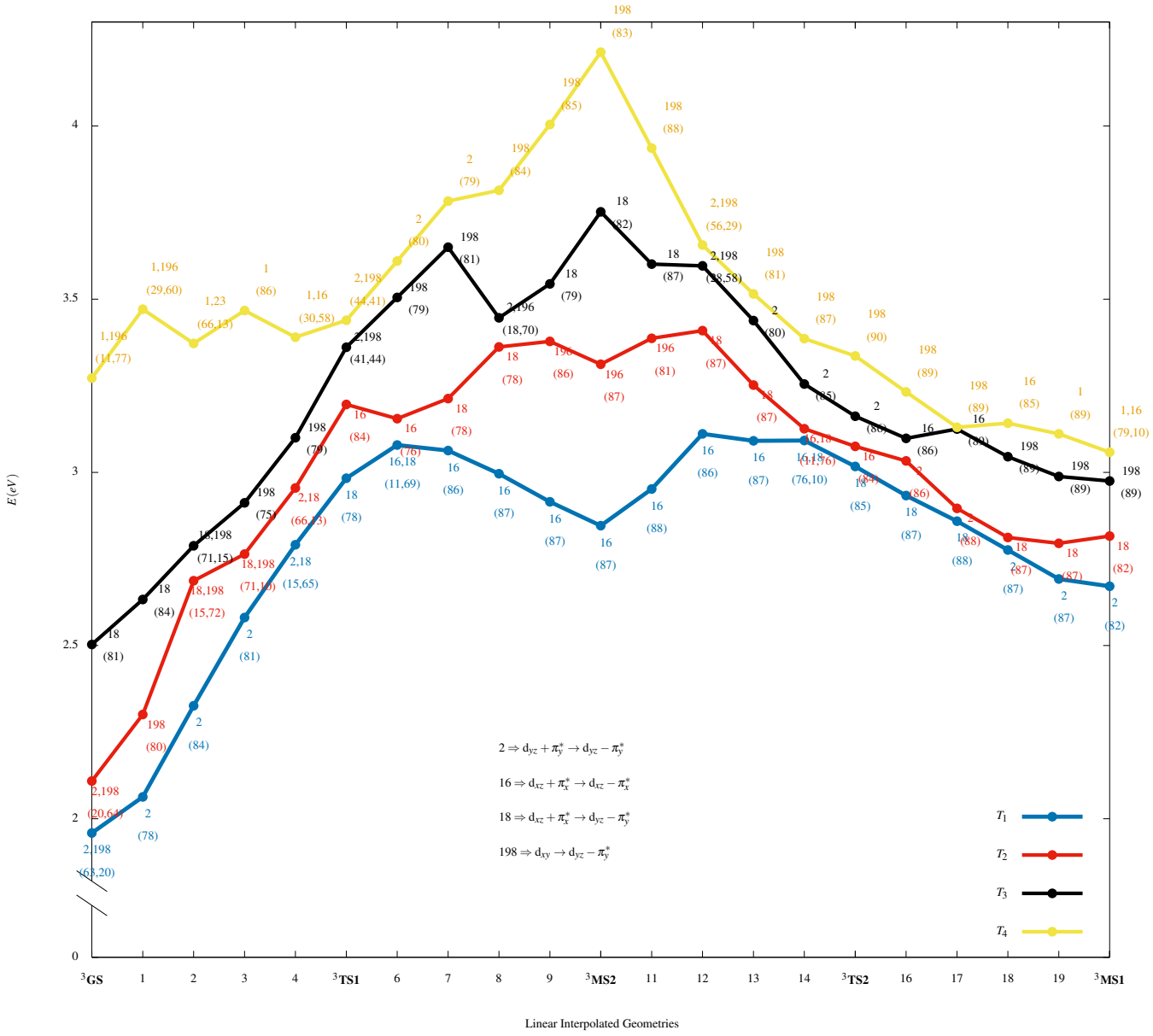

Figure A4 MS-CASPT2 energy profiles along with the main electronic characters of the perturbation modified CASSCF wavefunctions for the four lowest triplet states (values in parentheses give the weight in percentage of the configuration given just above and defined at the bottom) along the photoisomerization pathway. Reprinted with permission from *J. Chem. Theory Comput*. 2017, 13, 12, 6120-6130. Copyright 2017, American Chemical Society.

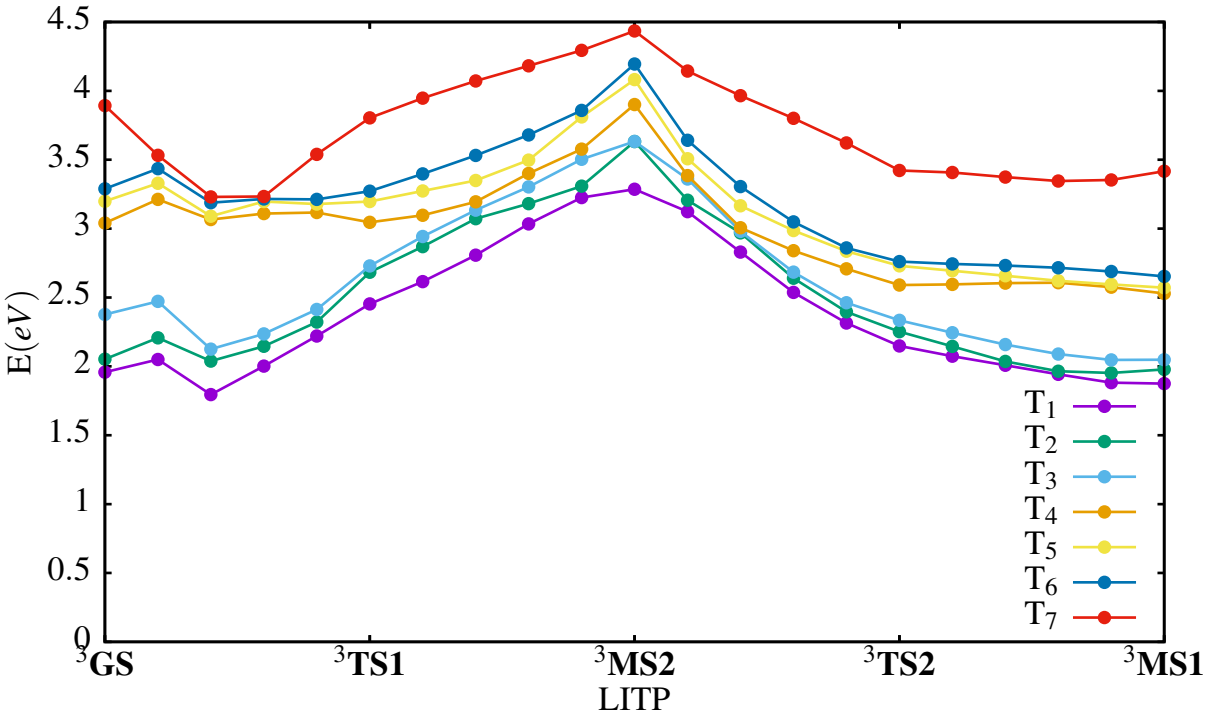

Figure A5 SA7-CASSCF(16,13) energy profiles of the seven lowest triplet states along the photoisomerization pathway. Reprinted with permission from *J. Chem. Theory Comput*. 2017, 13, 12, 6120-6130. Copyright 2017, American Chemical Society.

Table A3 Spin-orbit couplings (SOC) between S_1 and T_1 along the ^{3}**MS2**$\rightarrow{}^3$**MS1** pathway.

Geometry	SOC(cm^{-1})
^{3}**MS2**	155
2	139
3	101
4	69
^{3}**TS2**	433
7	455
8	397
9	191
10	20
^{3}**MS1**	54

List of Publications

Parts of the results included in this thesis have been published in the articles

1. **2017**: F. Talotta, J.-H. Heully, F. Alary, I. M. Dixon, L. González, M. Boggio-Pasqua
   Linkage Photoisomerization Mechanism in a Photochromic Ruthenium Nitrosyl Complex: New Insights from an MS-CASPT2 Study.
   J. Chem. Theory Comput. 13 (12), 6120-6130

2. **2017**: A. Atkins, F. Talotta, L. Freitag, M. Boggio-Pasqua, L. González
   Assessing Excited State Energy Gaps with Time-Dependent Density Functional Theory on Ru(II) Complexes.
   J. Chem. Theory Comput. 13 (9), 4123-4145

3. **2017**: J. S. García, F. Talotta, F. Alary, I. M. Dixon, J.-L. Heully, M. Boggio-Pasqua
   A Theoretical Study of the N to O Linkage Photoisomerization Efficiency in a Series of Ruthenium Mononitrosyl Complexes.
   Molecules 22 (10), 1667

For further results, two manuscripts are in preparation

- F. Talotta, L. González, M. Boggio-Pasqua,
  The NO Photodissotiation Mechanism in a Photochromic Ruthenium Nitrosyl Complex
  Manuscript in preparation (2018)

- F. Talotta, M. Boggio-Pasqua, L. González,
  Photoisomerization Dynamics of a Photochromic Ruthenium Nitrosyl Complex
  Manuscript in preparation (2018)